Distribution Agreement

In presenting this thesis or dissertation as a partial fulfillment of the requirements for an advanced degree from Emory University, I hereby grant to Emory University and its agents the non-exclusive license to archive, make accessible, and display my thesis or dissertation in whole or in part in all forms of media, now or hereafter known, including display on the world wide web. I understand that I may select some access restrictions as part of the online submission of this thesis or dissertation. I retain all ownership rights to the copyright of the thesis or dissertation. I also retain the right to use in future works (such as articles or books) all or part of this thesis or dissertation.

Signature:

_____

Brandon L. Greene Date

Proton, Electron and Proton-coupled Electron Transfer Dynamics in the Catalytic Mechanism of [NiFe] and [FeFe] Hydrogenases

By
Brandon L. Greene
Doctor of Philosophy
Chemistry

Dr. R. Brian Dyer, Advisor

Dr. Cora MacBeth, Committee Member

Dr. Tianquan Lian, Committee Member

Accepted

Dr. Lisa A. Tedesco
Dean of the James T. Laney School of Graduate Studies

Date

Proton, Electron and Proton-coupled Electron Transfer Dynamics in the Catalytic Mechanism of [NiFe] and [FeFe] Hydrogenases

By
Brandon L. Greene
B.S., Washington State University, 2005

Advisor: Dr. R. Brian Dyer

An abstract of
A dissertation submitted to the Faculty of the
James T. Laney School of Graduate Studies of Emory University
in partial fulfillment of the requirements for the degree of
Doctor of Philosophy
in Chemistry
2015

Proton, Electron and Proton-coupled Electron Transfer Dynamics in the Catalytic Mechanism of [NiFe] and [FeFe] Hydrogenases

By Brandon L. Greene

Hydrogenases are enzymes which catalyze the reversible reduction of protons to molecular hydrogen with high kinetic rates and low over-potentials using earth abundant metals, iron and nickel. Their chemical mechanism is of significant interest as a model for biomimetic systems aimed at improving existing proton reduction catalysts, but their chemical mechanism has been elusive. In this thesis, kinetic methods, both based on traditional steady state techniques as well as novel pre-steady state methods, are explored and utilized to directly observe chemical changes during catalysis by a [NiFe] hydrogenase from the hyperthermophilic *Pyrococcus furiosus* as well as an [FeFe] hydrogenase from the hyperthermophilic *Thermotoga maritima*.

Steady state kinetic analysis of the Pyrococcus furiosus [NiFe] hydrogenase was used to probe the rate determing steps and thermodynamics of redox mediator interactions revealing a product release rate determining step and relatively slow intramolecular proton transfer. Despite significant insight gained through steady state kinetic analysis, little information could be determined beyond the rate determining steps. To address this, methods for rapidly initiating the proton reduction activity of model hydrogenases were explored using photo-initiated electron transfer from small molecule photo-ionization, redox dye and quantum dot photo-sensitization. Once methods for photo-initiation were established, pre-steady state catalytic initiation of the *Pyrococcus furiosus* hydrogenase was investigated by time resolved spectroscopy, sensitive to the enzyme active site, revealing rich chemical dynamics on timescales 10^4 s^{-1} faster than the rate determining step(s). The active site dynamics probed by time resolved infrared transient absorbance demonstrated the kinetic validity of several reaction intermediates previously proposed based on equilibrium structural and spectroscopic data. Furthermore, the mechanism of the chemical reactions necessary for inter-conversion of the verified intermediates was elucidated, implicating various proton-coupled reduction pathways involved in enzymatic turnover. Additionally, pre-steady state investigation of the proton reduction activity of the *Thermotoga maritima* [FeFe] hydrogenase also revealed multiple chemical steps occurring faster than the overall catalytic rate and verified previously proposed catalytic intermediates as being kinetically competent.

Proton, Electron and Proton-coupled Electron Transfer Dynamics in the Catalytic Mechanism of [NiFe] and [FeFe] Hydrogenases

By
Brandon L. Greene
B.S., Washington State Unversity, 2005

Advisor: R. Brian Dyer, Dr.

A dissertation submitted to the Faculty of the
James T. Laney School of Graduate Studies of Emory University
in partial fulfillment of the requirements for the degree of
Doctor of Philosophy
in Chemistry
2015

Acknowledgements

First and foremost, I would like to thank my advisor, Prof. R. Brian Dyer, who has provided invaluable guidance and counsel throughout my graduate tenure. He has been a source of inspiration for me as a man of conviction, discipline and genius which are plainly evident in his scientific endeavors. Being a part of those scientific endeavors is an experience that has changed my view of what science can be, not only a method for ascertaining truth, but also a method for becoming a better person. Furthermore, in this regard I would like to also thank my committee members Prof. Tianquan Lian and Prof. Cora MacBeth who have aided in critically engaging me both scientifically and personally. Both are fantastic scientists and I have been fortunate to have been mentored and taught by them. Beyond my core committee I have also enjoyed insightful discussions with other faculty including Prof. Chris Scarborough, Prof. Emily Weinert, Prof. James Kindt, Prof. Michael Heaven, Prof. Kalid Salaita and Prof. Stephan Lutz.

I would also like to thank my parents, Linda and Jeff Greene, for their love and support throughout my life. They have given me every opportunity necessary for my own personal development as well as a critical and honest perspective. None more can be asked of a parent. They are also some of the hardest working and deepest loving people I have ever met, and given the opportunity, would have been phenomenal scientists in their own right.

Additionally, I would like to thank my girlfriend Desiree Huff, who has somehow always been able to remind me that there is a beautiful thing called "the world" outside the lab that is worth enjoying. I also thank my friends and colleagues at Emory University, particularly James Vickers, Kevin Yehl, Gokul Raghunath, Bryant Chica, Erin Schuler, Dr. Brendan Parr and Dr. Donny Magana who have been there through the highs and lows of my graduate career. Some of these friends and colleagues have been inspirational for their hard work, some for their scientific genius, some for their charisma, humor or insight and others just for the quality of friends that they are.

I would finally like to thank the people in the chemistry department who make chemistry at Emory feel like a family. Ann Dasher and Steve Krebs in particular come to mind as people who make the department feel like home. For someone who moved 2000+ miles to attend a school he knew very little about this was essential in establishing early on a productive graduate career.

Finally, I would like to thank my numerous collaborators without whom little of this thesis would have been possible. Special thanks must go out to Professor Michael Adams of the University of Georgia and his students Chang-Ho "Perry" Wu and Dr. Gerti Schut as well as Professor Michael Maroney of the University of Massachusetts Amherst and his post-doc Dr. Crisjoe Joseph.

I am very fortunate to be surrounded by such wonderful people in my life, and I credit all those listed above with this thesis.

Table of Contents

List of Figures

Chapter 4

Chapter 5

List of Tables

Chapter 1

Introduction

1.1 Renewable Energy Challenges, Chemical Fuels and the Role of Bioinorganic/Biomimetic Chemistry

Population growth, a globally rising standard of living, increasing difficulty in fossil fuel access and environmental repercussions associated with their use necessitate the development of alternative energy sources that are sustainable in nature.[1,2] Solar energy has been proposed as a sustainable energy source to supplement the planets growing energy demands, but significant challenges have restricted its use to very limited implementation.[2,3] One of the central challenges in the use and application of solar energy is the temporally uneven distribution of incident energy of the sun at any location on earth due to the solar cycle and weather. This presents an obstacle for solar energy usage, requiring the intermittent energy to be stored in order to meet energy demands at low light conditions.[4]

The present paradigm for storage of solar energy involves the conversion of light energy to chemical energy in the form of chemical bonds. This can be done by the use of batteries such as lithium ion batteries, or in combustion based chemical fuels such as H_2, hydrocarbons or O_2. Battery technology has developed significantly, but its applications have been limited based on the low energy density, low efficiency and limited lifetime. Chemical fuels such as hydrocarbons, H_2 or O_2 have higher energy density than the leading conventional battery technologies among other advantages, but their production requires catalysts. Despite progress to in their development, effective catalysts for the production of H_2, O_2 or hydrocarbons from renewable feed stocks remains a central challenge in the chemical sciences.

Of the aforementioned potential renewable chemical fuels, O_2 and H_2 are of high interest since they represent potential products of the splitting of water (H_2O), one of the most abundant chemical substances on the Earth's surface.[1,2,5] The water splitting process requires both water (OH^-) oxidation to form O_2 and proton reduction. A considerable amount of research has been dedicated to the development of heterogeneous and homogeneous catalysts for water oxidation and proton reduction.[6] Significant progress has been made in proton reduction catalysis, and indeed from an engineering perspective, inefficiencies in many potential solar water splitting modalities result from other aspects of the module such as water oxidation, catalyst-semiconductor interfaces and electron transport.[1,2,7] While this may lead to the conclusion that basic research on proton reduction is not necessary, this a short sighted inference since it is likely that future developments could result in advancement in other aspects of solar water splitting which may result in proton reduction becoming a bottleneck in system efficiency. Additionally, research on proton reduction has resulted in numerous unintended developments in the chemical sciences which will likely continue to be developed through further research.

In proton reduction, the best catalyst to date with respect to the intrinsic kinetics and thermodynamics is still platinum metal, both in heterogeneous and homogenous forms. Unfortunately, platinum is extremely scarce on the earth surface, and therefore is economically not viable for large scale use. This requires development of proton reduction catalysts based on more abundant materials such as first row transition metals, particularly nickel, iron and cobalt.[6] These metals have emerged as potential candidates for efficient proton reduction due to their relative M-H bond strength and electron affinity as demonstrated by the (over-simplified) "Volcano" plots (Fig. 1B) although their

chemistry rarely occurs through the homolytic mechanisms used to derive such plots.[8-10] This oversimplified thermodynamic treatment is useful in determining transition metals that may function to some capacity in proton reduction, but as is clear from such plots, all earth abundant metals will require additional energy (over-potentials) to drive the M-H bond formation or cleavage. Alternative diagrams in which heterolytic proton reduction mechanisms are considered have been much less developed.

In homogeneous systems, transition metals are ligated by molecules used for solvation and tuning of reactivity. These ligands, organic or inorganic, contribute first, second and outer sphere coordination effects, shown pictorially in Figure 1A, which have been shown dramatically affect catalytic efficiencies. This is due to an expansion of the reaction potential energy surface to include contributions of metal electron density, symmetry, electron and proton transfer rates and sterics. Indeed, ligands to homogeneous metal based proton reduction catalysts have expanded the thermodynamic and kinetic potential of other 1st row transition metals, but still none so far have matched or exceeded platinum.

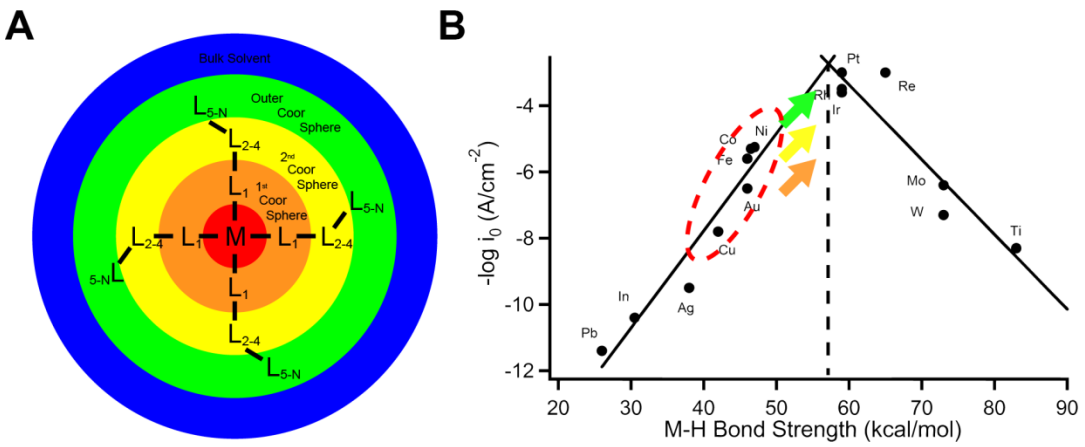

Figure 1.1 – Coordination environment of homogeneous metal catalysts and "Volcano" plots for the hydrogen evolution reaction (HER) of various metals. (A) Coordination environment of a metal based catalysts. "M" represents the metal of interest, lines represent bonds (four coordinate metal shown here), ligands directly bound to the metal are considered the first coordination sphere "L_1", the next three bound atoms "$L_{2\text{-}4}$" constitute a 2nd coordination sphere and the remaining ligands contribute to the outer coordination sphere before bulk solvent is encountered. (B) "Volcano" plot for HER activity from various metal based (111) surfaces. Data taken from Trasatti (current densities) and Kristalik (Heat of adsorption) et al.[11,12] Dashed red line indicates metal based properties for 1st row transition metals and arrows indicate coordination sphere effects on the multi-dimensional potential energy surface described in the text projected onto the M-H coordinate.

In light of the shortcomings of the established non-precious metal proton reduction catalysts, chemists often take inspiration from nature. In the early development of life on Earth, hydrogen has been proposed as a potential energy vector for growth coupled to CO_2 as a carbon source to make the building blocks of life before the great

oxidative event.[13] To do this efficiently, early organisms must have evolved enzymes that catalyze the oxidation of H_2 to drive CO_2 reduction to produce organic matter. The reverse reaction, reduction of protons, may also have served as a mechanism for maintaining homeostasis of the intracellular reduction potential. In 1934, Green and Strickland detailed their observations of reversible hydrogen production by *E. coli* bacteria catalyzed by an enzyme they termed hydrogenase (H_2ase).[14,15] Fast-forward nearly 80 years, and H_2ases are now understood as the gold standard in proton reduction catalysis with exceedingly high kinetic rates (>10,000 s^{-1}) and negligible over-potentials utilizing only nickel and iron.[16-18] Thus the H_2ases are examples of molecular systems with substantial outer sphere contributions to their catalytic efficiency which add multiple dimensions for improvement to the simple scheme depicted in standard volcano plots.

To understand the ligand (protein) contributions which aid in efficient proton reduction by H_2ases biomimetic and bioinspired chemists have developed structural and functional analogues of the H_2ases based on nickel and iron as well as cobalt.[19-23] A few notable examples in the very recent literature have achieved excellent turnover rates, reversibility or over-potentials, but none have captured all three aspects necessary to match the enzyme.[19-24] This is due to an inadequate understanding of the structural and functional aspects of H_2ases which result in their remarkable efficiency, a prerequisite for rational design of synthetic models.[25] For this reason, a detailed structurally consistent mechanistic understanding of the H_2ase enzymes will likely have direct implications on the development of efficient biomimetic catalysts for proton reduction that may be applicable to solar water splitting applications as well as other technologies such as fuel cells.

1.2 H_2ases: Cellular Function and Implications on Mechanism

H_2ases are exquisite catalysts for reversible proton reduction, but they have considerable phylogenic and functional diversity, which has been shown to correlate to their *in vitro* activity.[26] Phylogenically, the H_2ases can be classified based on two convergent evolutionary trajectories, resulting in two forms of the enzyme differentiated by the metal content of their active site cofactors and conserved functional protein core as [FeFe] and [NiFe] H_2ases.[27-29] The cellular and isolated activity of [FeFe] H_2ases has, in general, been shown to preferentially reduce protons, whereas the [NiFe] enzymes can be biased toward H_2 oxidation or H^+ reduction *in vitro* and *in vivo* depending on cellular conditions and/or the enzyme cofactor/subunit architecture.[26] The [FeFe] H_2ases are found primarily in anaerobic bacteria and react irreversibly with O_2. The [NiFe] H_2ases on the other hand are found ubiquitously in bacteria and archaea from both aerobic and anaerobic environments. It is thought that one evolutionary consequence of this is their reversible inhibition or complete tolerance to O_2. For this reason the [NiFe] H_2ases have attracted significantly more attention.[30] Both the [NiFe] and [FeFe] H_2ases has been observed to contain subclasses that further differentiate their functionality.[26]

1.2.1 [NiFe] H_2ases

[NiFe] H_2ases occur in bacteria and archaea super-kingdoms and are quite ubiquitous in both. A classification of the [NiFe] H_2ases has been developed based on their amino acid sequence near the cysteine active site binding domains which correlate to their *in vivo* function summarized in Figure 2.

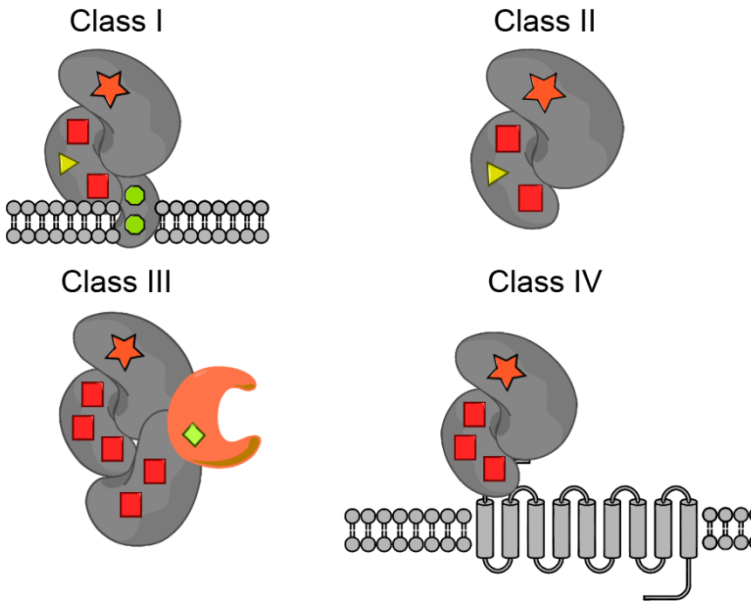

Figure 1.2 – Class description of [NiFe] H_2ases. Stars represent the [NiFe] active site, squares represent Fe_4S_4 clusters, triangles represent Fe_3S_4 clusters, diamonds represent Fe_2S_2 clusters and octagons represent hemes. Class III [NiFe] H_2ases contain an additional subunit with a cofactor binding domain shown in rose. Class I and IV [NiFe] H_2ases are membrane bound with the class IV containing additional subunits involved in proton pumping.

Class 1 [NiFe] H_2ases are heterotrimeric proteins containing a large subunit (~60kDa) harboring the $(S^T_{cys})_2Ni(S^B_{cys})_2Fe(CO)(CN)_2$ active site (where S^T indicates terminal and S^B indicates bridging μ-bound to the iron), a small subunit (~30kDa) with 1-3 FeS clusters and a small membrane integral di-heme cytochrome subunit which is the site of electron exchange with the quinone pool.[31-33] This class of H_2ases is involved in H_2 oxidation coupled to quinone reduction, which facilitate the overall cellular reduction of NO_3^-, SO_4^{2-}, fumerate, CO_2 or O_2 depending on the organism and conditions.[34] Class 2 [NiFe] H_2ases are very similar to class 1 H_2ases, except they lack the membrane targeting

and translocation (MTT) or twin arginine translocation (TAT) labels of the class 1 H_2ases, thus they remain in the cytoplasm as soluble enzymes without the membrane integral cytochrome subunit.[35,36] Their cellular function involves the sensing of H_2 for transcription of class 1 H_2ases or recycling H_2 generated by nitrogen fixation. This class of H_2ase is also thought to interact with the quinone pool.[28] Being linked to the quinone pool, both these classes of enzyme typically function in H_2 oxidation because their physiological acceptors are thermodynamically incapable of driving proton reduction. Class 3 [NiFe] H_2ases are similar to class 1 and 2 [NiFe] H_2ases, except they contain additional subunits that interact with cofactors (such as F_{420}, Ferredoxin, NAD(P)H and flavins).[28,37] This class has been termed bi-directional based on its ability to either oxidize hydrogen or reduce protons depending on cellular conditions.[26,37] This bi-directionality is a direct result of the interaction with redox cofactors that are in thermodynamic equilibrium with the H_2/H^+ couple. The final class of H_2ases, class 4, are membrane integral multimeric H_2ases that typically function in the reduction of protons to H_2 with the concomitant generation of a proton gradient from a complex I like set of subunits.

Despite a wide variety of cellular functions, all [NiFe] H_2ases characterized to date appear to be structurally and spectroscopically very similar, particularly with respect to their large and small subunits harboring the active site and the FeS cluster chain.[26,38,39] In an attempt to reconcile the wide variability in cellular function relative to the highly similar spectroscopic properties of their active sites, protein film electrochemistry has been applied to these enzymes which has suggested that these differences are based on the solvent exposed cofactors, but this hypothesis is still under investigation.[40-42] Specifically, classes I and II [NiFe] H_2ases appear to function only in H_2 oxidation *in*

vivo, but function bi-directionally quite well on a pyrolytic graphite electrode in the absence of their cytochrome cofactor, a high potential redox cofactor. Differences still remain among classes I and II [NiFe] H_2ases and those which function bi-directionally *in vivo*, or are biased towards proton reduction.[40,43] Thus, the underlying mechanism of the *in vivo* and *in vitro* directionality is still unclear.

1.2.2 [FeFe] H_2ases

[FeFe] H_2ases are more infrequently observed biologically and are found exclusively in bacteria and eukaryote super-kingdoms. As a result, their biological structure-function based classification is slightly less rigorous.[26,34] The minimal [FeFe] H_2ase contains only the so-called H-cluster ligated to a minimal protein scaffold (~45 kDa) through a single cysteine residue.[44,45] The exact nature of the active site has been characterized by x-ray crystallography, FTIR and cw/pulsed EPR spectroscopy, and is best described as a Fe_4S_4 cubane cluster attached to the catalytic center $(CO)(CN)Fe(CO)(S_2C_2H_6N)Fe(CO)(CN)$ by the single bridging cysteine residue which anchors the active site.[46-50] This minimal protein, which only contain the catalytic site and no additional cofactors, is found exclusively in green algae. It is interesting when compared to the [NiFe] H_2ases, since it does not require additional cofactors for activity. There is a conserved domain of ~350 residues that harbors the H-cluster in all [FeFe] H_2ases. Other [FeFe] H_2ases have been observed to contain additional FeS cofactors which vary significantly in their amino acid content beyond the conserved domains.[45,51] The diversity of [FeFe] H_2ases also includes multi-subunit enzymes, some of which are proposed to be involved in electron bifurcation where the two electrons from H_2 are used

to reduce a high and low potential acceptor "straddling" the H_2 couple.[52-54] Unfortunately, the biochemical and microbiological classifications of [FeFe] H_2ases are still being developed.[26,28]

1.3 H_2ases Chemical Mechanism

Following the discovery of the H_2 production activity of numerous micro-organisms biochemists began investigating the chemical nature of the enzyme responsible for this cellular activity. In landmark experiments, using ortho/para H_2 exchange, Rittenburg *et al.* demonstrated that the mechanism of action in the H_2ase of E. coli involved heterolytic cleavage of H_2 into a hydride and a proton, a distinct mechanism from the homolytic cleavage of platinum.[55] Despite the fundamentally different mechanism, the kinetic rates and over-potential were observed to be very similar to bulk platinum.[17,56] Basic enzymology and kinetics studies showed that the enzyme would catalyze H/D exchange and showed different rates of H_2 production relative to H_2 oxidation indicating a "bias" towards H_2 oxidation.[37,57-61] Additionally, the measured kinetic isotope effects were appreciable, but moderate at between 2-4 for proton reduction, and have not been examined for H_2 oxidation.[62-65] The enzyme was also shown to be inhibited reversibly by O_2 and CO as well as acetylene.[62,64,66,67] Reactivation after O_2 inactivation required extended incubation with reducing agents or H_2, and the reactivation time was highly dependent on the conditions used for oxidative inactivation and the organism from which the enzyme was procured.[68-71] In other enzymes from other micro-organisms O_2 reactivity irreversibly abolished the H_2ase activity. This was later shown to correlate with metal content of the enzyme active site (diiron rather than nickel-

iron active sites) establishing a set of convergently evolved phylogenetically distinct H_2ases.[72,73]

1.3.1 [NiFe] H_2ases

Bioinorganic chemists began examining the metal responsible for H_2 activation and multiple groups proposed nickel based on metal analysis and EPR observations of a S=1/2 trivalent species with hyperfine interactions observed after cell growth under ^{61}Ni.[74-77] This resonance responded reversibly to H_2 levels, growing in under oxidizing conditions when not present and decaying under mild reductive treatment.[74-77] This opened up a large area of research into the electronic structure of the nickel environment in the hydrogenase as well as biochemical efforts to isolate the H_2ase enzymes from various organisms.[30,78]

Using Mössbauer spectroscopy, metal analysis and EPR spectroscopy, the nickel containing H_2ases were determined to contain approximately 12 additional iron atoms, and 12 acid labile sulfides.[79-81] One of the iron atoms was bound to the active site, establishing a bimetallic [NiFe] active site, and others that were integral to Fe_4S_4 and Fe_3S_4 clusters observed in other enzymes and redox active proteins known at the time.[79-81] More sophisticated EPR spectroscopy, specifically ENDOR and HYSCORE spectroscopy sensitive to nuclear spins within coupling distance to the probed electron spin, revealed that there was a strongly associated, solvent exchangeable proton at the [NiFe] active site that was proposed to be a bridging hydride in the H_2 activated trivalent nickel state.[82-85]

Significant advancement in the understanding of these enzymes came with the report of an X-ray crystal structure of a [NiFe] H_2ase from *Desulfovibrio gigas*, which revealed the overall protein architecture shown in Figure 3.[31-33] The structure as well as numerous subsequent structures displayed a number of interesting characteristics including: the FeS cluster organization which formed an apparent molecular wire to the buried active site from the surface exposed distal Fe_4S_4 cluster, the unique active site ligated to the enzyme including three diatomic ligands to the iron, proton transport pathways and hydrogen diffusion channels. Studying CO reactivity, a known inhibitor of the [NiFe] H_2ases, the diatomic ligands to the active site were identified as one CO and two CNs.[86-88] These ligands were shown to be highly sensitive to the electronic state of the enzyme irrespective of a paramagnetic state of the nickel ion, yielding a more universal probe of active site reactivity revealing new stable steady states.[88-90]

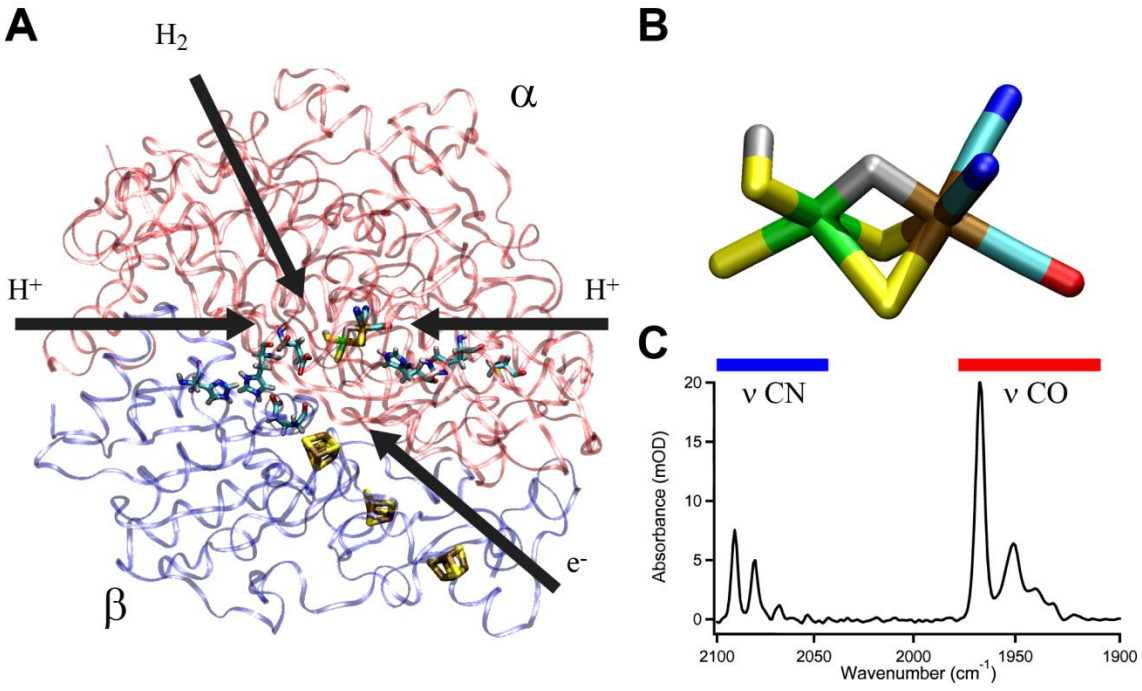

Figure 1.3 – Enzyme architecture, active site structure and FTIR spectrum of [NiFe] H_2ases. (A) Protein architecture of the *D. gigas* class I [NiFe] H_2ase (PDB code 4U9H). FeS clusters are shown in brown and yellow, with an arrow indicating electron flow in the H_2 production. Amino acids are shown that are proposed to be involved in proton transport to the active site during H_2 production. The active site is shown with an arrow indicating the tunnel for H_2 approach. (B) [NiFe] H_2ase active site in the Ni_a-SR form. Yellow represents sulfur, brown represents iron, cyan represents carbon, green represents nickel, silver represents hydrogen, blue represents nitrogen and red represents oxygen. (C) FTIR spectrum for the *Pyrococcus furiosus* class III soluble H_2ase 1 (SHI). Blue and red labels highlight CN and CO absorbance regions of the spectrum respectively.

Using both infrared and EPR spectroscopies, coupled with electrochemical control, a mechanism, based on observed equilibrium states has been proposed and is detailed in Figure 4.[30] This mechanism involves two n=1 proton coupled reduction processes which have been shown to be in thermodynamic equilibrium with the H_2/H^+ couple denoted Ni_a-S, Ni_a-C and Ni_a-SR representing catalytically active states with Nickel species which are EPR Silent, aCtive and Silent but Reduced. These equilibrium states have been observed in numerous [NiFe] H_2ases and appear to be present among all [NiFe] H_2ases with only slight spectrally distinguishable differences implying a remarkably similar active site electronic structure across various organisms and classes of [NiFe] H_2ases. Since the vibrational frequency of the π-acceptor CO ligand is highly susceptible to the electron density and thus the electronic structure of the active site, the similarity observed among the [NiFe] H_2ases from various micro-organisms and of

various biological functions indicates a similar catalytic mechanism. The infrared spectral properties of these states for several [NiFe] H_2ases are reported in Table 1, where it is apparent that the both the absolute frequency and spectral shift between active states are highly conserved.

	Absolute CO Frequency (cm^{-1})			Frequency Shift (cm^{-1})		
Organsim (Class)	Ni_a-S	Ni_a-C	Ni_a-SR	Δν S-C	Δν C-SR	Ref.
A. aeolicus (I)	1927	1949	N.D.	-22	N.A.	[91]
A. vinosum (III)*	1947	1969	1955	-22	14	[92]
A. vinosum (I)	1932	1951	1936	-19	15	[87]
D. fructosovorans (I)	1933	1951	1938	-18	13	[93]
D. gigas (I)	1934	1952	1940	-18	12	[88]
D. vulgaris (I)	1943	1961	1948	-18	13	[89]
R. eutropha (I)	1936	1957	1948	-21	9	[94]
R. eutropha (II)	1943	1962	N.D.	-19	N.A.	[95]
R. eutropha (III)	n.d.	1961	1946	N.A.	15	[96]
Synechocystis (III)	1947	1968	1955	-21	13	[97]
		Average		-20	13	
		Standard Deviation		1.6	1.8	

Table 1.1 – Summary of infrared frequencies of known [NiFe] H_2ase steady states Ni_a-S, Ni_a-C and Ni_a-SR in thermodynamic equilibrium with H_2/H^+ and their relative spectral shifts. * Indicates data were reinterpreted based on subsequent data from other type III H_2ases. Original assignment was that 1969 cm^{-1} peak corresponds to Ni_a-S and 1947 cm^{-1} corresponds to Ni_a-C and 1955 cm^{-1} was unassigned.

Protein film voltammetry (PFV) has also been established as a useful experimental tool for the investigation the [NiFe] H_2ase mechanism.[69] In PFV experiments, proteins physisorbed onto an electrode surface directly exchange electrons with the electrode, removing the need for external chemical mediators or assay reactants

and enabling the rapid exchange of solution conditions.[98] A maximal catalytic rate was determined for the soluble [NiFe] H_2ase of *Allochromatium vinosum* to be 1,000-9,000 s^{-1} for H_2 oxidation and 500-1,000 s^{-1} for H_2 production.[16] Due to this exceedingly high turnover frequency (TOF) directly determining the species involved in catalysis has been difficult by conventional stopped-flow or freeze-quenching techniques due to the slow mixing time required for both methods.[99,100] Rapid mixing and freeze quenching experiments have indeed been performed on the [NiFe] H_2ases which have shown that the proposed intermediates Ni_a-S, Ni_a-C and Ni_a-SR react with or result from reactions with H_2 on timescales faster than the stopped-flow or freeze-quenching timescales.[99,100] While these results alone do not establish the kinetic competency of these intermediates they do indicate that their involvement in the mechanism of these enzymes is very probable. The cumulative mechanistic picture based on these results is described in Figure 4, which is compiled from extensive work and is reproduced in numerous recent reviews.[30,101-104]

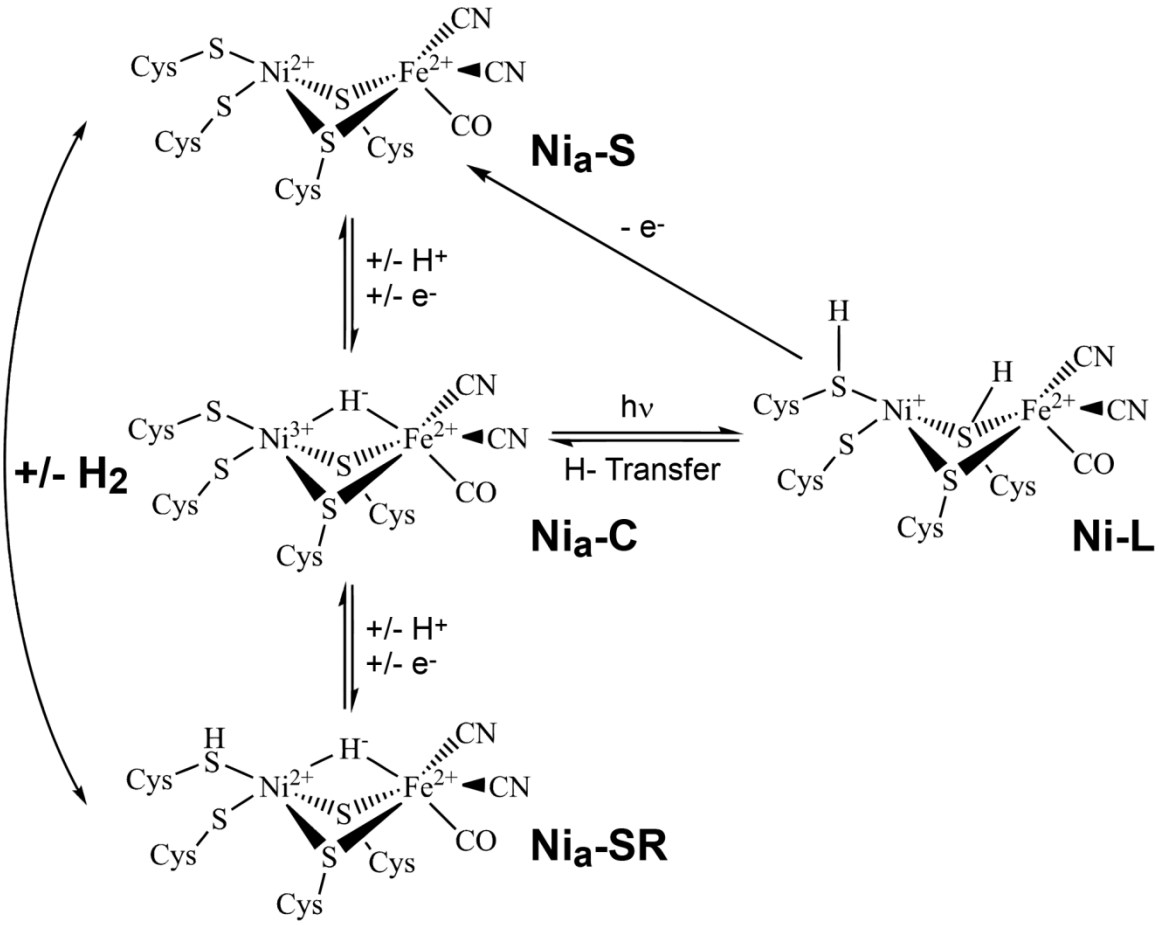

Figure 1.4 – Proposed catalytic mechanism of proton reduction/H_2 oxidation by [NiFe] H_2ases. Ni-L represents a photo-chemical product of Ni_a-C that has been proposed to be an intermediate in the formation of Ni_a-C from Ni_a-S.

1.3.2 [FeFe] H_2ases

As stated above, the chemical properties of the [FeFe] H_2ases are much less understood due to their extreme irreversible oxygen sensitivity and their smaller prevalence in life on earth.[72,73] Based on the few [FeFe] H_2ases spectroscopically and electrochemically investigated thus far, a rudimentary understanding of their reactivity and active site chemistry has emerged.[105] [FeFe] H_2ases were first identified from *Desulfovibrio* and *Clostridium* micro-organisms. These enzymes contained no nickel and

exhibited anomalous EPR and Mössbauer properties in their oxidized form indicating non-heme iron with a g_z of 2.10.[106-109] EPR, FTIR and x-ray crystallography, analogously to the [NiFe] H_2ases, have aided in the determination of the overall enzyme structure illustrated in Figure 5.

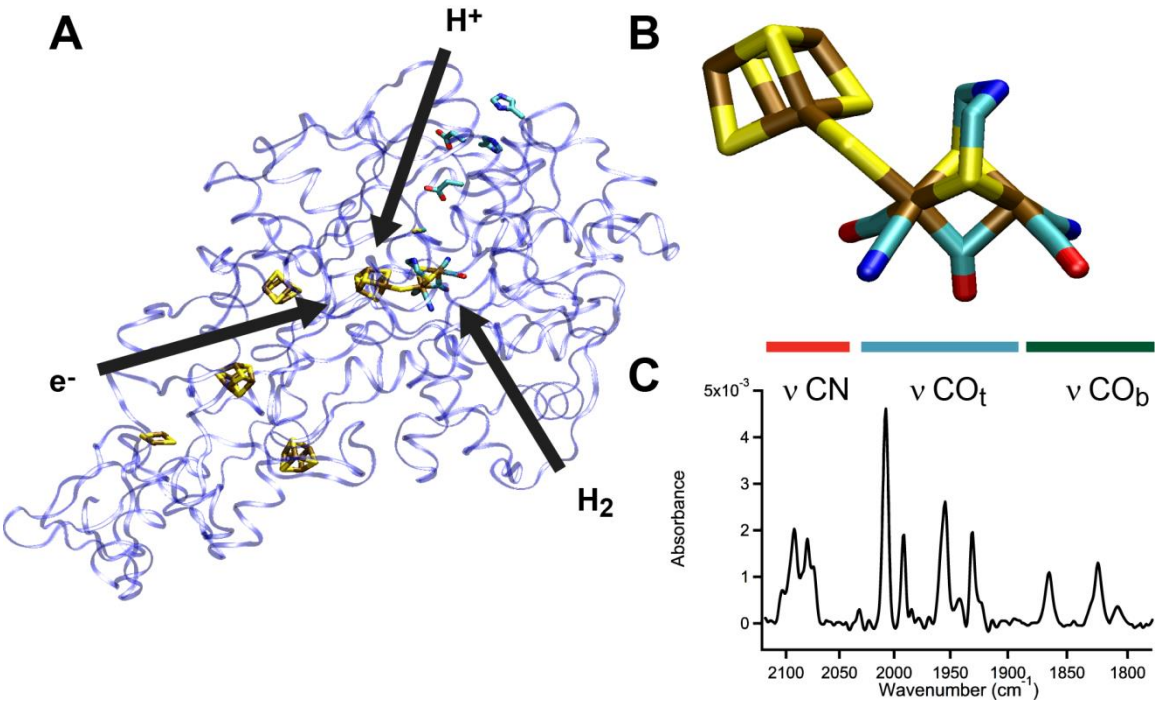

Figure 1.5 – Enzyme architecture, active site structure and FTIR spectrum of [FeFe] H_2ases. (A) Protein structure of the [FeFe] H_2ase from *Clostridium pasteurianum* (PDB code 3C8Y). Protein structure shown in blue, iron in brown, sulfur in yellow, carbon in cyan, oxygen in red and nitrogen in blue. (B) H-cluster structure for [FeFe] H_2ases. (C) FTIR spectrum of the H-cluster for the [FeFe] H_2ase of *Thermatoga maritimia.*

In spectroelectrochemical titrations, this g_z 2.10 resonance was found to disappear with an apparent reduction potential of -400 mV vs. NHE at pH 8.0 converting to a

diamagnetic state.[49,50,106,108,110,111] By complementary FTIR measurements, these states were assigned to be in thermodynamic equilibrium with H_2/H^+ and termed H_{ox} and H_{red}. This conversion was found to be proton coupled with a pH dependence of -59 mV/pH.[47,111-113] Based on high level EPR and FTIR spectroscopy, the H_{ox} state has been assigned to a formally $Fe(I)Fe(II)Fe_4S_4^{2+}$ state where the unpaired electron is located on the di-iron center.[50,106,109-111] The H_{red} state was found to exist as a doubly reduced core complex consistent with a formally $Fe(I)Fe(I)Fe_4S_4^{2+}$ active site cluster where the second electron is again located on the di-iron core.[112,114,115] In the majority of [FeFe] H_2ases these two states are the only isolatable states in redox titrations, but interestingly in the FeS cluster free [FeFe] H_2ase from *Chlamydomonas reinhardii,* a third further reduced species was observed, termed H_{sred} which was spectroscopically consistent with a $Fe(I)Fe(I)Fe_4S_4^{+}$ configuration.[47,116,117] This state is not observed in the other [FeFe] H_2ases that contain additional FeS clusters presumably because of the instability of this state relative to the reduction neighboring FeS clusters.

		Spectral Position (cm^{-1})				
State	Organism	CN (1)	CN (2)	CO (1)	CO (2)	CO_B
H_{inact}	Dd	2106	2087	2007	1983	1848
H_{trans}	Dd	2100	2075	1983	1977	1836
H_{ox}	Dd	2093	2079	1965	1940	1802
	Cr	2088	2072	1964	1940	1800
	Cp	2086	2072	1971	1948	1802
H_{red}	Dd	2093	2079	1965	1916	1894
	Cr	2083	2070	1935	1891	1793
H_{sred}	Cr	2070	2026	1954	1919	1882

Table 1.2 - Summary of infrared frequencies of known [FeFe] H_2ase steady states H_{ox}, H_{red} and H_{sred} in thermodynamic equilibrium with H_2/H^+ as well as O_2 inactivated states H_{trans} and H_{inact}. COB indicates bridging CO, which switches to a terminal binding motif in the H_{sred} state and potentially in the H_{red} state of [FeFe] H_2ases with ancillary FeS clusters. Dd indicates *Desulfovibrio desulfuricans, Cp* indicates *Clostridium pasteurianum* and *Cr* indicates *Chlamydomonas reinhardii.*

Again, as with the [NiFe] H_2ases, the spectral properties of these proteins are reasonably similar (albeit with few examples, Table 1.2) among the various organisms studied to date. One marked difference is the nature of the bridging CO, which switches to a terminal binding motif in the H_{sred} state of the [FeFe] H_2ase from *Chlamydomonas reinhardtii*, but appears to occur in the H_{red} state of the [FeFe] H_2ase from *Desulfovibrio desulfricanus*. Based on these steady states a mechanism has been proposed which is summarized in Figure 6 based on very recent literature.[47,112,113,116]

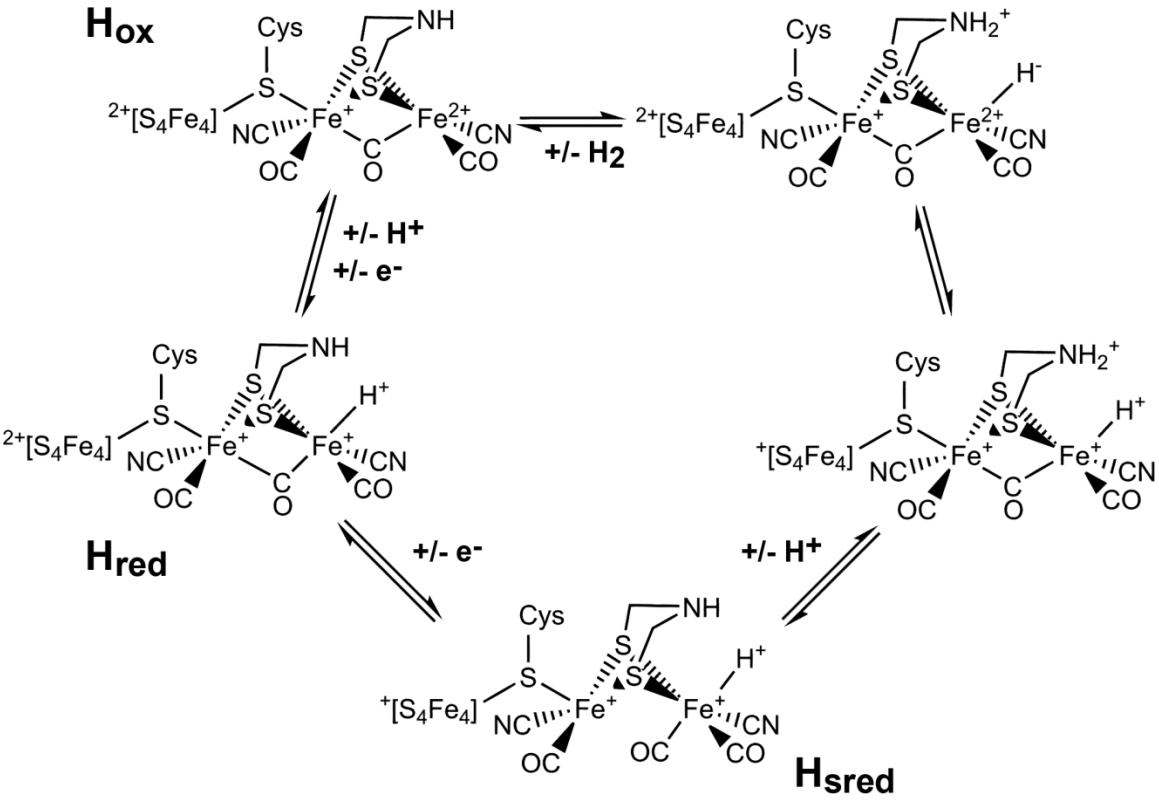

Figure 1.6 – Proposed [FeFe] mechanism for H_2 production/oxidation based on equilibrium states. Unnamed states are proposed, but never observed experimentally.

The [FeFe] H_2ases typically function with a 10 fold higher rate for H_2 production over H_2 oxidation.[118] They also catalyze the H/D exchange reaction, a similar reactivity as that observed in the [NiFe] H_2ases.[119] Point mutations proposed to disrupt the proton transfer reaction have been shown to induce changes in the redox properties of the H-cluster, exhibiting drastically different behavior when protons are limiting.[113] This may indicate that the enzyme architecture eliminates off pathway reactivity by supplying protons and electrons with high efficiency.

There are several common aspects of the mechanistic formulations of both [NiFe] and [FeFe] H_2ases.[30,38,120] First and most importantly, the proposed intermediate states have only been characterized in the steady state regime and thus there is no direct

evidence for their involvement in catalysis.[99,100] Secondly, the observed intermediate states are not separated by elementary processes and involve both proton and electron transfer which could be coupled or decoupled. Finally, the environmental contributions to stabilization of the proposed intermediates are not clear. For these reasons, the mechanisms of both [NiFe] and [FeFe] H_2ases are far from established and are areas of continued research.

1.4 Practical Applications of Fast Kinetic Analysis

Mechanistic investigation of enzymes necessitates kinetics, the study of rates of chemical reactions.[121] There are two general methods for studying kinetics of enzymes; steady state kinetics, which describes the rate of change of chemical species on timescales slower than the reaction of interest and pre-steady state kinetics which describes the rate of change of chemical species on timescales faster than the reaction of interest.[121] Steady state kinetics has been and continues to be extremely useful, but its inherent limitations are often an obstacle in the development of greater chemical understanding, particularly for complex reactions. This is because steady state methods typically involve keeping the concentration of one component of the reaction in significant excess to continue reactivity for long observation periods. Conversely, in pre-steady state kinetics, the concentration of a reactant is rapidly increased or decreased and the relaxation back to equilibrium is monitored as a function of time. An example problem associated with this limitation is shown in Figure 7. Here two reactions are considered, one involving two sequential uni-molecular reactions in which species A is converted to species B which subsequently forms species C by two irreversible chemical

reactions and a second involving three sequential uni-molecular reactions where species A is converted to intermediate X, then to B and finally forming species C. In the former, three potential kinetic scenarios can be described; $k_1 < k_2$, $k_1 \sim k_2$ or $k_1 > k_2$ all of which will result in different populations of the intermediate species B. In this situation, if $k_1 << k_2$ then no intermediate will be observed in either steady state or pre-steady state kinetics due to rapid decay of the intermediate to C. If $k_1 > k_2$, say 1000 s^{-1} and 100 s^{-1} as depicted in Figure 7, the intermediate B may be observed in steady state kinetics as well as pre-steady state kinetics since some residual intermediate lasts longer than k_2 the rate determining step (100 s^{-1}). If an additional intermediate, termed species X, is formed before the formation of B and the rate of formation of X is fast relative to the rate determining step of the overall chemical reaction, say 500 s^{-1}, then intermediate X forms and completely decays faster than the overall rate of ~100 s^{-1}. Depending on the analytic specificity and time resolution, numerous potential outcomes could be observed experimentally. In the steady state regime, time resolution is limited to timescales slower than the slowest reaction component, in this case >10 ms. Considering the first scenario, slow transition of A to C is observed with no buildup of intermediate B. In the second case, a modest buildup of intermediate is observed, but the reaction is completed rapidly. In the third case, substantial intermediate is built up, but product formation is identical to the first scenario. Additionally, with the modest rate constants applied of 100-1,000 s^{-1}, nearly all details of the reaction progress are complete in 40 ms, which is slower than most steady state methods can observe. With insufficient time resolution, these reactions may appear to be identical but with sufficient time resolution the differences are clear. This thought experiment demonstrates that in simple systems steady state kinetics is still

a powerful approach for investigating mechanisms, but for the many chemical reactions involving more than two steps and rates that can range from femtoseconds to seconds the steady state method of kinetic analysis can leave critical details unobservable. Thus the use of pre-steady state kinetics is ideally suited for the study of such reactions.

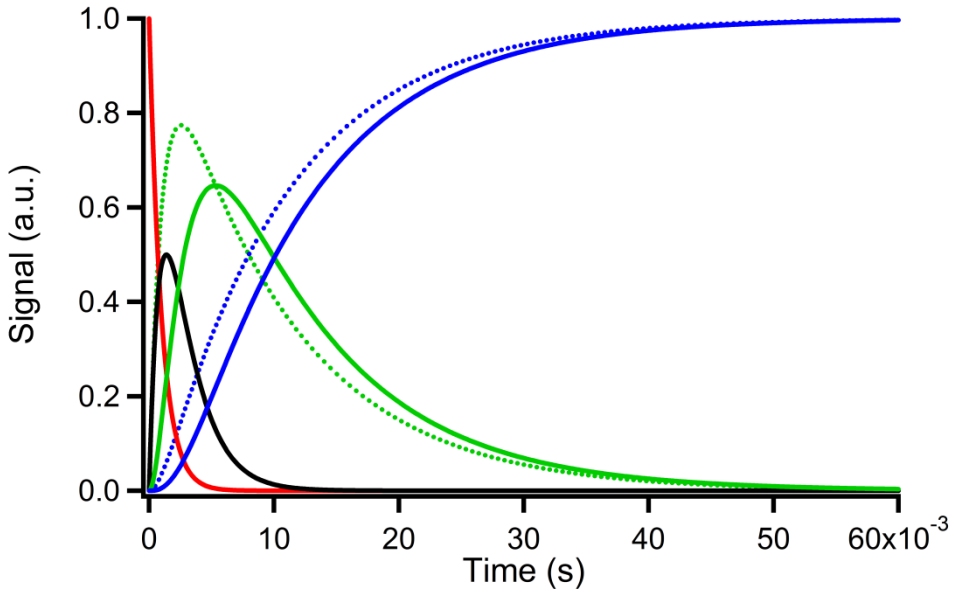

Figure 1.7 – Simulated reaction kinetics for an irreversible two-step and three step uni-molecular reactions with varying rate constants. Kinetic simulation parameters: $[A]_0 = 1$ (red), $[X]_0 = 0$ (black), $[B]_0 = 0$ (green) and $[C]_0 = 0$ (blue), for reaction 1 (dotted lines), k_1=1000 s^{-1} and k_2 = 100 s^{-1}, for reaction 2 (solid lines), k_1 = 1000 s^{-1}, k_2 = 500 s^{-1} and k_3 = 100 s^{-1}.

Practically, pre-steady state kinetic studies require two features of the analytical method: (1) that the mixing time of reactants is faster than the reaction rate and (2) an appropriate analytic detection method is used which allows for chemical information to be collected faster than the reaction rate. To mix reactants on a rapid timescale there are

numerous methods, each with their own experimental time resolution characteristics, that have been applied to the study of condensed phase chemical systems including: stopped flow mixing which can probe reactions with rates near 10^3 s^{-1}, continuous flow mixing which can probe reactions with rates near 10^5 s^{-1} and photo-chemical release which can probe reactions with rates of 10^{11} s^{-1}. Of these methods photo-chemical release is by far the most valuable due to the very high time resolution, a consequence of the reactants already being mixed (diffusion of reactants may still be required, but on a much smaller length scale). Analytical methods for rapidly detecting chemical reactions also have intrinsic time resolution, chemical information and sensitivity limitations. Additionally, for fast mixing experiments, volumes are minimized which decreases the mixing time, but makes conventional spectroscopic methods difficult. Consequentially these methods tend to utilize fluorescence spectroscopy, which is only suited for specialized applications. Photochemical release has the advantage of being experimentally amenable to most conventional fast spectroscopic techniques.

The photo-chemical initiation method requires a component of the system under investigation to contain photo-labile reactant of interest. Photo-dissociation of the reactant is achieved in the excited state and the release timescale is determined by the excited state dissociation pathway, which can range from the timescale of a single bond vibration (10^{12}-10^{13} s^{-1}) to typical fluorescent lifetimes (10^6-10^{10} s^{-1}). Once liberated from the parent cage molecule, the reactants are free to diffuse and react on molecular length scales. For rapid mixing, diffusional length scales are typically a few microns at best due to optical constraints of probe methods, whereas the diffusion lengths for the photo-release of molecular caged reagents at millimolar concentrations are <6 nm. Since

diffusion time scales linearly with length in a one dimensional sense, this results in a 10^3 rate enhancement of collisional frequency. An additional geometric benefit is that within the optically excited volume, assuming uniform spatial power density, the concentration jump is homogeneous, thus simplifying the data analysis.

Reports of the use of photo-chemical reaction initiation coupled with time resolved spectroscopy are rare relative to conventional kinetic analysis techniques, but are becoming increasingly more common as the chemical library of photo-caged reactants increases and spectroscopic methodology becomes more powerful. Critical and ubiquitous reactions such as protein folding, ligand binding and catalysis have been probed at unprecedented timescales with very rich chemical information through the aforementioned photo-release and fast detection methodology.[122-124]

1.5 Hypothesis and Scope of This Thesis

As detailed above, H_2ases represent the best known proton reduction catalysts to date based on their fast, efficient, stable and reversible catalysis. To develop molecular catalysts which match or exceed this reactivity, a detailed understanding of the chemical mechanism of these enzymes is critical. Central aspects of the enzymatic mechanism of the H_2ases with respect to development of artificial catalysts regard the structure and function of the catalytic organometallic active site cofactor and the outer-sphere contributions to catalysis of the protein matrix itself. Determination of the functional role of the organometallic active site requires knowledge of the reactivity towards its substrates; electrons, protons and H_2. Similarly, determination of the functional role of the protein scaffold requires knowledge of the substrate and product transport properties

such as proton, electron and gas diffusion. The transport properties of products and substrates through the enzyme as well as active site chemistry necessarily occur faster than the overall catalytic rate. Since catalytic rates of most H_2ases lie in the range of 10^2-10^3 s^{-1}, the fundamental processes involved in catalysis must occur faster, which presents an experimental challenge, as rapid mixing techniques used to initiate chemical reactions on rapid timescales cannot achieve time resolutions much faster than 10^3 s^{-1}. Thus experimental methodologies capable of initiating catalysis on timescales much faster than the overall catalytic rate could probe directly the substrate transport properties and active site chemical reactivity. It is expected that if such an experiment could be performed with sufficient temporal resolution and analytical specificity, new insight may be gained on the reactivity and mechanism of the H_2ases. These insights are critical since structural models of the active site alone do not capture critical aspects of the enzyme function, particularly concerning the negligible over-potentials and reversibility of the H_2ases. The central motivation of this thesis and a governing hypothesis can be summarized as follows:

"Elements of the [NiFe] and [FeFe] hydrogenase enzyme architectures facilitate, modulate and tune the proton reduction activity by the active site metallocofactor, allowing efficient and reversible catalysis."

To address this hypothesis, both conventional steady state, as well as novel pre-steady state kinetics, were utilized to elucidate the elementary processes involved in enzymatic action. Conventional steady state kinetics revealed a product release rate

determining step, a slow intramolecular proton transfer step and rapid gas diffusion through the protein matrix, but yielded little quantitative information on fundamental electron and proton transfer reactions or active site chemistry. Pre-steady state methods capable of addressing these shortcomings directly were thus developed through photo-initiation of the reductive chemistry of the H_2ases by photo-induced electron transfer or photo-induced chemical potential jumps. Additionally, analytical instrumentation was developed for the direct spectroscopic investigation of active site dynamics and intermolecular electron transfer through nanosecond resolved infrared and visible spectroscopy respectively. Applying both photo-initiation and fast time resolved spectroscopy to the pre-steady state kinetic analysis of reactions of H_2ases allowed for the simultaneous observation of electron and proton transfer as well as active site photochemistry. Through chemical control of the initial conditions prior to photo-initiation, specific details of the catalytic mechanism of the [NiFe] H_2ase from *Pyrococcus furiosus* were deduced including the mechanism of active site proton-coupled reduction revealing an important role of proton tunneling in H_2ase chemistry. This electron-proton tunneling mechanism is likely involved in the energetic leveling of the catalytic mechanism, avoiding high energy intermediates which may enable reversibility. Furthermore, the rates of intramolecular ET and proton transfer were determined to be significantly faster than the rate determining steps in catalysis, indicating the catalytic rate is unhindered by the protein scaffold. Thus the hypothesis governing this thesis was indeed verified, although a complete understanding of the proton and electron transfer dynamics has not been achieved, thus the work has opened up numerous new topics of research in the H_2ases.

1.6 References

1 Lewis, N. S. & Nocera, D. G. Powering the planet: chemical challenges in solar energy utilization. *P Natl Acad Sci USA* **103**, 15729-15735, (2006).

2 Gray, H. B. Powering the planet with solar fuel. *Nat Chem* **1**, 7-7, (2009).

3 Lewis, N. S. Toward cost-effective solar energy use. *Science* **315**, 798-801, (2007).

4 Crabtree, G. W. & Lewis, N. S. Solar energy conversion. *Phys Today* **60**, 37-42, (2007).

5 Turner, J. A. A realizable renewable energy future. *Science* **285**, 687-689, (1999).

6 Du, P. W. & Eisenberg, R. Catalysts made of earth-abundant elements (Co, Ni, Fe) for water splitting: Recent progress and future challenges. *Energ Environ Sci* **5**, 6012-6021, (2012).

7 Steele, B. C. H. & Heinzel, A. Materials for fuel-cell technologies. *Nature* **414**, 345-352, (2001).

8 Parsons, R. The Rate of Electrolytic Hydrogen Evolution and the Heat of Adsorption of Hydrogen. *T Faraday Soc* **54**, 1053-1063, (1958).

9 Sabatier, P. Announcement. Hydrogenation and dehydrogenation for catalysis. *Ber Dtsch Chem Ges* **44**, 1984-2001, (1911).

10 Quaino, P., Juarez, F., Santos, E. & Schmickler, W. Volcano plots in hydrogen electrocatalysis - uses and abuses. *Beilstein J Nanotech* **5**, 846-854, (2014).

11 Krishtalik, L. I. *Advances in Electrochemistry and Electrical Engineering*. Vol. 3 (Interscience, 1970).

12 Trasatti, S. Work Function, Electronegativity, and Electrochemical Behavior of Metals .3. Electrolytic Hydrogen Evolution in Acid Solutions. *J Electroanal Chem* **39**, 163-&, (1972).

13 Wachtershauser, G. From volcanic origins of chemoautotrophic life to Bacteria, Archaea and Eukarya. *Philos T R Soc B* **361**, 1787-1806, (2006).

14 Farkas, A., Farkas, L. & Yudkin, J. The decomposition of sodium formate by bacterium doll in the presence of heavy water. *P R Soc Lond B-Conta* **115**, 373-379, (1934).

15 Green, D. E. & Stickland, L. H. Studies on reversible dehydrogenase systems. I. The reversibility of the hydrogenase system of Bact. coli. *Biochem J* **28**, 898-900, (1934).

16 Pershad, H. R. *et al.* Catalytic electron transport in Chromatium vinosum [NiFe]-hydrogenase: Application of voltammetry in detecting redox-active centers and establishing that hydrogen oxidation is very fast even at potentials close to the reversible H+/H-2 value. *Biochemistry-Us* **38**, 8992-8999, (1999).

17 Jones, A. K., Sillery, E., Albracht, S. P. J. & Armstrong, F. A. Direct comparison of the electrocatalytic oxidation of hydrogen by an enzyme and a platinum catalyst. *Chem Comm*, 866-867, (2002).

18 Madden, C. *et al.* Catalytic Turnover of [FeFe]-Hydrogenase Based on Single-Molecule Imaging. *J Am Chem Soc* **134**, 1577-1582, (2012).

19 Tard, C. & Pickett, C. J. Structural and functional analogues of the active sites of the [Fe]-, [NiFe]-, and [FeFe]-hydrogenases. *Chem Rev* **109**, 2245-2274, (2009).

20 Helm, M. L., Stewart, M. P., Bullock, R. M., DuBois, M. R. & DuBois, D. L. A Synthetic Nickel Electrocatalyst with a Turnover Frequency Above 100,000 s(-1) for H-2 Production. *Science* **333**, 863-866, (2011).

21 Camara, J. M. & Rauchfuss, T. B. Combining acid-base, redox and substrate binding functionalities to give a complete model for the [FeFe]-hydrogenase. *Nat Chem* **4**, 26-30, (2012).

22 Han, Z. J., Qiu, F., Eisenberg, R., Holland, P. L. & Krauss, T. D. Robust Photogeneration of H-2 in Water Using Semiconductor Nanocrystals and a Nickel Catalyst. *Science* **338**, 1321-1324, (2012).

23 Ogo, S. *et al.* A Functional [NiFe]Hydrogenase Mimic That Catalyzes Electron and Hydride Transfer from H-2. *Science* **339**, 682-684, (2013).

24 Dempsey, J. L., Brunschwig, B. S., Winkler, J. R. & Gray, H. B. Hydrogen Evolution Catalyzed by Cobaloximes. *Accounts Chem Res* **42**, 1995-2004, (2009).

25 Kaur-Ghumaan, S. & Stein, M. [NiFe] hydrogenases: how close do structural and functional mimics approach the active site? *Dalton Trans*, (2014).

26 Vignais, P. M. & Billoud, B. Occurrence, classification, and biological function of hydrogenases: An overview. *Chem Rev* **107**, 4206-4272, (2007).

27 Wu, L. F. & Mandrand, M. A. Microbial Hydrogenases - Primary Structure, Classification, Signatures and Phylogeny. *FEMS Microbiol Lett* **104**, 243-270, (1993).

28 Vignais, P. M., Billoud, B. & Meyer, J. Classification and phylogeny of hydrogenases. *FEMS Microbiol Rev* **25**, 455-501, (2001).

29 Shima, S. & Thauer, R. K. A third type of hydrogenase catalyzing H-2 activation. *Chem Rec* **7**, 37-46, (2007).

30 Lubitz, W., Ogata, H., Rudiger, O. & Reijerse, E. Hydrogenases. *Chem Rev* **114**, 4081-4148, (2014).

31 Volbeda, A. *et al.* Crystal-Structure of the Nickel-Iron Hydrogenase from Desulfovibrio-Gigas. *Nature* **373**, 580-587, (1995).

32 Volbeda, A. *et al.* Structure of the [NiFe] hydrogenase active site: Evidence for biologically uncommon Fe ligands. *J Am Chem Soc* **118**, 12989-12996, (1996).

33 Higuchi, Y., Yagi, T. & Yasuoka, N. Unusual ligand structure in Ni-Fe active center and an additional Mg site in hydrogenase revealed by high resolution X-ray structure analysis. *Structure* **5**, 1671-1680, (1997).

34 Vignais, P. M. & Colbeau, A. Molecular biology of microbial hydrogenases. *Curr Issues Mol Biol* **6**, 159-188, (2004).

35 Tamagnini, P. *et al.* Hydrogenases and hydrogen metabolism of cyanobacteria. *Microbiol Mol Biol R* **66**, 1-+, (2002).

36 Appel, J. & Schulz, R. Hydrogen metabolism in organisms with oxygenic photosynthesis: hydrogenases as important regulatory devices for a proper redox poising? *J Photoch Photobio B* **47**, 1-11, (1998).

37 Fontecilla-Camps, J. C., Amara, P., Cavazza, C., Nicolet, Y. & Volbeda, A. Structure-function relationships of anaerobic gas-processing metalloenzymes. *Nature* **460**, 814-822, (2009).

38 Fontecilla-Camps, J. C., Volbeda, A., Cavazza, C. & Nicolet, Y. Structure/function relationships of [NiFe]- and [FeFe]-hydrogenases. *Chem Rev* **107**, 4273-4303, (2007).

39 Ogata, H., Lubitz, W. & Higuchi, Y. [NiFe] hydrogenases: structural and spectroscopic studies of the reaction mechanism. *Dalton T*, 7577-7587, (2009).

40 Armstrong, F. A. *et al.* Dynamic electrochemical investigations of hydrogen oxidation and production by enzymes and implications for future technology. *Chem Soc Rev* **38**, 36-51, (2009).

41 McIntosh, C. L., Germer, F., Schulz, R., Appel, J. & Jones, A. K. The [NiFe]-Hydrogenase of the Cyanobacterium Synechocystis sp PCC 6803 Works Bidirectionally with a Bias to H-2 Production. *J Am Chem Soc* **133**, 11308-11319, (2011).

42 Hexter, S. V., Grey, F., Happe, T., Climent, V. & Armstrong, F. A. Electrocatalytic mechanism of reversible hydrogen cycling by enzymes and distinctions between the major classes of hydrogenases (vol 109, pg 11516, 2012). *P Natl Acad Sci USA* **109**, 18232-18233, (2012).

43 Vincent, K. A., Parkin, A. & Armstrong, F. A. Investigating and exploiting the electrocatalytic properties of hydrogenases. *Chem Rev* **107**, 4366-4413, (2007).

44 Nicolet, Y., Piras, C., Legrand, P., Hatchikian, C. E. & Fontecilla-Camps, J. C. Desulfovibrio desulfuricans iron hydrogenase: the structure shows unusual coordination to an active site Fe binuclear center. *Struct Fold Des* **7**, 13-23, (1999).

45 Peters, J. W. X-ray crystal structure of the Fe-only hydrogenase (Cpl) from Clostridium pasteurianum to 1.8 angstrom resolution (vol 282, pg 1853, 1998). *Science* **283**, 35-35, (1999).

46 Albracht, S. P. J., Roseboom, W. & Hatchikian, E. C. The active site of the [FeFe]-hydrogenase from Desulfovibrio desulfuricans. 1. Light sensitivity and magnetic hyperfine interactions as observed by electron paramagnetic resonance. *J Biol Inorg Chem* **11**, 88-101, (2006).

47 Silakov, A., Kamp, C., Reijerse, E., Happe, T. & Lubitz, W. Spectroelectrochemical Characterization of the Active Site of the [FeFe] Hydrogenase HydA1 from Chlamydomonas reinhardtii. *Biochemistry-Us* **48**, 7780-7786, (2009).

48 Silakov, A., Wenk, B., Reijerse, E. & Lubitz, W. (14)N HYSCORE investigation of the H-cluster of [FeFe] hydrogenase: evidence for a nitrogen in the dithiol bridge. *Phys Chem Chem Phys* **11**, 6592-6599, (2009).

49 Nicolet, Y. *et al.* Crystallographic and FTIR spectroscopic evidence of changes in Fe coordination upon reduction of the active site of the Fe-only hydrogenase from Desulfovibrio desulfuricans. *J Am Chem Soc* **123**, 1596-1601, (2001).

50 VanderSpek, T. M. *et al.* Similarities in the architecture of the active sites of Ni-hydrogenases and Fe-hydrogenases detected by means of infrared spectroscopy. *Eur J Biochem* **237**, 629-634, (1996).

51 Lemon, B. J. & Peters, J. W. Binding of exogenously added carbon monoxide at the active site of the iron-only hydrogenase (CpI) from Clostridium pasteurianum. *Biochemistry-Us* **38**, 12969-12973, (1999).

52 Schut, G. J. & Adams, M. W. W. The Iron-Hydrogenase of Thermotoga maritima Utilizes Ferredoxin and NADH Synergistically: a New Perspective on Anaerobic Hydrogen Production. *J Bacteriol* **191**, 4451-4457, (2009).

53 Schuchmann, K. & Muller, V. A Bacterial Electron-bifurcating Hydrogenase. *J Biol Chem* **287**, 31165-31171, (2012).

54 Wang, S. N. *et al.* NADP-Specific Electron-Bifurcating [FeFe]-Hydrogenase in a Functional Complex with Formate Dehydrogenase in Clostridium autoethanogenum Grown on CO. *J Bacteriol* **195**, 4373-4386, (2013).

55 Krasna, A. I. & Rittenberg, D. The Mechanism of Action of the Enzyme Hydrogenase. *J Am Chem Soc* **76**, 3015-3020, (1954).

56 Pershad, H. R. *et al.* A voltammetric appraisal of rapid catalytic electron transport in Chromatium vinosum [NiFe]-hydrogenase. *J Inorg Biochem* **74**, 264-264, (1999).

57 Hoberman, H. D. & Rittenberg, D. Biological catalysis of the exchange reaction between water and hydrogen. *J Biol Chem* **147**, 211-227, (1943).

58 Tamiya, N. & Miller, S. L. Kinetic Studies on Hydrogenase. *J Biol Chem* **238**, 2194-&, (1963).

59 Anand, S. R. & Krasna, A. I. Catalysis of H2-Hto Exchange by Hydrogenase . A New Assay for Hydrogenase. *Biochemistry-Us* **4**, 2747-&, (1965).

60 Yagi, T., Tsuda, M. & Inokuchi, H. Kinetic Studies on Hydrogenase - Parahydrogen-Orthohydrogen Conversion and Hydrogen-Deuterium Exchange-Reactions. *J Biochem-Tokyo* **73**, 1069-1081, (1973).

61 Coremans, J. M., van Garderen, C. J. & Albracht, S. P. On the redox equilibrium between H2 and hydrogenase. *Biochim Biophys Acta* **1119**, 148-156, (1992).

62 Mctavish, H., Sayavedrasoto, L. A. & Arp, D. J. Substitution of Azotobacter-Vinelandii Hydrogenase Small-Subunit Cysteines by Serines Can Create Insensitivity to Inhibition by O-2 and Preferentially Damages H-2 Oxidation over H-2 Evolution. *J Bacteriol* **177**, 3960-3964, (1995).

63 McTavish, H., SayavedraSoto, L. A. & Arp, D. J. Comparison of isotope exchange, H-2 evolution, and H-2 oxidation activities of Azotobacter vinelandii hydrogenase. *BBA-Protein Struct M* **1294**, 183-190, (1996).

64 Zorin, N. A. *et al.* Inhibition by iodoacetamide and acetylene of the H-D-exchange reaction catalyzed by Thiocapsa roseopersicina hydrogenase. *Eur J Biochem* **241**, 675-681, (1996).

65 Bertrand, P., Dole, F., Asso, M. & Guigliarelli, B. Is there a rate-limiting step in the catalytic cycle of [Ni-Fe] hydrogenases? *J Biol Inorg Chem* **5**, 682-691, (2000).

66 Fisher, H. F., Krasna, A. I. & Rittenberg, D. The Interaction of Hydrogenase with Oxygen. *J Biol Chem* **209**, 569-578, (1954).

67 Gingras, G., Calvin, M. & Goldsby, R. A. Carbon Dioxide Metabolism in Hydrogen-Adapted Scenedesmus. *Arch Biochem Biophys* **100**, 178-&, (1963).

68 Abou Hamdan, A. *et al.* O-2-independent formation of the inactive states of NiFe hydrogenase. *Nat Chem Biol* **9**, 15-+, (2013).

69 Jones, A. K., Pershad, H. R., Sillery, E., Albracht, S. P. J. & Armstrong, F. A. Insights into the catalytic cycle of [NiFe]-hydrogenases from direct electrochemistry. *J Inorg Biochem* **86**, 283-283, (2001).

70 Vignais, P. M. *et al.* Continuous monitoring of the activation and activity of [NiFe]-hydrogenases by membrane-inlet mass spectrometry. *Int J Hydrogen Energ* **27**, 1441-1448, (2002).

71 Kurkin, S., George, S. J., Thorneley, R. N. F. & Albracht, S. P. J. Hydrogen-induced activation of the [NiFe]-hydrogenase from Allochromatium vinosum as studied by stopped-flow infrared spectroscopy. *Biochemistry-Us* **43**, 6820-6831, (2004).

72 Adams, M. W. W. The Structure and Mechanism of Iron-Hydrogenases. *Biochim Biophys Acta* **1020**, 115-145, (1990).

73 Peters, J. W. Structure and mechanism of iron-only hydrogenases. *Curr Opin Struc Biol* **9**, 670-676, (1999).

74 Cammack, R., Patil, D., Aguirre, R. & Hatchikian, E. C. Redox Properties of the Esr-Detectable Nickel in Hydrogenase from Desulfovibrio-Gigas. *FEBS Lett* **142**, 289-292, (1982).

75 Kruger, H. J. *et al.* Evidence for Nickel and a 3-Iron Center in the Hydrogenase of Desulfovibrio-Desulfuricans. *J Biol Chem* **257**, 4620-4623, (1982).

76 Legall, J. *et al.* The Presence of Redox-Sensitive Nickel in the Periplasmic Hydrogenase from Desulfovibrio Gigas. *Biochem Bioph Res Co* **106**, 610-616, (1982).

77 Moura, J. J. G. *et al.* Unambiguous Identification of the Nickel Electron-Paramagnetic-Res Signal in Ni-61-Enriched Desulfovibrio-Gigas Hydrogenase. *Biochem Bioph Res Co* **108**, 1388-1393, (1982).

78 Lubitz, W., Reijerse, E. & van Gastel, M. [NiFe] and [FeFe] hydrogenases studied by advanced magnetic resonance techniques. *Chem Rev* **107**, 4331-4365, (2007).

79 Teixeira, M. *et al.* Redox Properties and Activity Studies on a Nickel-Containing Hydrogenase Isolated from a Halophilic Sulfate Reducer Desulfovibrio-Salexigens. *Biochimie* **68**, 75-84, (1986).

80 Cammack, R., Patil, D. S., Hatchikian, E. C. & Fernandez, V. M. Nickel and Iron-Sulfur Centers in Desulfovibrio-Gigas Hydrogenase - Electron-Spin-Resonance Spectra, Redox Properties and Interactions. *Biochim Biophys Acta* **912**, 98-109, (1987).

81 Huynh, B. H. *et al.* On the Active-Sites of the [Nife] Hydrogenase from Desulfovibrio-Gigas - Mossbauer and Redox-Titration Studies. *J Biol Chem* **262**, 795-800, (1987).

82 Vanderzwaan, J. W., Albracht, S. P. J., Fontijn, R. D. & Slater, E. C. Mono-Valent Nickel in Hydrogenase from Chromatium-Vinosum - Light Sensitivity and Evidence for Direct Interaction with Hydrogen. *FEBS Lett* **179**, 271-277, (1985).

83 Brecht, M., van Gastel, M., Buhrke, T., Friedrich, B. & Lubitz, W. Direct detection of a hydrogen ligand in the [NiFe] center of the regulatory H-2-sensing hydrogenase from Ralstonia eutropha in its reduced state by HYSCORE and ENDOR spectroscopy. *J Am Chem Soc* **125**, 13075-13083, (2003).

84 Foerster, S., van Gastel, M., Brecht, M. & Lubitz, W. An orientation-selected ENDOR and HYSCORE study of the Ni-C active state of Desulfovibrio vulgaris Miyazaki F hydrogenase. *J Biol Inorg Chem* **10**, 51-62, (2005).

85 Fan, C. L. *et al.* Detection and Characterization of Exchangeable Protons Bound to the Hydrogen-Activation Nickel Site of Desulfovibrio-Gigas Hydrogenase - a H-1 and H-2 Q-Band Endor Study. *J Am Chem Soc* **113**, 20-24, (1991).

86 Bagley, K. A., Vangarderen, C., Albracht, S. P. J. & Woodruff, W. H. Infrared Studies on the Interaction of Carbon-Monoxide with Nickel in Hydrogenase. *Biophys J* **64**, A276-A276, (1993).

87 Bagley, K. A., Duin, E. C., Roseboom, W., Albracht, S. P. J. & Woodruff, W. H. Infrared-Detectable Groups Sense Changes in Charge-Density on the Nickel Center in Hydrogenase from Chromatium-Vinosum. *Biochemistry-Us* **34**, 5527-5535, (1995).

88 deLacey, A. L. *et al.* Infrared spectroelectrochemical characterization of the [NiFe] hydrogenase of Desulfovibrio gigas. *J Am Chem Soc* **119**, 7181-7189, (1997).

89 Fichtner, C., Laurich, C., Bothe, E. & Lubitz, W. Spectroelectrochemical characterization of the [NiFe] hydrogenase of Desulfovibrio vulgaris Miyazaki F. *Biochemistry-Us* **45**, 9706-9716, (2006).

90 De Lacey, A. L., Fernandez, V. M., Rousset, M. & Cammack, R. Activation and inactivation of hydrogenase function and the catalytic cycle: Spectroelectrochemical studies. *Chem Rev* **107**, 4304-4330, (2007).

91 Pandelia, M. E. *et al.* Membrane-Bound Hydrogenase I from the Hyperthermophilic Bacterium Aquifex aeolicus: Enzyme Activation, Redox Intermediates and Oxygen Tolerance. *J Am Chem Soc* **132**, 6991-7004, (2010).

92 Long, M. N. *et al.* Characterization of a HoxEFUYH type of [NiFe] hydrogenase from Allochromatium vinosum and some EPR and IR properties of the hydrogenase module. *J Biol Inorg Chem* **12**, 62-78, (2007).

93 DeLacey, A. L. *et al.* IR spectroelectrochemical study of the binding of carbon monoxide to the active site of Desulfovibrio fructosovorans Ni-Fe hydrogenase. *J Biol Inorg Chem* **7**, 318-326, (2002).

94 Saggu, M. *et al.* Spectroscopic Insights into the Oxygen-tolerant Membrane-associated [NiFe] Hydrogenase of Ralstonia eutropha H16. *J Biol Chem* **284**, 16264-16276, (2009).

95 Pierik, A. J., Schmelz, M., Lenz, O., Friedrich, B. & Albracht, S. P. J. Characterization of the active site of a hydrogen sensor from Alcaligenes eutrophus. *FEBS Lett* **438**, 231-235, (1998).

96 Horch, M. *et al.* Probing the active site of an O2-tolerant NAD+-reducing [NiFe]-hydrogenase from Ralstonia eutropha H16 by in situ EPR and FTIR spectroscopy. *Angew Chem Int Ed* **49**, 8026-8029, (2010).

97 Germer, F. *et al.* Overexpression, Isolation, and Spectroscopic Characterization of the Bidirectional [NiFe] Hydrogenase from Synechocystis sp PCC 6803. *J Biol Chem* **284**, 36462-36472, (2009).

98 Armstrong, F. A., Heering, H. A. & Hirst, J. Reactions of complex metalloproteins studied by protein-film voltammetry. *Chem Soc Rev* **26**, 169-179, (1997).

99 Happe, R. P., Roseboom, W. & Albracht, S. P. J. Pre-steady-state kinetics of the reactions of [NiFe]-hydrogenase from Chromatium vinosum with H-2 and CO. *Eur J Biochem* **259**, 602-608, (1999).

100 George, S. J., Kurkin, S., Thorneley, R. N. F. & Albracht, S. P. J. Reactions of H-2, CO, and O-2 with active [NiFe]-Hydrogenase from Allochromatium vinosum. A stopped-flow infrared study. *Biochemistry-Us* **43**, 6808-6819, (2004).

101 Pandelia, M. E., Ogata, H. & Lubitz, W. Intermediates in the Catalytic Cycle of [NiFe] Hydrogenase: Functional Spectroscopy of the Active Site. *Chemphyschem* **11**, 1127-1140, (2010).

102 Fritsch, J., Lenz, O. & Friedrich, B. Structure, function and biosynthesis of O(2)-tolerant hydrogenases. *Nat Rev Microbiol* **11**, 106-114, (2013).

103 Shafaat, H. S., Rudiger, O., Ogata, H. & Lubitz, W. [NiFe] hydrogenases: A common active site for hydrogen metabolism under diverse conditions. *BBA-Bioenergetics* **1827**, 986-1002, (2013).

104 Lubitz, W. [NiFe] and [Fe Fe] hydrogenases: Active site structures and catalytic mechanisms. *J Biol Inorg Chem* **19**, S99-S99, (2014).

105 Lubitz, W., Ogata, H., Rudiger, O. & Reijerse, E. Hydrogenases. *Chem Rev* **114**, 4081-4148, (2014).

106 Huynh, B. H. *et al.* Desulfovibrio-Vulgaris Hydrogenase - a Nonheme Iron Enzyme Lacking Nickel That Exhibits Anomalous Electron-Paramagnetic-Res and Mossbauer-Spectra. *P Natl Acad Sci-Biol* **81**, 3728-3732, (1984).

107 Adams, M. W. W. & Mortenson, L. E. The Purification of Hydrogenase-Ii (Uptake Hydrogenase) from the Anaerobic N-2-Fixing Bacterium Clostridium-Pasteurianum. *Biochim Biophys Acta* **766**, 51-61, (1984).

108 Adams, M. W. W. & Mortenson, L. E. The Physical and Catalytic Properties of Hydrogenase-Ii of Clostridium Pasteurianum - a Comparison with Hydrogenase-I. *J Biol Chem* **259**, 7045-7055, (1984).

109 Wang, G. *et al.* Mossbauer and Electron Nuclear Double-Resonance Study of Oxidized Bidirectional Hydrogenase from Clostridium-Pasteurianum W5. *J Biol Chem* **259**, 4328-4331, (1984).

110 Pierik, A. J., Hulstein, M., Hagen, W. R. & Albracht, S. P. J. A low-spin iron with CN and CO as intrinsic ligands forms the core of the active site in [Fe]-hydrogenases. *Eur J Biochem* **258**, 572-578, (1998).

111 De Lacey, A. L., Stadler, C., Cavazza, C., Hatchikian, E. C. & Fernandez, V. M. FTIR characterization of the active site of the Fe-hydrogenase from Desulfovibrio desulfuricans. *J Am Chem Soc* **122**, 11232-11233, (2000).

112 Mulder, D. W. *et al.* EPR and FTIR analysis of the mechanism of H2 activation by [FeFe]-hydrogenase HydA1 from Chlamydomonas reinhardtii. *J Am Chem Soc* **135**, 6921-6929, (2013).

113 Mulder, D. W. *et al.* Investigations on the Role of Proton-Coupled Electron Transfer in Hydrogen Activation by [FeFe]-Hydrogenase. *J Am Chem Soc* **136**, 15394-15402, (2014).

114 Stripp, S., Sanganas, O., Happe, T. & Haumann, M. The structure of the active site H-cluster of [FeFe] hydrogenase from the green alga Chlamydomonas reinhardtii studied by X-ray absorption spectroscopy. *Biochemistry-Us* **48**, 5042-5049, (2009).

115 Roseboom, W., De Lacey, A. L., Fernandez, V. M., Hatchikian, E. C. & Albracht, S. P. J. The active site of the [FeFe]-hydrogenase from Desulfovibrio desulfuricans. II. Redox properties, light sensitivity and CO-ligand exchange as observed by infrared spectroscopy. *J Biol Inorg Chem* **11**, 102-118, (2006).

116 Adamska, A. *et al.* Identification and characterization of the "super-reduced" state of the H-cluster in [FeFe] hydrogenase: a new building block for the catalytic cycle? *Angew Chem Int Ed* **51**, 11458-11462, (2012).

117 Adamska-Venkatesh, A. *et al.* New redox states observed in [FeFe] hydrogenases reveal redox coupling within the H-cluster. *J Am Chem Soc* **136**, 11339-11346, (2014).

118 Vincent, K. A. *et al.* Electrochemical definitions of O-2 sensitivity and oxidative inactivation in hydrogenases. *J Am Chem Soc* **127**, 18179-18189, (2005).

119 Vignais, P. M. H/D exchange reactions and mechanistic aspects of the hydrogenases. *Coordin Chem Rev* **249**, 1677-1690, (2005).

120 Armstrong, F. A. & Albracht, P. J. [NiFe]-hydrogenases: spectroscopic and electrochemical definition of reactions and intermediates. *Philos T Roy Soc A* **363**, 937-954, (2005).

121 Laidler, K. J. *Chemical Kinetics*. Third edn, (Harper & Row, Publishers, Inc., 1987).

122 Orii, Y. Immediate Reduction of Cytochrome-C by Photoexcited Nadh - Reaction-Mechanism as Revealed by Flow Flash and Rapid-Scan Studies. *Biochemistry-Us* **32**, 11910-11914, (1993).

123 Winkler, J. R. & Gray, H. B. Electron Flow through Metalloproteins. *Chem Rev* **114**, 3369-3380, (2014).

124 Donten, M. L. *et al.* pH-Jump Induced Leucine Zipper Folding beyond the Diffusion Limit. *J Phys Chem B* **119**, 1425-1432, (2015).

Chapter 2

Materials and Methods

2.1 – Introduction

This chapter describes a multitude of experimental methods used for examining steady state and pre steady state kinetics as well as spectroscopic features of hydrogenases and the chemical tools used for photo-initiation. Due to the significant experimental challenge of measuring structure specific kinetic processes from nanoseconds to seconds, numerous analytical techniques were required to develop and apply this methodology. This chapter is divided into four sections concerning enzyme expression and purification, non-enzymatic materials used, analytical methods and finally enzyme assays. Enzyme expression and purification was performed by Dr. Crisjoe A. Joseph working in Prof. Michael Maroney's lab at University of Massachusetts at Amherst (*Thiocapsa roseopersicina*), Chang-Hao "Perry" Wu and Dr. Gerti Schut working in Prof. Michael W. W. Adams lab at the University of Georgia (*Pyrococcus furiosus* and *Thermotoga maritima* respectively), enzymes which are used throughout this thesis. Additional chemicals were used as received from standard commercial sources and quantum dots were synthesized according to established literature procedures which are primarily explored in Chapter 4. UV-Vis, FTIR, Raman, gas chromatography and fluorescence as well as time resolved applications of visible, infrared and fluorescence spectroscopy were used extensively throughout this thesis. Finally methods for experimentally determining enzyme rate constants and kinetic parameters are detailed which are used in Chapter 3.

2.2 - Enzyme purification

2.2.1 - Expression and purification of *Thiocapsa roseopersicina* membrane bound hydrogenase

- Expression and purification of *Thiocapsa roseopersicina* membrane bound hydrogenase was performed by Dr. Crisjoe A. Joseph at University of Massachusetts Amherst according to the procedure detailed below. Cultures of *Thiocapsa roseopersicina*, a photosynthetic, purple sulfur bacterium, were grown from stabs generously donated by Dr. I. N. Gogotov (Institute of Soil Sciences – Puchino, Russia) and Dr. Kornel Kovacs (Biological Research Institute, Hungarian Academy of Sciences – Szeged, Hungary). The stabs were used to inoculate 10 mL sealed, autoclaved vials which contained modified Pfennig's media. These vials were flushed with a carbon dioxide:nitrogen (1:4) mixture and illuminated with incandescent light at 25 ˚C. During the late logarithmic phase of growth (2 – 4 weeks), the vials were used to inoculate a larger container of modified Pfennig's media (such that the inoculum makes up 20% of the total batch culture). This process was repeated, increasing the container size each step until the cultures were grown in 10 L carboys from which the cells are harvested. The harvest process included a combination of microfiltration (using a self-constructed apparatus utilizing a hollow fiber cartridge) and centrifugation.

Purification of the hydrogenase enzyme used a procedure described below. In 350 g batches (harvested from 120 L), the cell paste was converted to an acetone powder by suspending it in 2 L of acetone (previously chilled to -30 ˚C), and then allowed to stir for 1 h at 4 ˚C. This process was used to lyse the cells and dissolve the cellular membrane, leaving the hydrogenase intact. The suspension was filtered through a coarse frit and the

filter cake was then resuspended in 90% acetone and stirred for another hour. This process was continued until the filtrate is no longer dark purple (about 9-12 washes), the final wash used 100% acetone. The wet powder was dried over P_4O_{10} in a desiccator under vacuum. The resulting sand colored powder (yield = 60 g) was then stored at -20 oC. In 15g batches the acetone powder was dissolved in warm (50 ˚C) nano-pure water. It is allowed to stir for 1-2 h after which it is centrifuged. The supernatant is poured off and 100 mL of DEAE-DE52 is added to the supernatant. This mixture is agitated by gentle shaking for 2 h. The DEAE mixture is filtered and the resin is resuspended in 1 L of a salt solution (450 mM NaCl, 20 mM TRIS, pH = 7.5). Again the mixture is agitated by gentle shaking for 2 h and the solution in filtered. To the filtrate, 100 g of $(NH)_2SO_4$ is added along with 50 mL of butyl sepharose resin. This mixture is agitated by gentle shaking for 2 h and packed into an FPLC column. The column is subject to the following chromatographic procedure and the fractions were assayed for hydrogenase activity by GC. Butyl Sepharose Chromotography (1 mM TRIS, pH =7.5): 200 mL at a constant 4% $(NH)_2SO_4$ then 150 mL gradient to 0% $(NH)_2SO_4$ then 250 mL at a constant 0% $(NH)_2SO_4$. Hydrogenase activity is found all throughout the latter half of the program. The most active fractions appear when the 0% $(NH)_2SO_4$ starts. These are pooled and concentrated. This pool is loaded onto a Q-sepharose column and subject to the following elution program. Q-Sepharose Chromotography (20 mM TRIS, pH =7.5): constant 0 mM NaCl for 2 column volumes then constant 250 mM NaCl for 2 column volumes then constant 600 mM NaCl for 8 column volumes with a final step at constant 1 M NaCl for 2 column volumes. Hydrogenase activity is found in the first half of the 600 mM NaCl fractions. These fractions are pooled and buffered exchanged into a MES buffer system at

lower pH. It is then loaded into another Q-sepharose column and subject to the following elution program. Once again the fractions are assayed for hydrogenase activity. Q-Sepharose Chromotography (50 mM MES, pH =5.5): gradient to 200 mM NaCl over 2 column volumes then constant 200 mM NaCl for 2 column volumes then gradient to 450 mM NaCl over for 4 column volumes then constant 600 mM NaCl for 2 column volumes then gradient to 1 M NaCl over 1 column volume and finally a constant 1 M NaCl for 1 column volume. Hydrogenase activity is found in the gradient to 450 mM NaCl fractions. The active fractions are pooled. Native prep-PAGE: The final purification was achieved using a 9% native preparative polyacrylamide gel. The hydrogenase band was excised and separated from gel particulates using a short Q-Sepharose column.

2.2.2 – Expression and purification of the soluble H_2ase 1 (SHI) from *Pyrococcus furiosus* (*Pf*)– The purification of the 9-His tagged SHI of *Pf* was performed as described by Chandrayan *et al*. and was performed by Chang-Ho "Perry" Wu at the University of Georgia.[1] His tag variants were expressed and purified identically. Briefly, a knock in cassette was constructed for the 9x-His tag by a four fragment addition to the plasmid including an upstream flanking region, a marker cassette (P_{gdh}-pyrF), an S-layer protein promoter including the 9x-His tag and a downstream flanking region by overlapping PCR, placed at the N-terminus of the β subunit. Cells were grown in rich media with maltose as the carbon source in 20 L fermenters at 90 ˚C under N_2/CO_2 for 14 hours. Cells were harvested and lysed by anaerobic stirring with 50 μg/mL DNase in TRIS buffer for 4 hours. Ultracentrifugation was used to separate the cell membrane and the supernatant was purified by Ni-NTA affinity chromatography.

2.2.3 – Expression and purification of the electron bifurcating [FeFe] H_2ase from *Thermotoga maritima* (*Tm*) – The expression and purification of the native [FeFe] H_2ase from *Tm* was performed as described by Schut and Verhagen *et al.* and was performed by Gerti Schut at the Unviersity of Georgia.[2,3] Briefly, Tm was grown in 500 L cultures at 80 ˚C with 0.4% (wt/vol) maltose in rich medium. Cells were lysed anaerobically by osmotic shock in 200 mL 50 mM Tris-HCl, pH 8.0, containing DNase (2.5 mg) and sodium dithionite (1 mM). The cell-free extract of 400 g (wet weight) of cells was loaded onto a DEAE Sepharose FF column (10x20cm) and the hydrogenase was eluted at 30 ml min in a linear gradient of 15 L from 0 to 0.5 M NaCl in 20 mM Tris-HCl, pH 8.0. The pooled hydrogenase fractions were loaded onto a Q-Sepharose HP column (3.5x10 cm) equilibrated with 20 mM Tris- HCl, pH 8.0. Adsorbed proteins were eluted at 4 ml/min with a linear gradient (1 L) from 0 to 0.5 M NaCl in 20 mM Tris-HCl, pH 8.0. The hydrogenase containing fractions were diluted with two volumes of equilibration buffer and loaded onto a hydroxyapatite column (5.0x12 cm) equilibrated in 20 mM Tris-HCl, pH 8.0. The column was developed at 4 ml/min with a linear gradient (2 L) from 0 to 200 mM potassium phosphate in 20 mM Tris-HCl. The hydrogenase-containing fractions were concentrated using a HiTrap Q column (5 ml) equilibrated with 20 mM Tris-HCl, pH 8.0, at 4 ml/min and eluted with 0.5 M NaCl in Tris-HCl, pH 8.0. The concentrated fraction was loaded onto a Superdex S-200 gel filtration column (6.0x60 cm) equilibrated in 20 mM HEPES, pH 7.0, containing 150 mM NaCl at 5 ml/min (3L). Ammonium sulfate (to 1.0 M) was added to the hydrogenase-containing fractions and these were loaded onto a column (3.5x10 cm) of Phenyl Sepharose equilibrated with 20 mM Tris-

HCl, pH 8.0, containing 1 M $(NH_4)_2SO_4$ and 10% glycerol at 5 ml/min. The protein was eluted with a linear gradient (1 L) from 1 to 0 M $(NH_4)_2SO_4$. Fractions containing hydrogenase were pooled, loaded on a small Phenyl
Sepharose column (1.6x5 cm) equilibrated with 1 M $(NH_4)_2SO_4$ and 10% glycerol at 4 ml/min, and the enzyme was eluted with 20 mM Tris-HCl containing 10% glycerol at 2 ml/min. The concentrated enzyme was applied to a Superdex S-200 column (6.0x60 cm) equilibrated with 20 mM Tris-HCl, pH 8.0, containing 150 mM NaCl at 5 ml/min.

2.3 – Materials

All reagents were commercial grade and used without further purification.

2.3.1 – Buffers – All buffers reported herein were prepared using monobasic and dibasic potassium phosphate of analytical grade (J. T. Baker) and pH adjusted using 6M NaOH and 6M HCl and a calibrated pH meter (Mettler Toledo). Salt additions were determined to be less than 10% of the buffer concentration based on initial pH. Deuterated buffers were prepared identically, with two additional steps of freeze dry exchange into pure D_2O (99.9%, Cambridge Isotope Labs).

2.3.2 – Nanocrystal synthesis

2.3.2.1 – CdTe quantum dots - CdTe quantum dots of ~3 nm diameter were grown by procedures based on the method of Hao *et al.* and was scaled according to demand.[4] Briefly, 44 mg (340 µmol) Tellurium powder (Strem 99.999%) and 65 mg (1.8 mmol)

$NaBH_4$ (Sigma 98%) were disolved in 2mL DI water under argon for 8 hrs to form a dark purple NaHTe solution. 124 mg (680 µmol) of $CdCl_2$ (Aldrich 99.5%) was dissolved in 150mL DI water and 108 uL (1.2 mmol) mercaptopropionic acid (MPA) was added and pH adjusted to ~11 by KOH. The Cd^{2+} solution was degased and brought to reflux then NaHTe solution was added. The solution quickly turned bright orange and a band edge appeared at between 490-495 nm. Band edges at 530 nm were achieved by growth for ~6 hrs and monitored by UV-Vis. Once the dots were of the appropriate size, the reaction was quenched by cooling then the dots were precipitated by acetone and collected by centrifugation. This process was repeated to wash away any remaining soluble reagents. Dots were then re-suspended in DI H_2O and stored in the dark at RT. These dots retained their luminescence for months by this method.

2.3.2.2 – CdSe@CdS quantum dot in rods – CdSe@CdS quantum dot in rods were synthesized by Bryant Chica at Emory University based on established procedures.[5] The nanocrystals were characterized by TEM to confirm their nanostructure and were 4 nm x 30 nm. The dot in rod nanoparticles were ligand exchanged to solubilize them in aqueous solution as follows: CdSe/CdS core/shell QD's were precipitated from the crude reaction mixture with 1-propanol and methanol and then spun down in a centrifuge at 5000xg for 5 minutes. The QD's were then resuspended in minimal chloroform and precipitated with addition of methanol. This was repeated twice and then the QD's were resuspended in chloroform. The ligand exchange solution was prepared by adding 200 mg of glutathione to 4 mL of 3:1 MeOH:H_2O. The glutathione was then dissolved in this solution by adjusting the pH to ~11 to deprotonate the ligand and generate the reactive thiolate form

with high affinity for the nanocrystal surface. 200 uL of the QD's in chloroform and 1 mL of the glutathione solution were combined in a vial and then vortexed for 2 minutes. The aqueous and organic phases were allowed to separate and borate buffer (pH 8) and chloroform (750 uL) were added to increase the volume of the respective phases. The mixture was shaken and the phases allowed to separate. The organic phase was removed and the aqueous phase was 2x extracted with chloroform to remove any residual hydrophobic ligand. The resulting glutathione capped nanocrystals were purified using 30 kDa Centricon molecular weight cutoff filters to remove excess glutathione or else stored in the crude exchange solution. All QD samples were stored in the dark under argon at 3^0C.

2.3.3 Miscellaneous Chemicals – Ultrahigh purity H_2, N_2, CO and 5% H_2 in N_2 were purchased from Lindt Gas Solutions LLC. 99.8% D_2 (Raman standard and H/D exchange assay) was purchased from Sigma Aldrich. 98% HD gas (Raman standard) was purchased from Sigma Aldrich. β-nicotinamide adenine dinucleotide (NADH) (98%), Tris(bipyridine) ruthenium(II) dichloride (98%), methyl viologen dichloride (MV, 99.9%) and 98% sodium dithionite ($Na_2S_2O_4$) were purchased from Sigma Aldrich.

2.4 – Analytical Methods

2.4.1 – UV-Vis absorption – Routine UV-Vis absorption characterizations were carried out using a Lambda 35 UV-Vis spectrophotometer (Perkin Elmer) in dual beam configuration with 1 nm slit width and 1 nm scan steps. UV-Vis of samples used in

transient measurements was performed on a home-built spectrometer described briefly herein. An attenuated fiber coupled 30 W HgXe lamp (Ocean Optics Inc.) was subsequently collimated and passed through the sample in single beam geometry. The transmitted beam was focused into another fiber optic which directed the transmitted light onto a CCD based spectrophotometer (Ocean Optics QE65000). Typical integration times were 10 ms and 100 scans were averaged. The single beam spectrum of the CaF_2 cell with H_2O was determined and used as a reference. Temperature dependent UV-Vis was carried out using a Carry 35 spectrophotometer (Agilent Technologies Inc.) in dual beam configuration with 1 nm slit width and resolution.

2.4.2 – FTIR – Routine FTIR and temperature dependent FTIR were measured using a modified Varian Excalibur FTIR spectrometer in an external beam configuration. The external beam was focused at the sample by a F/2 off axis 90˚ gold parabolic mirror and subsequently recollimated by another F/2 90˚ off axis parabolic mirror then focused onto a 1mm liquid nitrogen cooled MCT detector by a final F/1 90˚ off axis parabolic mirror. The sample temperature was controlled by a recirculating temperature controlled water bath, and the sample was rastered (for sample and reference measurements) by a computer controlled electronic stage. Typical measurements employed 2 cm^{-1} spectral and optical resolution, with 20 kHz modulation frequency, under-sampling ratio of 2, and a frequency filter of 10 kHz. Triangular apodization functions were used to compute the Fourier transform and Fourier transformed data was ratioed against an appropriate reference for absorbance measurements. Light titration difference FTIR measurements

were performed on a Biorad FTS 6000 step-scan FTIR spectrometer in an external beam configuration analogous to the external configuration of the Excalibur system. Spectra were collected by excitation of the sample from the second harmonic (527 nm) of an actively Q-switched Nd:YLF laser (Crystalaser Inc.) at a repetition rate of 4 kHz and a power of 125 mW focused to a 1 mm spot. Exposure times were controlled by a computer controlled optical shutter. CaF_2 windows were used throughout and PTFE spacers were used of various thickness from 75-125 μm housed in copper cells for thermal conductivity.

2.4.3 – Gas Chromatography - The GC measurements were performed on an Agilent 7890A gas chromatography instrument equipped with a pulse discharge detector (Valco Instruments) and a 30 m long 50 μm thick molecular sieve column (HP PLOT-Molsieve, Agilent Technologies Inc.) with an oven temperature of 100˚C, inlet at 150 ˚C and detector at 120 ˚C with an inlet pressure of 8 psi and a split ratio of 100:1. The peak position and amplitude were calibrated by performing controlled injections of H_2 into the experimental cell used for measurements under identical volume ratios of gas to liquid (2.25 mL total volume, 1.25 mL solution, 1 mL headspace). 10 μL of sample headspace (1%) were sampled at each time-point, the most air exposed 5μL were discarded and the remaining 5 μL were injected to the GC. Under these conditions H_2 eluted off the column at 1.71 minutes, whereas O_2 eluted at 2.02 minutes and N_2 at 2.31 minutes. Using the known density of H_2 at NTP (0.089 g/L), the injected volume and the atmospheric pressure the integrated peak area was converted to nanomoles of H_2 in the cell using the determined calibration curve. This was repeated with D_2 gas (for KIE measurements) and

determined to be identical. A representative calibration standard is shown below in Figure 2.1.

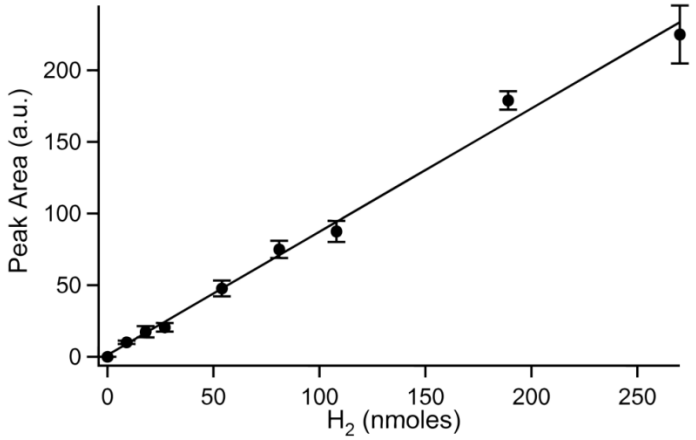

Figure 2.1 - GC calibration for the quantification of $H_2(D_2)$ using the pulsed discharge detector. Error bars represent the standard deviation of three independent measurements.

2.4.4 – Photoluminescence – Photoluminescence titration data for CdTe quantum dots were recorded on an Ocean Optics QE65000 CCD spectrophotometer using a 35W Xe lamp (Ocean Optics) and a computer controlled monochromotor (Ocean Optics) to select an excitation wavelength of 500 nm. Photoluminescence was collected orthogonal to the excitation beam. 1mL samples of 500 nM MPA capped QDs (concentration determined by the method of Peng et al. and used throughout) in 100 mM phosphate buffer pH = 7.0 were prepared anaerobically in a 5% H_2 atmosphere in Ar in an anaerobic box (COY Labs.) Separately a 50 µL solution of 80 µM H_2ase in 100 mM phosphate buffer pH = 7 activated under 5% H_2 in argon was prepared and loaded into a gas tight syringe. Titrations with CdTe quantum dots were collected by titration of a 100 µM H_2ase stock into a solution of 1.5 µM CdTe quantum dots in 0.4 µM steps of H_2ase (10 µL) to a final

concentration of 4 μM. Photoluminescence titrations with CdTe quantum dots were collected by titration of a 100 μM H_2ase stock into a solution of 1.5 μM CdTe quantum dots in 0.4 μM steps of H_2ase (10 μL) to a final concentration of 4 μM. For Ru(bpy) photoluminescence titrations of concentrated solutions of H_2ase into 10 μM Ru(bpy) to a final concentration of 20 μM H_2ase in steps of 2 μM H_2ase. A 1.4 mL quartz micro fluorescence cell (Starna Inc.) was loaded with the QD solution, sealed with a septum. Titrations were performed by injecting 5μL of the concentrated H_2ase solution then allowed to equilibrate for 20 minutes. Absorbance measurements were performed on a Perkin Elmer Lambda 35 UV-Vis spectrometer. After an absorbance measurement a blank photoluminescence spectra was collected using a rhodamine G6 (R6G) polymer block (Starna Inc) exciting at 500 nm to correct for lamp and spectrometer drift. Sample photoluminescence spectra were then collected integrating for 2 minutes averaging 5 scans. A dark scan was collected to subtract out the baseline signal. Absorbance at 500 nm was ~0.04 OD and dilution effects were corrected by controlled injections of pure buffer. The PL was then integrated from 510 nm – 800nm and normalized. Quantum yield measurements were determined twice by $Ru(bpy)_3$ in deaerated buffer (4% QY) and R6G in ethanol (95% QY) by the equation

$$\Phi_x = \Phi_{ST} \cdot \frac{A_x}{A_{ST}} \cdot \left(\frac{\eta_x}{\eta_{ST}}\right)^2$$

where Φ_x is the QY of the unknown, Φ_{st} is the QY of the standard, A is the absorbance and η is the index of refraction of the solvent used for the measurements. Absorbances were all below 0.1 to eliminate non-linear absorbance vs. photoluminescence gradients.

2.4.5 – Time Resolved Photoluminescence - Time resolved photoluminescence measurements were carried out on a home built instrument described below. The second harmonic from a Q-switched Nd:YAG laser (10 Hz, 10 μJ/pulse, Quanta Ray Inc.) was used to excite samples of $Ru(bpy)_3^{2+}$ and was focused to ~4 mm diameter at the sample location. Scattered excitation light was used to trigger data collection. Sample photoluminescence was collected by a 4" F/1 quartz lens and focused onto a PMT by another 4" F/1 lens. CCD output was digitized by a LeCroy Wavesurfer oscilloscope (Teledyne Inc.), inverted and normalized.

2.4.6 – Tandem Transient Infrared/Visible Absorbance - A schematic of the instrumental design is shown in Fig. 2.2. Photolysis was achieved by a Q-switched Nd:YAG laser (Continuum Inc.) with a repetition rate of 10 Hz. An LBO crystal was used to generate the double and triple harmonics at 532 and 355 nm respectively. The 355 nm line was separated by a series of prisms in the harmonic separator. The subsequent 355 nm light was filtered of any residual 532 and 1064 by a 355 nm dielectric mirror and passed onto a stable top beam shaper (Laseroptiks Inc) which flattened the Gaussian profile of the beam minimizing drift of pump energy over the pump volume. Pump pulses were "picked" by triggering of an optical shutter (Thor Labs Inc) opening for 95% of the pulse to pulse repetition rate eliminating possible double excitation. The picked pulses were focused at the sample to a 200 μm diameter spot by a long focal length fused silica lens as measured by a knife edge. A back reflection was used to trigger the data collection by a photo-diode detector (Thor Labs Inc). The sample was probed by two monochromatic laser beams from a tunable cw quantum cascade laser (QCL, Daylight

Solutions LLC) and a compact 635 nm laser diode (Thor Labs Inc). The two beams were brought collinear by germanium windows which transmitted the mid infrared light and reflected the 635 nm visible light. The QCL was optically isolated by a series of linear polarizers oriented perpendicular to each other and an off axis germanium window. The 635 nm beam was cross polarized to the pump beam allowing for discrimination of the pump pulse at the photo-diode detector by a polarizer and filtered by a 420 nm long pass filter to reject NADH fluorescence.

The infrared and visible beams were focused to 80 and 100 μm diameter spots respectively by a CaF_2 lens as measured by a knife edge to ensure even pump illumination. The IR probe beam was focused onto a 1 mm (50 MHz) MCT detector (Kolmar Inc.) The visible probe was focused onto a 13 mm^2 fast rise time (125 MHz) silicon photo-diode detector (Thor Labs Inc.). The raw signal from trigger, 635 nm diode and MCT were passed to a 16 bit 65 MHz analog bandwidth digitizer (Gage Applied Technologies Inc.) operating at 10 MHz digital resolution and the data was subsequently logarithmically binned in time decreasing the data points from 10^6 to 10^4. The raw signal intensities (I_0) were determined by an optical chopper and DC offset to 0 V, thus the ΔA was calculated by $\Delta A = -\log(I_{data} + I_0/I_0)$ and the infrared transients were corrected for thermal response of the solvent by subtraction of the scaled (10-20% in most cases) reference heating signature which resolved baselines below 100 μOD with noise levels of 30 μOD for 50 shot averages.

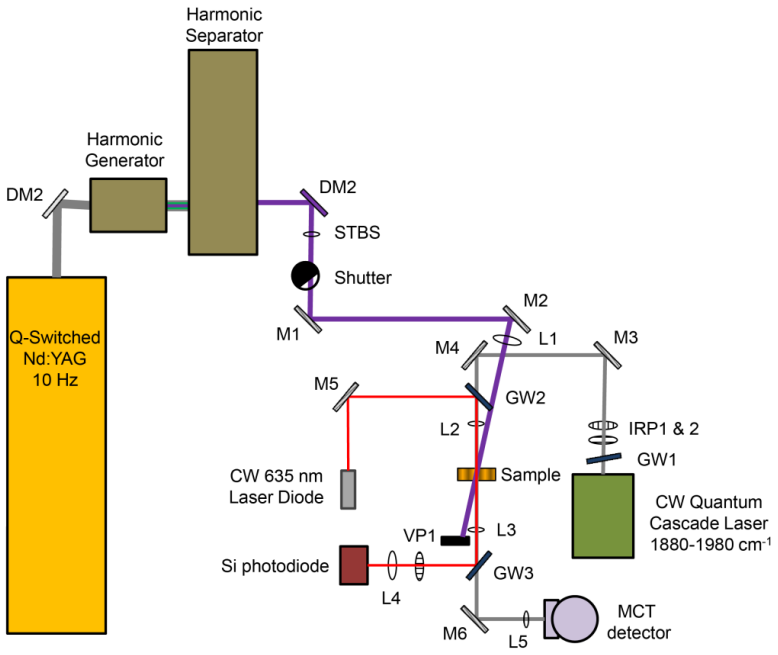

Figure 2.2 - Simultaneous transient infrared and visible absorbance apparatus. Optics labels are as follows: DM# = dielectric mirror, STBS = stable top beam shaper, M# = mirror, L# = Lens (L2, L3 and L5 are CaF_2, L1 and L4 are fused silica), IRP# = CaF_2 IR wire grid polarizer, VP# = Visible polarizer, GW# = germanium window.

Samples for transient experiments were prepared as follows. Solutions of 2 mg of active H_2ase were exchanged into 10 mM MV^{2+} and 50 mM phosphate with pH(D)s of 6.3, 7.0 and 7.7 by 50 kDa molecular weight cutoff centrifugal filters (Millipore) under an H_2 free atmosphere until no further H_2 induced MV^{2+} reduction was observed. This protocol prepared the various enzyme samples in similar equilibrium state distributions and under slightly oxidized conditions amenable to photo-reduction. The MV^{2+} exchanged H_2ase samples were then exchanged similarly into 12 mM NADH, 10 mM MV^{2+} and 50 mM phosphate at the appropriate pH(D) and concentrated to a final volume of 10-15 µL resulting in a final concentration of 1.5 mM H_2ase based on a molecular

weight of 153,000 Da. The concentrated sample was loaded into one half of a split infrared transmission cell employing CaF_2 windows sandwiching a dividing Teflon spacer (pathlength = 75 μm) and sealed. The reference was prepared similarly except for the use of reduced horse heart myoglobin (deoxyMb) at a concentration of 2 mM Mb which matched the optical density at 355 nm.

2.4.7 – Raman Detection of HD – For D_2/H^+ exchange, Raman scattering of the gas headspace was used to quantify HD (3420 cm^{-1}) production by 527 nm excitation with a Nd:YLF laser operating at 3 kHz and 200 mW of incident power. The scattering was collected and dispersed using a transmissive grating spectrograph (Kaiser) and the spectrum was imaged on a CCD (Princeton instruments) with an integration time of 10 s binning 40 time points with a final time resolution of ~7 minutes. Calibrations were performed for scattering non-linearity and offset by reference samples of H_2, HD and D_2 (4160, 3632 and 2989 cm^{-1} respectively, Fig. 2.3)

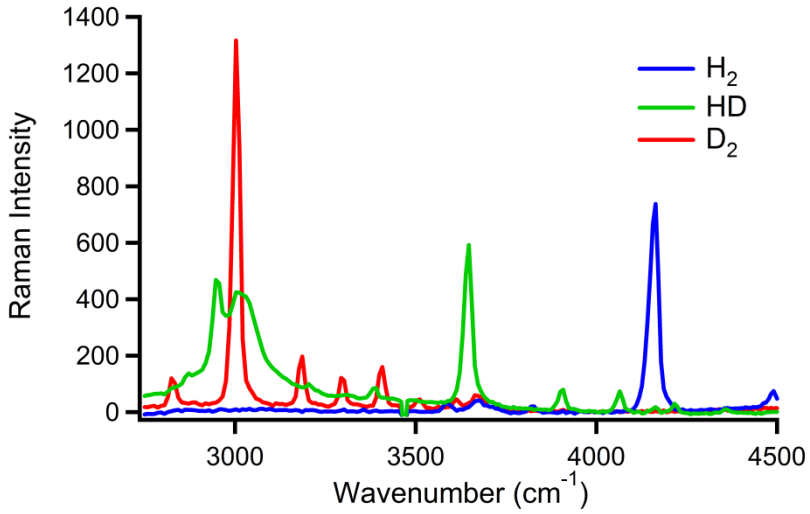

Figure 2.3 – Raman spectra of gas phase H_2, HD and D_2.

2.5 – Enzyme Assays

2.5.1 – H_2 Production - H_2ase steady state kinetics samples (5-100 nM) were prepared anaerobicaly in buffers (50 mM PO_4 at appropriate pH(D)) containing 5% H_2 in an N_2 atmosphere. After preparation the samples were flushed with pure N_2 for 15 minutes under vigorous stirring. Samples were subsequently allowed to equilibrate for another 10 minutes after which the headspace was analyzed to confirm the removal of H_2. Next a concentrated stock solution of methyl viologen (MV) and $Na_2S_2O_4$ was injected to a final concentration of 1-10 mM MV and 2-20 mM $Na_2S_2O_4$ respectively, initiating the timing of the kinetics experiment. Samples of the headspace were measured every 5 minutes by gas chromatography (section 2.3.3) and experiments were repeated at least three times with error reported as the standard deviation of the measurements at each time point.

Photo-catalytic initiation was carried out as follows. For Ru(bpy) photoionization, 1μM *Tr* H_2ase was mixed with 500 μM $Ru(bpy)_3^{2+}$ and 100 mM Ascorbate in 100 mM

phosphate buffer pH = 7.4. Samples were prepared anaerobically and exchanged with nitrogen to eliminate residual H_2. Photoexcitation was achieved by a the second harmonic (527 nm) of a Nd:YLF laser operating at 3 kHz and 150 mW of incident power with a beam diameter of 1 cm. Similarly, for CdTe quantum dot sensitization 1μM *Tr* H_2ase was mixed with 0.5 μM $Ru(bpy)_3^{2+}$ and 100 mM Ascorbate in 100 mM phosphate buffer pH = 7.4 under identical excitation conditions. For NADH photolysis, , 200 μM NADH, 10 mM MV^{2+} and 20 nM H_2ase were mixed in 50 mM PO_4 buffer pH 7.0. The sample was illuminated by a 351 nm Nd:YLF laser (Crystalaser Inc.) at 50 mW incident power, a repetition rate of 2 kHz and focused to 500 μm diameter spot through the 1 cm path of the cuvette.

Temperature dependent H_2 production assays were collected identically to routine assays with the additional temperature control via a recirculating water bath running through the cuvette holder. Temperature measured directly via a thermocouple.

2.5.2 – H/D Exchange – Samples of 100 nM H_2ase were prepared in 50 mM phosphate buffer at the indicated pH and 1 mM $Na_2S_2O_4$ to maintain the active enzyme and samples were exchanged into 100% D_2. The Raman scattering peak at 3430 cm^{-1} was reported as detailed in 2.3.7.

2.5.3 – S^0 Reduction – Samples of 1 mM polysulfide (generated as in inhibition experiments [2.4.1]) were anaerobically mixed with 100 nM H_2ase in 50 mM phosphate buffer pH 7.0 and purged with N_2. Next a concentrated stock solution of methyl viologen (MV) and $Na_2S_2O_4$ was injected to a final concentration of 1-10 mM MV and 2-20 mM

$Na_2S_2O_4$ respectively, initiating the timing of the kinetics experiment. GC measurements of the headspace were measured using a HP-PLOT U column for separation of the H_2S. Control experiments showed no H_2S production in the absence of the SHI.

2.5.4 – CO Inhibition - CO inhibition studies were carried out identically as above, but the headspace was flushed with CO gas for 10 minutes prior to initiation under vigorous stirring resulting in a saturated CO solution. S^0 inhibition studies were performed by the inclusion of 2 mM Na_2S_{5-8} polysulfide solution made by mixing elemental sulfur with sodium sulfide at 3:1 ratio anaerobically until completely dissolved.[6]

2.5.5 – Temperature dependent MV^+/MV^{2+} equilibrium - The temperature dependent equilibrium with 500 μM MV and 5% H_2 was investigated over a temperature range from 10-95˚C by UV-Vis spectroscopy on a Cary UV-Vis spectrometer equipped with a thermoelectric temperature control module in double beam mode using a H_2O cell as a reference. Temperature was measured directly with a thermocouple.

2.6 – Data analysis

2.6.1 Transient kinetics fitting – Transient infrared data for the Pf SHI photo-reduction experiments were performed using a global model described pictorially below and described further in Chapter 5. Kinetic traces from the 1920 (Ni-L), 1948 (Ni_a-S), 1954 (Ni_a-SR) and 1967 (Ni_a-C) cm^{-1} transients were fit globally in IGOR under the following conditions: Ni_a-S transients were fit with three global rates, k_1 and k_2 corresponding to

Ni_a-C production and k_4 corresponding to formation from Ni-L, Ni_a-C in addition to the two coupled rates (k_1 and k_2) was fit with an additional coupled rate k_3 representing reformation from Ni-L and another uncoupled rate k_5 of decay by reduction to the Ni_a-SR^- state, Ni-L transients were fully fit by the two global rates k_4 and k_3, and Ni_a-SR was fit locally by a single rate k_6 resulting from protonation of Ni_a-SR^-.

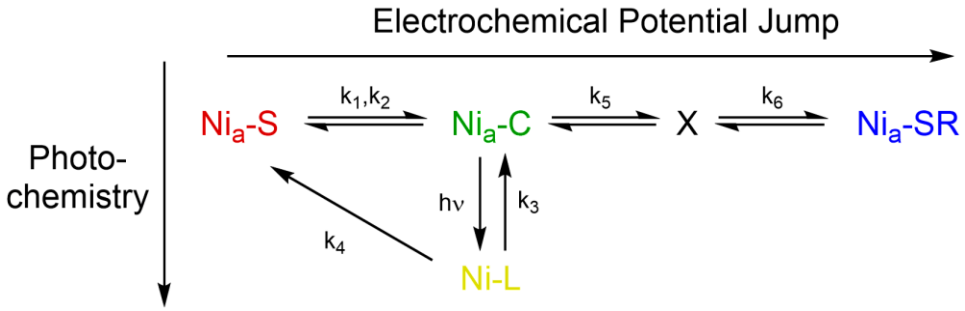

Figure 2.4 – Kinetic fitting model for global fitting analysis.

2.7 – References

(1) Chandrayan, S. K.; Wu, C. H.; McTernan, P. M.; Adams, M. W. *Protein Expres Purif* **2015**, *107*, 90.

(2) Schut, G. J.; Adams, M. W. W. *J Bacteriol* **2009**, *191*, 4451.

(3) Verhagen, M. F. J. M.; O'Rourke, T.; Adams, M. W. W. *BBA-Bioenergetics* **1999**, *1412*, 212.

(4) Zhang, H.; Zhou, Z.; Yang, B.; Gao, M. Y. *J Phys Chem B* **2003**, *107*, 8.

(5) Talapin, D. V.; Nelson, J. H.; Shevchenko, E. V.; Aloni, S.; Sadtler, B.; Alivisatos, A. P. *Nano Lett* **2007**, *7*, 2951.

(6) Ma, K. S.; Weiss, R.; Adams, M. W. W. *J Bacteriol* **2000**, *182*, 1864.

Chapter 3

Steady State Kinetic Investigations of a Model [NiFe] H_2ase Mechanism.

Abstract: Hydrogenases (H_2ases), enzymes which catalyze the reversible oxidation of H_2, have attracted significant interest as models for biomimetic development of efficient hydrogen production catalysts under mild conditions. To develop biomimetic catalysts, a fundamental understanding of the structure and chemical mechanism is a prerequisite. To this end, numerous studies have focused on the structure of the H_2ase enzymes, but the chemical mechanism has been less investigated by traditional enzymology techniques. In this chapter, an extensive kinetic analysis of the reactivity of a prototypical [NiFe] H_2ase from the hyperthermophilic organism *Pyroccocus furiosus* is presented. Using pH and kinetic isotope effects aspects of the rate determining step were determined, which involves the release of H_2 in proton reduction with a competitive intramolecular proton transfer step. Additionally, competitive inhibition studies revealed fast gas diffusion to the active site relative to the lifetime of the Ni_a-S state and competitive electron transfer within the various subunits of the *Pf* SHI. The results shed some light on the chemical mechanism of the H_2ases, but also implicate a multitude of chemical processes which occur faster than the rate determining step, limiting the utility of traditional steady state kinetic analysis of this enzyme.

3.1 - Introduction

H_2ases catalyze a deceptively complex reaction; the reversible reduction of protons to molecular hydrogen described in equation (1).[1-7]

$$2\,H^+(aq) + 2\,e^- \leftrightarrow\ H_2(g) \quad (1)$$

Despite the apparent simplicity of the overall chemical reaction, this process has proven to be quite complex in even the simplest systems. The reaction as written in Equation 1 is not an elementary reaction as defined by chemical kinetics, which describe

reactions with at most two molecules (excluding some three body gas phase reactions). The elementary steps necessary to facilitate the *catalytic* proton reduction reaction include proton transfer, electron transfer or proton-coupled electron transfer to the catalyst, any additional chemical steps within the catalyst itself necessary to form H_2 and eventual H_2 release.[8-12] The reaction in equation 1 including the contributions of the catalyst must at a minimum involve ten states as detailed in Figure 3.1 A. The situation described in Figure 3.1 already represents a sophisticated kinetic equilibrium which involves 36 coupled microscopic rate constants, an unsolvable problem analytically. Figure 3.1 implies a single active metal which can undergo protonation and reduction. This picture is slightly deceptive since there are no true monometallic (i.e. no additional ligands or additional metal centers) proton reduction catalysts. To facilitate the proton reduction reaction multiple metals or metal ligands are used to store protons and/or electrons to mitigate the demand of any single metal site to be both nucleophilic enough to bind protons and electrophilic enough to be reduced.[13-20] These contributions further complicate the chemical scheme shown in Figure 3.1A, where each step of protonation and reduction may involve numerous other equilibrium states of charge distribution within the catalyst.

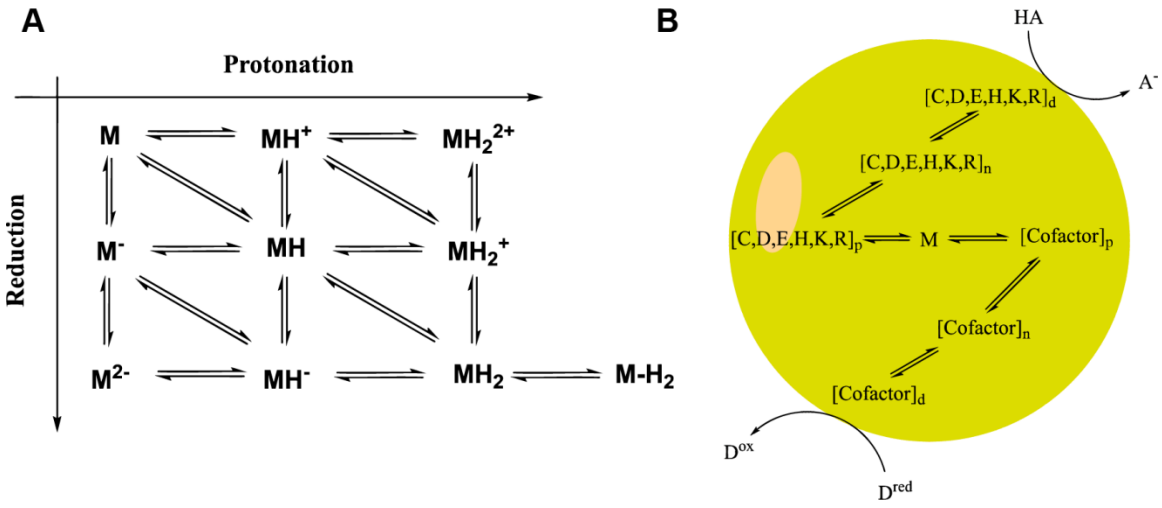

Figure 3.1 – Aspects of proton reduction at metal centers and in protein scaffolds. A) Schematic representation of proton reduction chemistry kinetics at a metal center. Red equilibrium arrow indicates an isoelectronic and isoprotic process of H_2 formation at the metal center. B) Enzyme based intramolecular electron and proton transfer model for an enzyme with n proton transport components ($[C,D,E,H,K,R]_x$, ionizable amino acids) and n redox cofactors ($[Cofactor]_x$) connected to the active site M.

The basic components of small molecule reaction kinetics are further complicated in enzymatic systems due to the complexity of the biopolymer protein surroundings of the active cofactor. This is especially true of the various gas processing enzymes, which perform energetically difficult reactions by isolating reactivity to their buried protein core where their active sites are harbored.[21] The advantage of sequestration of the active site comes at a molecular price since reactants must then be transported over large distances from the solution interface to the buried core. For H_2ases, the reactants for H_2 production are electrons and protons. All H_2ases known to date, excluding the [Fe] only H_2ases and [FeFe] H_2ases from green algae, contain additional redox non-innocent cofactors. Redox

cofactors in the H_2ases are most typically standard cubane [Fe_4S_4] clusters, but have also been observed as [Fe_3S_4], [Fe_4S_3], [Fe_2S_2], flavins or hemes. These cofactors can store and shuttle one or more electrons and act as molecular wires to the active site from the protein surface.[22-26] Additionally, both [NiFe] and [FeFe] H_2ases contain conserved ionizable amino acid groups that allow exchange of protons from the surface to the active site through multiple protonation/deprotonation steps.[6,27,28] Thus from the most basic picture of proton reduction catalysis illustrated in Figure 3.1A we can further describe enzyme systems schematically by an illustration described in Figure 3.1B. Including the electron and proton transport chain increases the number of potential states exponentially illustrating clearly the complexity of the enzymatic system despite the simple chemical reaction being catalyzed.

Given the complex nature of enzymatic proton reduction catalyzed by the H_2ases, it may be expected that numerous steady states would exist under any set of conditions and thus study of the mechanism of these enzymes would be intractable, however this is not the case. In actuality, of all the potential possible active site configurations that could be formulated (Figure 3.1A) only the states along the diagonal are significantly populated for the [NiFe]/[FeFe] H_2ases. This is clear from examination of the active site infrared and EPR properties under various chemical conditions which reports on the various protonation and reduction states of the [NiFe]/[FeFe] core.[29-35] The involvement of other proton and electron configurations at the active site may indeed be involved in the chemical mechanism of the H_2ases, but they represent kinetically or thermodynamically unfavorable states which only exist transiently. Kinetically or thermodynamically unstable states can be probed under certain conditions by kinetics. By examining the

array of chemical reactions that occur with H_2ases under various conditions (assays) the mechanism of action of these enzymes has been advanced substantially. The various assays used to measure H_2ase are described in Figure 3.2.

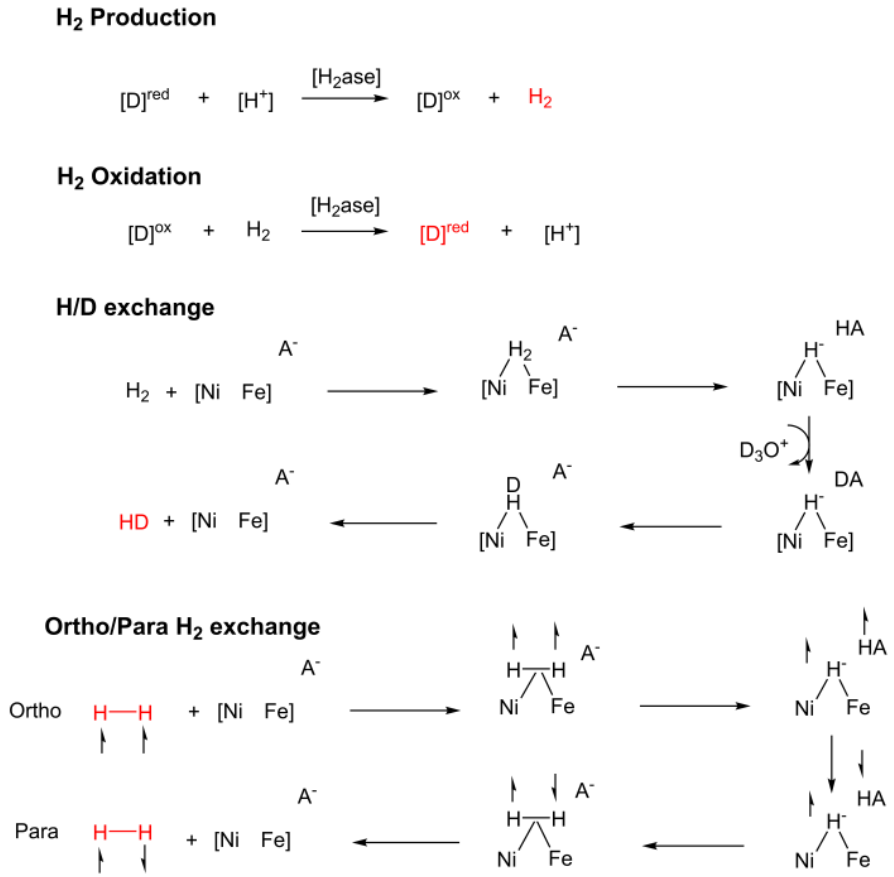

Figure 3.2 – Enzyme assays for kinetic analysis of H_2ase reactivity. Red species indicate chemical species used to probe the activity of the enzyme in various assays. H/D exchange can be reversed, i.e. that D_2 can be exchanged into H_2O to HD.

The simplest H_2ase assay, from an enzyme kinetics point of view, is the ortho/para exchange reaction. In this reaction, a nuclear spin isomer enriched H_2 atmosphere is exposed to a solution of H_2ase. The enzyme heterolytically cleaves the

enriched isomer and with no proton exchange or electron exchange reforms the H_2 molecule with a scrambling of the nuclear spin composition towards the thermodynamic level of 25% para, 75% ortho. This assay probes specifically the H_2 binding, heterolytic cleavage and release processes as well as minor contributions from H^+ exchange. As a consequence, the assay is invariant towards site directed mutagenesis of amino acid residues thought to be involved in the proton transport chain as well as tuning/knockout of electron carrying cofactors.[27,28] Due to experimental difficulties in performing this assay, it has largely been ignored as a tool for the study of these enzymes, but for those which an ortho/para exchange rate has been reported it has been reported to be very similar to the overall maximal H_2 production rate, which indicates that these processes involve similar rate determining steps.[5,27,36-40]

The H/D exchange is a slightly more complicated assay, in which the enzyme is placed in deuterated water and exposed to an atmosphere containing normal isotopic composition H_2.[27,28,40,41] Under these conditions the enzyme must bind and heterolytically cleave H_2, but the proton from this reaction is exchanged with the solvent deuterons and eventually recombined with the hydride to form the mixed isotope product HD or the fully deuterated D_2. By comparing this activity with the ortho/para exchange activity, one can examine the effects of proton transport.[28] Dementin et al. showed through site directed mutagenesis studies that various point mutations of conserved ionizable amino acids in the [NiFe] H_2ase from *Desulfovibrio fructosovorans* drastically affected the H/D exchange rate whereas they negligibly affected the ortho/para conversion.[27] Both the ortho/para conversion and H/D exchange yield useful phenomenological properties of the

H_2ases, but difficulties arise in the explicit assignment of elementary proton transfer rates presumably because the proton transfer rate is fast relative to H_2 binding or H_2 release.[40]

The final kinetic activity assays for H_2ases involves the full chemical reaction for which they catalyze, the formation or consumption of H_2.[42,43] This reaction is the most complex kinetic assay because it involves all components necessary for catalysis, H_2 binding or release, heterolytic cleavage, electron and proton transfer. Substantial advancement in the mechanistic investigation of H_2ases has been achieved by the analysis of these reactions from enzymes adsorbed onto electrodes.[24,44-46] This has been useful because it allows for the control and modulation of diffusional processes in reactivity through rotating disk protein film voltammetry. Additionally, it has been critical in the investigation of enzyme inhibition by O_2 under catalytic conditions since redox mediators typically react with molecular oxygen directly complicating the observed trends.[47,48] By comparison of this reactivity with that of the H/D exchange, a comparison of the rate of electron transfer relative to proton transfer and active site chemistry can be made.

Unfortunately, an exhaustive and comprehensive kinetic characterization of any one hydrogenase, [NiFe] or [FeFe], has not been performed.[40] The most thorough kinetic studies of H_2ase activity involve the [NiFe] H_2ases and they will be discussed exclusively herein. The study of the kinetic behavior of H_2ases has chiefly focused on the rate determining step, which is typically the process being interrogated in steady state kinetics, particularly when the turnover rates are faster than 100 s^{-1}. For numerous H_2ases, they exhibit different activation energies for the H_2 oxidation relative to H_2 production, different forward and reverse maximal reaction rates and different inhibition properties indicating different rate determining steps for the two reactions.[23,49-51] Despite

these differences, due to the complexity of the enzyme and lack of experimental techniques for investigating pre-steady state kinetics, the rate determining step in H_2 oxidation and H_2 production is still under debate.[6,30,52,53]

To supplement and enrich pre-steady state mechanistic investigations of [NiFe] H_2ases, the steady state kinetics of a model [NiFe] hydrogenase from a hyperthermophilic organism *Pyrococcus furiosus* were investigated, particularly those involved in proton reduction. The mechanistic implications of these findings as well as the questions that these kinetic experiments are incapable of answering are discussed.

3.2 – Results and Discussion

3.2.1 – Proton Reduction: The Role of Proton Transport

Proton reduction in any hydrogenase system requires four prerequisite steps before active site chemistry can occur; protonation of the enzyme, reduction of the enzyme, intramolecular proton transport (PT) and intramolecular electron transport (ET). These four prerequisite steps can be separated into two categories, intermolecular (bimolecular) and intramolecular (uni-molecular) substrate transfer. Intermolecular proton (or electron) transfer kinetics can be described as in equation 3.2.

$$H^+(aq) + H_2ase \leftrightarrow H_2ase^+ \quad (3.1)$$

$$\frac{d[H_2ase^+]}{dt} = k_1 \cdot [H_2ase] \cdot [H^+] - k_{-1}[H_2ase^+] \quad (3.2)$$

where k_1 and k_{-1} are the forward and reverse rate constants of the reaction in equation 3.1. Under the condition that intermolecular PT is rate determining in proton reduction by a [NiFe] H_2ase, the observed forward rate constant should be quasi-first order with respect to both H^+ and the enzyme (no composite reactions technically have order). A similar

situation can be derived for an intermolecular ET process and an analogous first order relationship would be expected for the reductant, in this case methyl viologen, and catalyst. Unfortunately, by steady state methods there is no direct readout of the rate of proton or electron association and thus the overall proton reduction kinetics, as measured by production of H_2, must be used as the effective readout method. This adds a level of complexity which includes the intramolecular ET or PT as well as active site chemistry including hydride formation, protonation, reduction and H_2 release. Using gas chromatography to analyze the product (H_2) formation rate, the concentration dependence of H^+ and H_2ase were investigated and are shown below in Figure 3.3A.

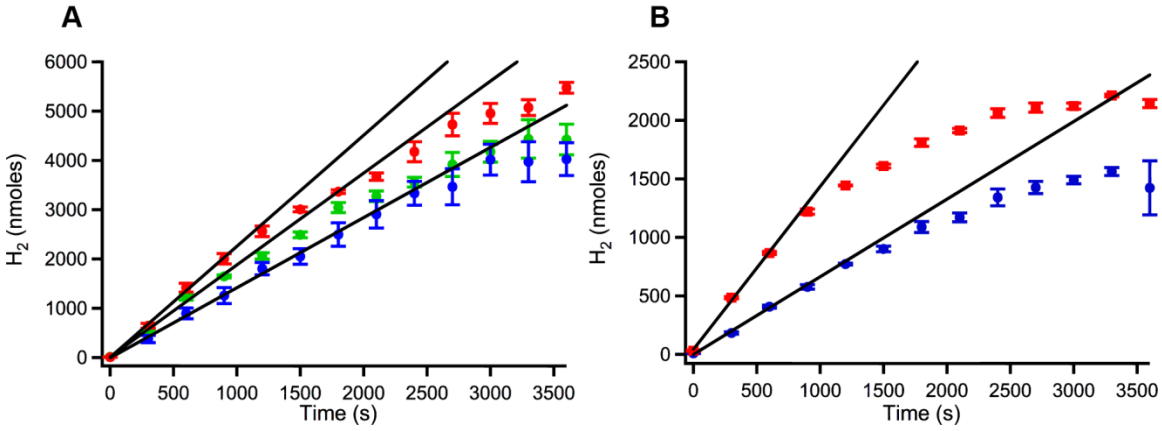

Figure 3.3 – [H^+] and [H_2ase] concentration dependence on proton reduction rates. A) pH dependence on proton reduction activity. Red circles represent pH 6.3, green pH 7.0 and blue pH 7.7. Data were fit to the initial 900 seconds and error is reported as the standard deviation of three independent measurements. Black lines indicate linear fits to the initial 900 seconds. B) Dependence of proton reduction kinetics on[H_2ase] concentration. Red indicates 40 nM H_2ase, and blue indicates 20 nM H_2ase and error is

reported as the standard deviation of three independent measurements. Black lines indicate linear fits to the initial 900 seconds.

The proton reduction rate observed at buffered $[H^+]$ concentrations from $2.0 * 10^{-8}$ (pH 7.7) to $5.0 * 10^{-7}$ (pH 6.6) M was found to range from 58 s^{-1} to 62 s^{-1}. Under these conditions, at early time within a given pH the rate was observed to be linear with respect to time (zero order) which is consistent with the $[H_2ase]$ and $[H^+]$ not changing as a function of time. By varying the initial H^+ concentration over an order of magnitude the initial rate was shown to change only 6%. If intermolecular PT were rate determining the initial rate dependence on $[H^+]$ should be linear, consistent with a first order relationship described in equation 2. Since this is not the case, it is concluded that the rate determining step for proton reduction is not intermolecular PT. This is not surprising since proton association processes are typically diffusionally controlled with association constants > 10^{10} M^{-1} s^{-1} for most acidic ionizable amino acids.[54] Alternatively, the variation of enzyme concentration should affect the kinetics of H_2 production with respect to all catalyst associated processes, i.e. since all rate determining processes must involve the enzyme the overall rate should be first order with respect to enzyme. Consequently, at low enzyme concentrations, doubling of the enzyme concentration does in fact double the rate as expected for a first order process with respect to enzyme (Figure 3.3B).

Relative to the single step intermolecular PT, intramolecular PT kinetics are much more complicated. Intramolecular PT can be modeled to a first approximation by a series of proton hoping processes. Due to lack of structural information including donor and acceptor pK_a's and the number of donor-acceptor pairs required to exchange a proton

from the bulk with the enzyme active site, the PT kinetics are at this point difficult to address. Additionally, even for structurally defined enzymes with known x-ray crystal structures, water molecules have been observed to be present in most H_2ase structures, but water content in the active solubilized structure has not been examined.[55-59] Despite this, estimates can be made based on extrapolations as to what the pH effect on intramolecular PT kinetics should yield based on a rate determining step of intramolecular PT. In the simplest hydrogenases, at least three ionizable amino acids are involved in the proton transfer pathway to the active site based on distance of the active site to the solvent exposed surface implicating four intramolecular proton exchange centers. For a simple set of bimolecular coupled reactions such as described below in Equation 3.3-3.5, the rate laws can be described as in Equation 3.6-3.9.

$$\mathbf{HA} + \mathbf{B^-} \underset{k_{-1}}{\overset{k_1}{\rightleftharpoons}} \mathbf{A^-} + \mathbf{HB} \qquad (3.3)$$

$$\mathbf{HB} + \mathbf{C^-} \underset{k_{-2}}{\overset{k_2}{\rightleftharpoons}} \mathbf{B^-} + \mathbf{HC} \qquad (3.4)$$

$$\mathbf{HC} + \mathbf{D^-} \underset{k_{-3}}{\overset{k_3}{\rightleftharpoons}} \mathbf{C^-} + \mathbf{HD} \qquad (3.5)$$

$$\frac{dHA}{dt} = k_{-1} \cdot [A^-] \cdot [HB] - k_1 \cdot [HA] \cdot [B^-] \qquad (3.6)$$

$$\frac{dHB}{dt} = k_1 \cdot [B^-] \cdot [HA] + k_{-2} \cdot [B^-] \cdot [HC] - k_{-1} \cdot [B^-] \cdot [HA] - k_2 \cdot [C^-] \cdot [HB] \qquad (3.7)$$

$$\frac{dHC}{dt} = k_2 \cdot [C^-] \cdot [HB] + k_{-3} \cdot [C^-] \cdot [HD] - k_{-2} \cdot [B^-] \cdot [HC] - k_3 \cdot [D^-] \cdot [HC] \qquad (3.8)$$

$$\frac{dHD}{dt} = k_3 \cdot [D^-] \cdot [HC] - k_{-3} \cdot [HD] \cdot [C^-] \qquad (3.9)$$

The H_2ases function well both in forward and reverse direction and thus the reversible rate constants must be considered, significantly complicating the analysis. If intramolecular PT were rate determining, the quantity dHD/dt would be directly

proportional to the dH_2/dt of the overall reaction based on fast subsequent active site chemistry. Thus solving for dHD/dt would yield a function whose form would describe the reactivity of the enzyme. Under steady state conditions, such as those applied in the steady state kinetic assay of pH dependent proton reduction rate;

$$\frac{dHB}{dt} = \frac{dHC}{dt} = 0 \quad (3.10)$$

$$\frac{dHD}{dt} = -\frac{dHA}{dt} = k_1 \cdot [HA] \cdot [B^-] - k_{-1} \cdot [A^-] \cdot [HB] \quad (3.11)$$

where [HA], $[A^-]$, [HB] and $[B^-]$ are the concentrations of the initial donor acceptor pair of ionizable amino acids. Thus for an arbitrarily long proton transfer chain under steady state conditions, intramolecular proton transport can be treated as the relative population of the initial two donor/acceptor sites due to reversibility. Under the conditions of the assay described by Figure 3.3A, pH remains constant over the course of the reaction, thus if the pKa of HA and HB were known, the initial concentrations of all species [HA], $[A^-]$, [HB] and $[B^-]$ could be determined. While the microscopic rate constants k_1 and k_{-1} are not known, using the constant solution pH and varying the associated pK_a values for HA and HB over a broad biologically relevant window (4-7), one can calculate the potential fractionation of both HA/A^- and HB/B^-. Since k_1 and k_{-1} are pH independent, their effect on the pH dependent rate enhancement of dHD/dt is expected to be negligible, thus their contributions can be neglected in this analysis. By varying the pK_a of both HA and HB and examining the effect on an arbitrary initial rate dHD/dt determined by k_1 and k_{-1} estimates of 10^5 s^{-1} and 10^5 s^{-1} respectively, a two dimensional scheme for the enhancement of dHD/dt (ΔdHD/dt) from pH 7.7 to 6.3 can be constructed for various pK_a's of HA and HB and is shown in Figure 3.4.

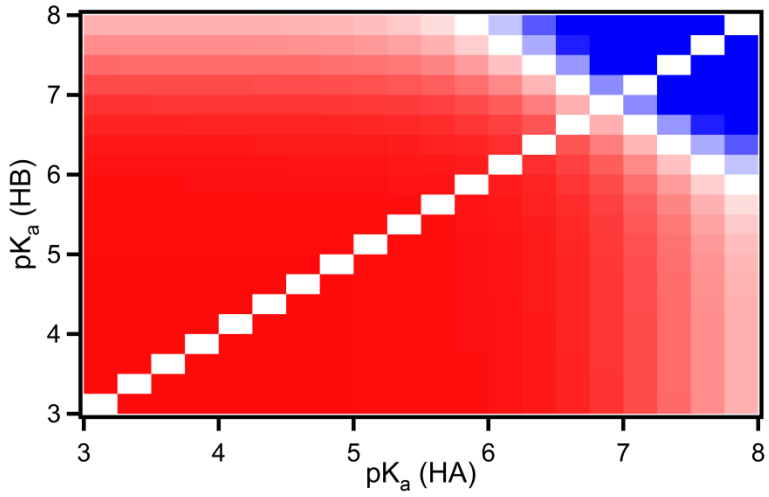

Figure 3.4 – Kinetic simulations of intramolecular PT with various initial H^+ acceptor/donor pK_a pairs. Data simulated with initial rates determined at pH 6.3 and 7.7 and the value reported is the percent difference in rate at the more acidic pH relative to the more basic pH at each pK_a pair and arbitrary rate constants k_1 and k_{-1} (10^5 s^{-1}).

It is clear from Figure 3.4 that if intramolecular PT is rate determining in proton reduction by the *Pf* SHI, the proton transport network must have a small pK_a difference between HA and HB (<0.08) such that pH changes do not significantly affect the population of the ratio of HA/B relative to HB/A. The observed rate enhancement of 6% with a proton concentration increase of over an order of magnitude is thus more consistent with a proton transfer step not being rate determining, but possibly on similar timescales which may slightly alter the observed rate constant. Thus despite not knowing the pK_a or length of the proton transfer chain, the possibility of intramolecular PT being rate liming is improbable, although not impossible. This analysis suggests intramolecular PT may be faster than enzyme turnover, but says nothing about how fast, or what

residues are involved in intramolecular PT. Site directed mutagenesis may be a method to further interrogate intramolecular PT.

Another steady state kinetic method that can interrogate, among other things, the role of proton transport/movement in catalysis by H_2ases is the kinetic isotope effect of proton/deuteron reduction activity. When substituting the solvent isotope composition from H_2O to D_2O in the presence of a reductant (MV^+), the enzyme must reduce deuterons, which have different zero-point bond energies in the X-(H/D) bonds and tunneling probabilities. These effects can vary substantially depending on the mechanism of X-(H/D) bond cleavage. For example in semi-classical transition state theory, the difference in zero point bond energy can result in KIEs of 1-7 depending on the energy of the transition state relative to the vibrational energy in the ν_0 X-(H/D) mode. Alternatively, due to the light nature of protons, adiabatic tunneling between donor and acceptor vibrational potential wells can occur, where isotope effects vary substantially from those derived from transition state theory. The magnitude of the KIEs for proton tunneling reactions are typically much greater than 10 and are modulated by the de Broglie wavelength of the proton/deuteron and the barrier width rather than height.[8,11,60-63] The steady state kinetic isotope effect of proton/deuteron reduction by the *Pf* SHI is shown in Figure 3.5 below.

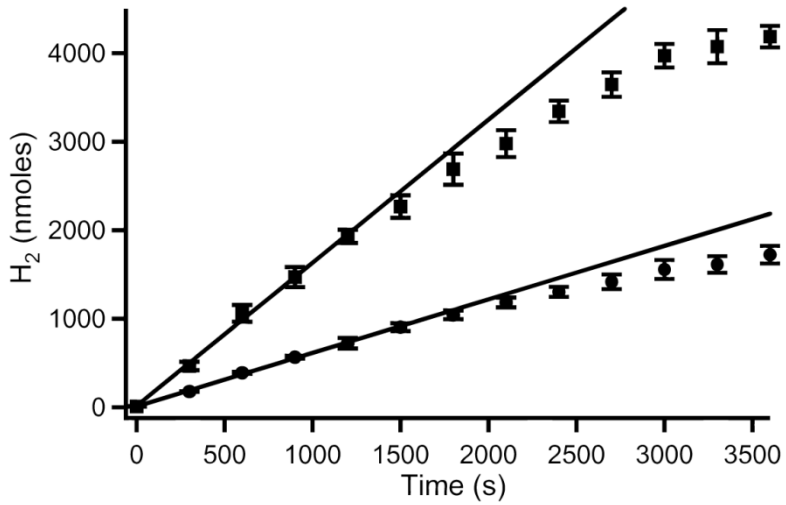

Figure 3.5 – Proton and deuteron reduction activity of *Pf* SHI. Gas chromatography analysis of the steady state KIE of proton reduction by *Pf* SHI at pH 7.0 (squares) and pD 7.0 (circles) with 5mM MV^+, 10 mM $Na_2S_2O_4$ and 50 mM phosphate buffer. Error bars represent the standard deviation between three identical experiments.

The deuteron reduction activity of the SHI (20 s^{-1}) is observed to be 3.1 fold slower than the rate of proton reduction (61 s^{-1}). Little to no KIE is expected for a rate determining step involving either intra or intermolecular ET, thus the observed KIE indicates either a proton dependent rate determining step or a proton dependent process which is competitive with the rate determining step. In the former case, the KIE would be a true measure of the KIE of the rate determining step, whereas in the latter case, the observed KIE would be an underestimate.

Based on the lack of significant pH differences in reactivity, but a large KIE it is concluded that either intramolecular PT is very close to rate determining and has a very large KIE (>3) which is manifested as an apparently smaller isotope effect, or that a chemical step involving proton/deuteron bond breaking is competitive for the rate

determining step, but is not affected by pH such as H_2 release from the active site. The latter has been proposed by others to be the rate determining step for standard [NiFe] H_2ases such as those found in the periplasm of *Thiocapsa roseopersicina*. A third possibility is that both of these steps, H_2 release and intramolecular PT are nearly identical in time and thus both affect the steady state behavior substantially. If proton exchange to the bulk and H_2 release from the active site are competitive for the rate determining step then in the presence of D_2 gas and H_2O solvent, the rate and quantity of formation of the mixed isotope product HD should be affected by pH. To probe this possibility we examined the H/D exchange activity of this enzyme by Raman scattering of the headspace of an enzymatic sample as a function of pH and the results are shown in Figure 3.6 below.

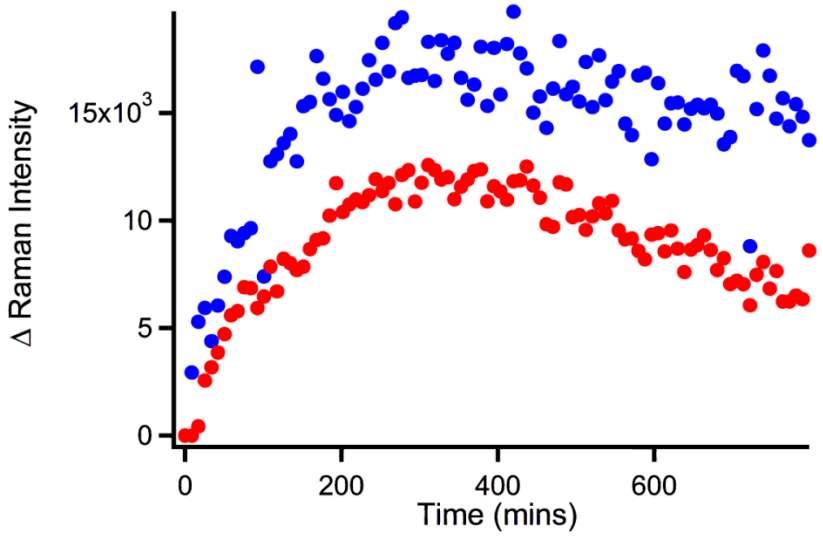

Figure 3.6 – pH dependence of H/D exchange activity of *Pf* SHI. H/D exchange activity probed by Raman spectroscopy at pH 6.3 (blue) and 7.7 (red). Samples were prepared in 50 mM phosphate buffer at the indicated pH and 1 mM $Na_2S_2O_4$ to maintain the active

enzyme and samples were exchanged into 100% D_2. The Raman scattering peak at 3430 cm^{-1} was integrated and reported herein for the HD quantification.

The H/D exchange data show two interesting properties; firstly, the rate of HD production is higher at pH 6.3 then at 7.7 by 16%, similar to the overall pH dependence of the H_2 production assay, and secondly, that the quantity of HD produced is approximately 50% more at pH 6.3 relative to the HD production at 7.7. These data are consistent with a model in which proton exchange to the bulk is competitive with the product release, but product release is in fact rate determining. In this model, pH can modulate the isotope exchange of the bound H_2 molecule before it is released due to the acceleration of the intramolecular PT at lower pH.

The above data clearly demonstrate that proton reduction is largely modulated by intramolecular PT and H_2 release at room temperature. *Pyrococcus furiosus* is a hyperthermophilic organism growing optimally at 100˚C naturally in hydrothermal vents and thus the enzymatic activity of the *Pf* SHI may be drastically different at higher temperatures relative to the behavior observed at room temp, nearly 80˚C below the optimal temperature of the organism. This point has been acknowledged in the literature and conflicting reports on the temperature dependence of the kinetic properties of this enzyme have been reported.[49,64] In order to investigate any potential temperature dependent reactivity of the SHI we investigated the proton reduction activity of the enzyme at temperatures ranging from 10-90˚C as well as the KIE over this range. The data are reported below in Figure 3.7.

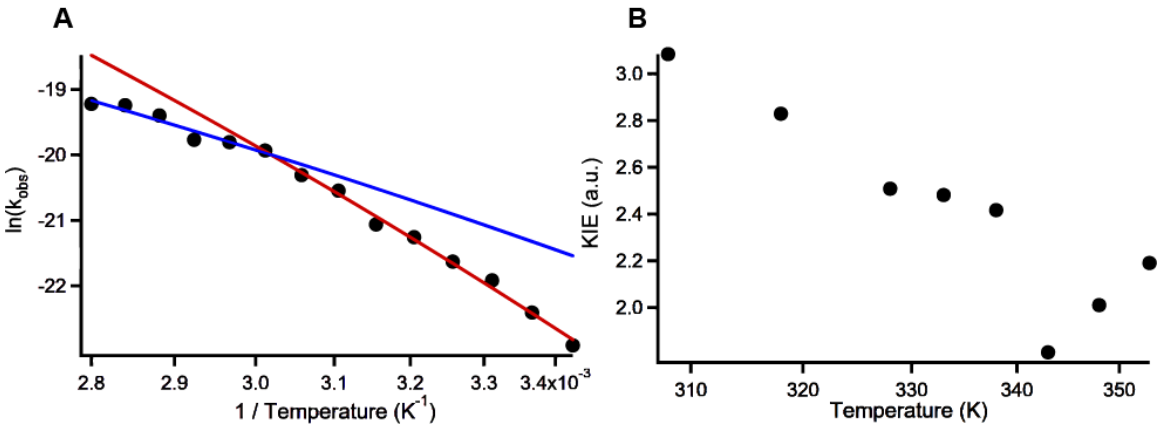

Figure 3.7 – Temperature dependent proton reduction and KIE for *Pf* SHI. A) Arrhenius plot of proton reduction kinetics of the *Pf* SHI from 10 to 90˚C. The data were fit to two independent linear regimes, >60˚C (blue) and <60˚C (red) with activation barriers of 31 kJ/mol and 58 kJ/mol respectively. B) Temperature dependent KIE for *Pf* SHI from 35-90˚C. Temperature dependent D_2 production was measured similarly as H_2 (data not shown)

It is apparent from Figure 3.7 A that more than one activation barrier is required to fit the experimental data with a break point at approximately 60˚C. The two regions were fit to two Arrhenius equations independently above and below 60 ˚C with E_a of 31 +/- 2 and 58 +/- 1 kJ/mol respectively. This break point is consistent with previous reports, but the additional break point where the enzymatic bias was observed to shift dramatically from H_2 oxidation to H^+ reduction at 80 ˚C was not observed. Although the data show little evidence of this bias shift transition, more temperature points above 90˚C would be useful in determining this explicitly, but the protein was not stable for long periods of time under these conditions. Additionally, the activation barriers calculated in the low temperature regime was 50% of that reported previously (108 kJ/mol), whereas

above 60˚C E_a was very similar to that reported for the 60 to 80˚C region previously (28 kJ/mol). Based on the model proposed above where product release is rate determining with a competitive rate determining step of intramolecular PT these barriers may measure these processes directly. Thus the barrier for H_2 release would be 58 kJ/mol which is similar to that predicted by theory (60 kJ/mol).[65] The second barrier may correspond to the barrier of intramolecular PT which may prove useful to identify the rate determining residue(s) involved in this process.

These data are further consistent with the temperature dependent KIE, where the relatively high KIE of ~3 is reduced to 2 with an approximate break point near 60 ˚C. It is noteworthy that the KIE decreases upon raising the temperature. This could be described by a transition from a primary isotope effect of $H_2(D_2)$ release to a secondary isotope effect of side chain reorganization after a fast proton transfer event. Typically in proton conduction, proton transfer rates are fast relative to the reorganization due to pre-aligned hydrogen bonded networks which after PT must reorient to pass the proton onto the next acceptor. These processes could be further examined by site directed mutagenesis and pH dependent infrared spectroscopy.

3.2.2 – Active Site Chemistry of Proton Reduction

Another steady state method for probing the mechanism of proton reduction in these enzymes is the inhibition assay with CO.[64,66-71] For standard [NiFe] H_2ases, CO binds to the active site terminally to nickel, inhibiting the H_2 oxidation or H^+ reduction activity.[32,72] This reactivity is thought to be correlated to O_2 inhibition due to the similar size and diffusion rate of CO and O_2.[28,30,68,71,73,74] CO is a strong σ-donor and π-acceptor

ligand and thus is expected to bind to metal centers which may have H_2 affinity, where H_2 also bonds through both σ-donation and π-back bonding, but to a much lesser extent due to smaller ligand field splitting.[75-77] Consistent with this, the binding of CO has been shown to have an activation barrier of 9 kJ/mol, a low barrier relative to the H_2 binding energy.[29] The [NiFe] core binds CO in only one of the stable redox states of the enzyme, the Ni_a-S state, which then rendered the active site redox inert, indicating that the presence of the bridging ligand at the active site blocks CO addition.[32,34,77,78] This is further supported by the observation that the photo-product of the Ni_a-C state, Ni-L can bind CO, but Ni_a-C cannot.[35,78] The CO inhibition effects on the proton reduction by the *Pf* SHI are shown in Figure 3.8.

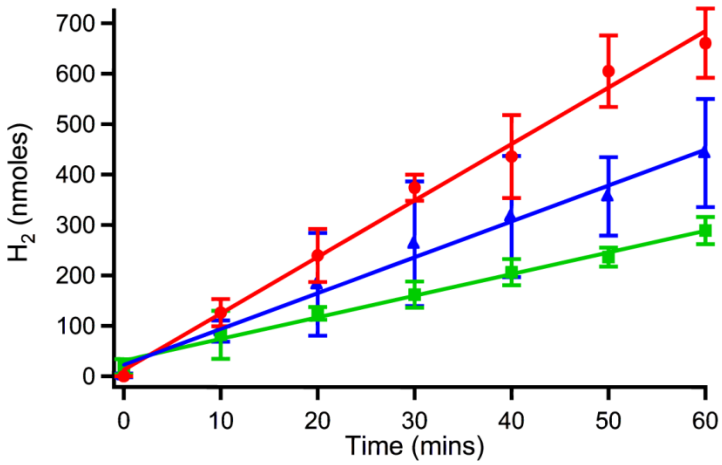

Figure 3.8 – Reversible inhibition of proton activity by *Pf* SHI. H_2 production kinetics from 1 nM H_2ase from 1 mM MV^+ and 2 mM $Na_2S_2O_4$ under N_2 (red), CO (blue) and N_2 with 2 mM polysulfides (green).

CO was found to inhibit (64%) the enzyme reversibly indicating that CO does indeed bind to the active site of the *Pf* SHI. This is consistent with recent reports, but is in contrast to initial studies on this enzyme.[64,79,80] CO inhibition is typically thought to be a strong indicator of the bias of the [NiFe] H_2ase active site, although it is rarely used in the H^+ reduction assay.[30] The mechanism of inhibition is unclear at this point due to the fact that proton reduction is thought to occur at the bridging position, in spite of theoretical investigations which typically consider the final H_2 formation step terminally at nickel or iron.[65,81-84] Additionally, it is noted that the proton reduction mechanism of the [FeFe] H_2ases occurs only at the distal Fe indicating a mono-metallic H_2 cleavage mechanism.[85-87] A mechanism in which CO binding to the active site competes with proton and electron transfer to the Ni_a-S state is consistent with the steady state behavior of this enzyme and previous spectroscopic investigations. This indicates that PT or ET to the Ni_a-S state must occur on similar timescales as CO diffusion to the active site, placing a relative timescale on the PT/ET step. Additionally, the CO off rate must be fast since inhibition is completely reversible and once removed, reactivity is fully restored (data not shown).

The *Pf* SHI has also been shown to have sulfur reduction chemistry transforming elemental sulfur or polysulfides to H_2S.[88,89] The diaphorase unit has been proposed as the sulfur reduction site based on sequence similarity with the sulfate reductases of the γ-β subunits. This provides an interesting opportunity to probe the enzyme inhibition by competitively diverting electron flow through the enzyme to S^0 instead of H^+. The polysulfide inhibition of the *Pf* SHI is shown in Figure 3.8. The inhibition was observed to be reversible and consistent with the hypothesis that S^0 competes with H^+ for electrons in proton reduction. Additionally, by infrared analysis of the active site (Figure 3.6), no

indication of active site chemistry unique to S^0 relative to any other oxidant was observed indicating coordination chemistry is not occurring or is highly unstable and decomposes to the known steady states. H_2S was determined to be the product of the polysulfide reduction process by GC, but incubation of the oxidized enzyme with H_2S failed to produce reduced states indicating that the reaction is largely irreversible (Figure 3.9). Unlike CO, S^0 or polysulfide can compete for electrons at any stage of catalysis. The observation that the inhibition effect is smaller than the CO inhibition implies that electron transfer is fast relative to catalysis or that sulfur reduction is slow relative to catalysis and/or CO binding. The S^0 reduction activity observed in the *Pf* SHI has been proposed to be a ubiquitous property of H_2ases, and thus may prove to be a unique method for studying ET kinetics relative to proton transfer in steady state experiments.

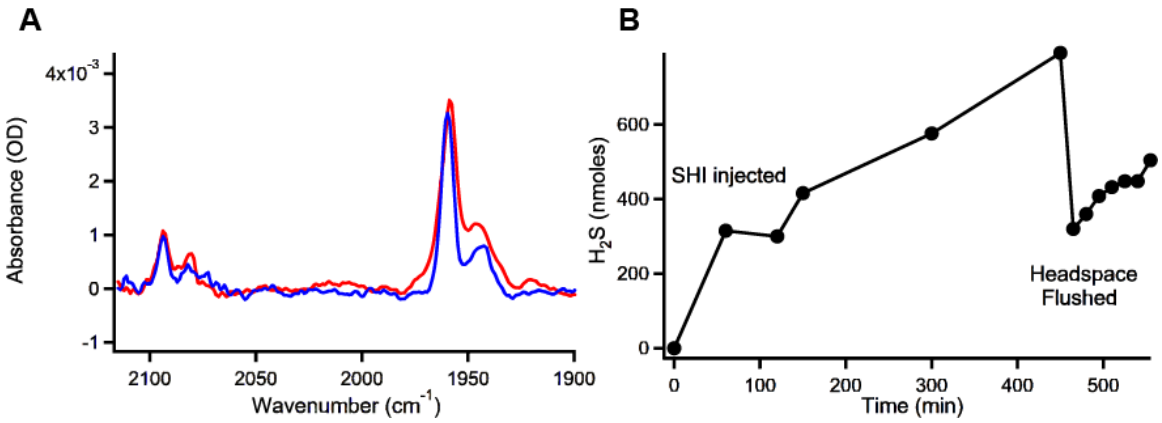

Figure 3.9 – FTIR characterization of the *Pf* SHI active site under H_2S and polysulfide and catalytic H_2S production. (A) FTIR characterization of the *Pf* SHI active site upon incubation with H_2S (blue) and polysulfides $Na_2S_{5\text{-}8}$ (red). (B) H_2S formation from 2 mM MV^+ and 2 mM polysulfide catalyzed by 100 nM SHI at pH 7.0 50 mM phosphate buffer.

3.2.3 Equilibrium and Enzyme Bias

It has been observed that the rate of forward reaction relative to the reverse reaction as defined by equation 3.12 is larger for class I, II and III [NiFe] H_2ases.[7,30,90]

$$2 \cdot A^{ox} + H_2 \leftrightarrow 2 \cdot D^{red} + 2 \cdot H^+ \qquad (3.12)$$

The equilibrium constant for this reaction can be defined as;

$$K_{eq} = \frac{[D^{red}]^2 \cdot [H^+]^2}{[A^{ox}]^2 \cdot [H_2]} \qquad (3.13)$$

for an ideal solution where $[H_2]$ can be determined by Henry's Law as;

$$[H_2] = \frac{\rho_{H_2}}{k_H} \qquad (3.14)$$

for an ideal gas. This reaction "bias" has been proposed to be due to the nature of the intermolecular electron donor-acceptor cofactor, which if too oxidizing to be in thermodynamic equilibrium with H_2 will be incapable of driving proton reduction.[23,26,90] This hypothesis is reasonable, but neglects any other contributions to the bias such as active site bias and PT, which may not be valid. Model complexes based on the active site of the [NiFe] and [FeFe] H_2ases have been synthesized and have been shown to be nearly always uni-directional.[14] Furthermore, examples of [FeFe] H_2ases and [NiFe] H_2ases with similar distal Fe_4S_4 clusters have been shown to have dramatically different biases.[90] A critical question for biomimetic chemists is the origin of this bias, and whether active site models can be expected to display similar biases or are these factors determined by the enzyme matrix.

This issue has been particularly contentious for the *Pf* SHI, which was originally proposed to be the first example of a [NiFe] H_2ase biased towards proton reduction, but was later proposed to be biased towards H_2 oxidation.[49,64,89] Perhaps of more interest than

the overall bias was the apparent temperature dependence of this bias where the bias towards H_2 production was proposed to increase with temperature. This bias could be an intrinsic property of the enzyme, or a consequence of electron donor interactions. To investigate this further, the temperature dependent equilibrium with 500 μM MV and 5% H_2 was examined over a temperature range from 10-95˚C by UV-Vis spectroscopy sensitive to the MV^+ concentration (Fig. 3.10).

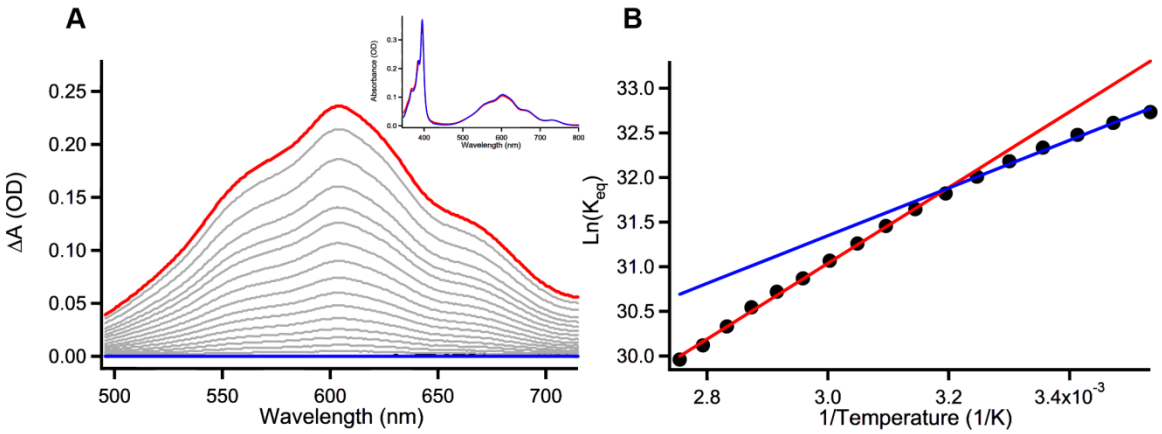

Figure 3.10 – Temperature dependent equilibrium of MV^+/MV^{2+} catalyzed by *Pf* SHI. A) UV-Vis measurements of the temperature dependent equilibrium of MV^+/MV^{2+} catalyzed by *Pf* SHI from 10˚C (blue) to 90˚C (red) in 5 ˚C steps (grey), and a final return to 10˚C (black, behind and identical to blue). Inset shows initial and return UV-Vis at 10˚C. B) Van't Hoff plot for the MV^+/MV^{2+} equilibrium reaction (squares, left ordinate) fit to the data (black line) above 45˚C.

The visible spectrum of the $MV^{+/2+}$ equilibrium with H_2 catalyzed by H_2ase revealed a shift of the equilibrium with temperature towards the oxidation of H_2 as observable by the increase in absorbance of the reaction product MV^+. It is expected that

if the equilibrium were not temperature dependent the MV^+ concentration would decrease due to the loss of solubility of the gaseous H_2. This is described empirically by the temperature dependence of Henry's Law as;

$$k_H(T) = k_H(T^\theta) \cdot e^{-C\cdot(\frac{1}{T}-\frac{1}{T^\theta})} \qquad (3.14)$$

where T^θ is the standard temperature (298 K) and C is an empirically derived proportionality constant defined as;

$$C = -\frac{\Delta H_{solvation}}{R} \qquad (3.15)$$

and has a value of 500 K for H_2. Using this and a modified version of the equilibrium constant expression accounting for unchanging proton concentration the equilibrium described in equation 3.12 can be redefined as;

$$K_{eq} = \frac{[MV^+]^2}{\frac{\rho_{H_2}(T)}{k_H(T)}\cdot[MV^{2+}]^2} \qquad (3.16)$$

Given that the Gibbs free energy of a reaction is defined as;

$$\Delta G^0 = -R \cdot T \cdot \ln(K_{eq}) = \Delta H - T \cdot \Delta S \qquad (3.17)$$

a plot of the $\ln(K_{eq})$ versus 1/T should yield a linear relationship with a slope of $-\Delta G^\circ/R$ for the overall reaction (Van't Hoff plot). The calculated temperature dependent equilibrium is shown in Figure 3.10 A. The data clearly show that this relationship is not obeyed, and the temperature dependence of the Van't Hoff plot varies significantly from the linear relationship <45˚C. In the linear region of the Van't Hoff plot (>45˚C) the ΔH_{rxn} was determined to be 27.6 ± 0.5 kJ/mol. The endothermic ΔH for the reaction as defined in Equation 3.16 suggests a thermodynamic bias towards H^+ reduction. The associated ΔS of -308 ± 1 J/mol*K indicates that the reaction as written is also entropically disfavored and that the enzyme remains biased towards H^+ reduction at all

temperatures. This is consistent with the initially observed bias towards proton reduction. The catalyst independent ΔG^0 of the reaction described in equation 3.12 with MV as the donor/acceptor system can be defined electrochemically using the relationship;

$$\Delta G^0 = -n \cdot F \cdot E \qquad (3.19)$$

where,

$$E = E_{cathode} - E_{anode} \qquad (3.20)$$

For H_2 oxidation at pH 7.0 the thermodynamic potential is defined by the Nernst equation.

$$E = E^0 + \frac{R \cdot T}{n \cdot F} \cdot \log(H^+) = E^0 - \frac{59.2\ mV}{n} \cdot \text{pH} = -414\ \text{mV (pH = 7)} \qquad (3.21)$$

Based on a reduction potential of MV^{2+} that is pH independent at -446 mV (Anode), the free energy at room temperature is expected to be 6.2 kJ/mol. The calculated free energy of reaction 3.16 at absolute zero is expected to be 27 kJ/mol, which is significantly larger than the thermodynamic potential of the reaction of 6.2 kJ/mol, and deviates further at higher temperatures (note non-Van't Hoff behavior below 45˚C). This is effectively an over-potential of the reaction catalyzed by the [NiFe] H_2ase as written in equation 3.16. H_2ases bound directly to electrode surfaces show almost no over-potential to the reversible catalytic wave. This indicates that the interaction with MV in solution significantly alters the chemical reaction thermodynamics. This can occur through multiple mechanisms including activity changes of the MV^+ vs. MV^{2+} species in the equilibrium constant that may be overcome by higher ionic strength, or that protein interaction or solvation of MV^{2+} is unfavorable at high temperature. The structural implications of this conclusion could yield information regarding the physiological bias

of these enzymes, particularly by comparing direct adsorption with native redox partner mediated catalytic activity.

3.3 – Conclusions

In this chapter steady state characterization of the proton reduction mechanism of the Pf SHI are presented. Using temperature and pH dependent of the observed kinetics of $H^+(D^+)$ reduction and H/D exchange a model was developed which is consistent with a product release rate determining step and a kinetically competitive intramolecular PT process. This has implications in the field of biomimetic design in which proton and H_2 affinity require a balanced relationship which can facilitate the facile reversible H^+ reduction chemistry. It would be interesting to compare this data to a similar data set for an [FeFe] H_2ase, which typically function in H^+ reduction rather than H_2 oxidation. Here H_2 release may be more favorable leading to drastically different KIE and pH effects.

In addition to determination of the rate determining steps, inhibition studies which probe the active site specifically (CO) and ET chain (S^0) independently were conducted which yielded insight. CO inhibition was shown to be substantial at saturation conditions (64%) and was reversible. Since the CO molecule only binds to the Ni_a-S state, this indicates that CO diffusion is reasonably competitive with the proton coupled reduction rate of this state. S^0 was shown to compete also reversibly with the *Pf* SHI and was shown to not occur at the active site by FTIR analysis of the active site reactions with H_2S and S^0 (polysulfide). This was interpreted as a competitive ET indicating that ET or PT to the S^0 is competitive with H^+ reduction providing a further probe of the directionally of ET flow and rate relative to PT.

Finally, based on steady state kinetic equilibrium studies the temperature dependent bias was shown to be manifested in an increasing endergonic free energy of the H_2 oxidation reaction pushing the bias more towards H_2 oxidation as temperature is increased. A complete physical explanation of this is at this point lacking, but likely is the result of intermolecular interactions which determine the ET thermodynamics which are highly relevant to the *in vivo* function of these enzymes. The presented steady state data still offer unsatisfactory descriptions of the intramolecular PT, ET and active site chemistry. These questions can theoretically be addressed by pre-steady state kinetics. In the subsequent chapters, methods for rapid initiation using light as a reaction initiator are developed to address the pre-steady state kinetics of this enzyme and others.

3.4 - References

(1) Farkas, A.; Farkas, L.; Yudkin, J. *P R Soc Lond B-Conta* **1934**, *115*, 373.

(2) Green, D. E.; Stickland, L. H. *Biochem J* **1934**, *28*, 898.

(3) Stickland, L. H.; Green, D. E. *Nature* **1934**, *133*, 573.

(4) Hoberman, H. D.; Rittenberg, D. *J Biol Chem* **1943**, *147*, 211.

(5) Krasna, A. I.; Rittenberg, D. *J Am Chem Soc* **1954**, *76*, 3015.

(6) Fontecilla-Camps, J. C.; Volbeda, A.; Cavazza, C.; Nicolet, Y. *Chem Rev* **2007**, *107*, 4273.

(7) Vignais, P. M.; Billoud, B. *Chem Rev* **2007**, *107*, 4206.

(8) Hammes-Schiffer, S.; Stuchebrukhov, A. A. *Chem Rev* **2010**, *110*, 6939.

(9) Reece, S. Y.; Nocera, D. G. *Annu Rev Biochem* **2009**, *78*, 673.

(10) Warren, J. J.; Tronic, T. A.; Mayer, J. M. *Chem Rev* **2010**, *110*, 6961.

(11) Weinberg, D. R.; Gagliardi, C. J.; Hull, J. F.; Murphy, C. F.; Kent, C. A.; Westlake, B. C.; Paul, A.; Ess, D. H.; McCafferty, D. G.; Meyer, T. J. *Chem Rev* **2012**, *112*, 4016.

(12) Conway, B. E.; Tilak, B. V. *Electrochim Acta* **2002**, *47*, 3571.

(13) Dempsey, J. L.; Brunschwig, B. S.; Winkler, J. R.; Gray, H. B. *Accounts Chem Res* **2009**, *42*, 1995.

(14) Tard, C.; Pickett, C. J. *Chem Rev* **2009**, *109*, 2245.

(15) Helm, M. L.; Stewart, M. P.; Bullock, R. M.; DuBois, M. R.; DuBois, D. L. *Science* **2011**, *333*, 863.

(16) Camara, J. M.; Rauchfuss, T. B. *Nat Chem* **2012**, *4*, 26.

(17) Weber, K.; Kramer, T.; Shafaat, H. S.; Weyhermuller, T.; Bill, E.; van Gastel, M.; Neese, F.; Lubitz, W. *J Am Chem Soc* **2012**, *134*, 20745.

(18) Kaur-Ghumaan, S.; Stein, M. *Dalton Trans* **2014**.

(19) Trasatti, S. *J Electroanal Chem* **1972**, *39*, 163.

(20) Quaino, P.; Juarez, F.; Santos, E.; Schmickler, W. *Beilstein J Nanotech* **2014**, *5*, 846.

(21) Fontecilla-Camps, J. C.; Amara, P.; Cavazza, C.; Nicolet, Y.; Volbeda, A. *Nature* **2009**, *460*, 814.

(22) Dementin, S.; Burlat, B.; Fourmond, V.; Leroux, F.; Liebgott, P. P.; Abou Hamdan, A.; Leger, C.; Rousset, M.; Guigliarelli, B.; Bertrand, P. *J Am Chem Soc* **2011**, *133*, 10211.

(23) Abou Hamdan, A.; Dementin, S.; Liebgott, P. P.; Gutierrez-Sanz, O.; Richaud, P.; De Lacey, A. L.; Roussett, M.; Bertrand, P.; Cournac, L.; Leger, C. *J Am Chem Soc* **2012**, *134*, 8368.

(24) Pershad, H. R.; Duff, J. L. C.; Heering, H. A.; Duin, E. C.; Albracht, S. P. J.; Armstrong, F. A. *Biochemistry-Us* **1999**, *38*, 8992.

(25) Lamle, S. E.; Albracht, S. P. J.; Armstrong, F. A. *J Am Chem Soc* **2004**, *126*, 14899.

(26) Hexter, S. V.; Grey, F.; Happe, T.; Climent, V.; Armstrong, F. A. *P Natl Acad Sci USA* **2012**, *109*, 18232.

(27) Dementin, S.; Burlat, B.; De Lacey, A. L.; Pardo, A.; Adryanczyk-Perrier, G.; Guigliarelli, B.; Fernandez, V. M.; Rousset, M. *J Biol Chem* **2004**, *279*, 10508.

(28) Vignais, P. M. *Coordin Chem Rev* **2005**, *249*, 1677.

(29) Pandelia, M. E.; Ogata, H.; Lubitz, W. *Chemphyschem* **2010**, *11*, 1127.

(30) Lubitz, W.; Ogata, H.; Rudiger, O.; Reijerse, E. *Chem Rev* **2014**, *114*, 4081.

(31) deLacey, A. L.; Hatchikian, E. C.; Volbeda, A.; Frey, M.; FontecillaCamps, J. C.; Fernandez, V. M. *J Am Chem Soc* **1997**, *119*, 7181.

(32) DeLacey, A. L.; Stadler, C.; Fernandez, V. M.; Hatchikian, E. C.; Fan, H. J.; Li, S. H.; Hall, M. B. *J Biol Inorg Chem* **2002**, *7*, 318.

(33) Fichtner, C.; Laurich, C.; Bothe, E.; Lubitz, W. *Biochemistry-Us* **2006**, *45*, 9706.

(34) De Lacey, A. L.; Fernandez, V. M.; Rousset, M.; Cammack, R. *Chem Rev* **2007**, *107*, 4304.

(35) Lubitz, W.; Reijerse, E.; van Gastel, M. *Chem Rev* **2007**, *107*, 4331.

(36) Tamiya, N.; Miller, S. L. *J Biol Chem* **1963**, *238*, 2194.

(37) Yagi, T.; Tsuda, M.; Inokuchi, H. *J Biochem-Tokyo* **1973**, *73*, 1069.

(38) Mctavish, H.; Sayavedrasoto, L. A.; Arp, D. J. *J Bacteriol* **1995**, *177*, 3960.

(39) Zorin, N. A.; Dimon, B.; Gagnon, J.; Gaillard, J.; Carrier, P.; Vignais, P. M. *Eur J Biochem* **1996**, *241*, 675.

(40) Bertrand, P.; Dole, F.; Asso, M.; Guigliarelli, B. *J Biol Inorg Chem* **2000**, *5*, 682.

(41) Vignais, P. M.; Cournac, L.; Hatchikian, E. C.; Elsen, S.; Serebryakova, L.; Zorin, N.; Dimon, B. *Int J Hydrogen Energ* **2002**, *27*, 1441.

(42) Gest, H. *Bacteriol Rev* **1954**, *18*, 43.

(43) Peck, H. D.; Gest, H. *J Bacteriol* **1956**, *71*, 70.

(44) Armstrong, F. A.; Heering, H. A.; Hirst, J. *Chem Soc Rev* **1997**, *26*, 169.

(45) Jones, A. K.; Lamle, S. E.; Pershad, H. R.; Vincent, K. A.; Albracht, S. P. J.; Armstrong, F. A. *J Am Chem Soc* **2003**, *125*, 8505.

(46) Armstrong, F. A.; Belsey, N. A.; Cracknell, J. A.; Goldet, G.; Parkin, A.; Reisner, E.; Vincent, K. A.; Wait, A. F. *Chem Soc Rev* **2009**, *38*, 36.

(47) Lamle, S. E.; Albracht, S. P. J.; Armstrong, F. A. *J Am Chem Soc* **2005**, *127*, 6595.

(48) Abou Hamdan, A.; Burlat, B.; Gutierrez-Sanz, O.; Liebgott, P. P.; Baffert, C.; De Lacey, A. L.; Rousset, M.; Guigliarelli, B.; Leger, C.; Dementin, S. *Nat Chem Biol* **2013**, *9*, 15.

(49) Bryant, F. O.; Adams, M. W. W. *J Biol Chem* **1989**, *264*, 5070.

(50) Dementin, S.; Leroux, F.; Cournac, L.; de Lacey, A. L.; Volbeda, A.; Leger, C.; Burlat, B.; Martinez, N.; Champ, S.; Martin, L.; Sanganas, O.; Haumann, M.;

Fernandez, V. M.; Guigliarelli, B.; Fontecilla-Camps, J. C.; Rousset, M. *J Am Chem Soc* **2009**, *131*, 10156.

(51) McTavish, H.; SayavedraSoto, L. A.; Arp, D. J. *BBA-Protein Struct M* **1996**, *1294*, 183.

(52) Shafaat, H. S.; Rudiger, O.; Ogata, H.; Lubitz, W. *BBA-Bioenergetics* **2013**, *1827*, 986.

(53) Lubitz, W. *J Biol Inorg Chem* **2014**, *19*, S99.

(54) Laidler, K. J. *Chemical Kinetics*; Third ed.; Harper & Row, Publishers, Inc.: New York, NY, 1987.

(55) Volbeda, A.; Charon, M. H.; Piras, C.; Hatchikian, E. C.; Frey, M.; Fontecillacamps, J. C. *Nature* **1995**, *373*, 580.

(56) Volbeda, A.; Garcin, E.; Piras, C.; deLacey, A. L.; Fernandez, V. M.; Hatchikian, E. C.; Frey, M.; FontecillaCamps, J. C. *J Am Chem Soc* **1996**, *118*, 12989.

(57) Montet, Y.; Amara, P.; Volbeda, A.; Vernede, X.; Hatchikian, E. C.; Field, M. J.; Frey, M.; FontecillaCamps, J. C. *Nat Struct Biol* **1997**, *4*, 523.

(58) Garcin, E.; Vernede, X.; Hatchikian, E. C.; Volbeda, A.; Frey, M.; Fontecilla-Camps, J. C. *Structure* **1999**, *7*, 557.

(59) Vitt, S.; Ma, K.; Warkentin, E.; Moll, J.; Pierik, A. J.; Shima, S.; Ermler, U. *J Mol Biol* **2014**, *426*, 2813.

(60) Cha, Y.; Murray, C. J.; Klinman, J. P. *Science* **1989**, *243*, 1325.

(61) Glickman, M. H.; Klinman, J. P. *Biochemistry-Us* **1996**, *35*, 12882.

(62) Knapp, M. J.; Rickert, K.; Klinman, J. P. *J Am Chem Soc* **2002**, *124*, 3865.

(63) Westheimer, F. H. *Chem Rev* **1961**, *61*, 265.

(64) van Haaster, D. J.; Silva, P. J.; Hagedoorn, P. L.; Jongejan, J. A.; Hagen, W. R. *J Bacteriol* **2008**, *190*, 1584.

(65) Lill, S. O. N.; Siegbahn, P. E. M. *Biochemistry-Us* **2009**, *48*, 1056.

(66) Krasna, A. I.; Rittenberg, D. *P Natl Acad Sci USA* **1954**, *40*, 225.

(67) Purec, L.; Krasna, A. I.; Rittenberg, D. *Biochemistry-Us* **1962**, *1*, 270.

(68) George, S. J.; Kurkin, S.; Thorneley, R. N. F.; Albracht, S. P. J. *Biochemistry-Us* **2004**, *43*, 6808.

(69) Hallahan, D. L.; Fernandez, V. M.; Hatchikian, E. C.; Hall, D. O. *Biochimie* **1986**, *68*, 49.

(70) Purec, L.; Krasna, A. I.; Rittenberg, D. *Biochemistry-Us* **1962**, *1*, 270.

(71) Fauque, G.; Berlier, Y.; Choi, E. S.; Peck, H. D.; Legall, J.; Lespinat, P. A. *Biochem Soc T* **1987**, *15*, 1050.

(72) Ogata, H.; Mizoguchi, Y.; Mizuno, N.; Miki, K.; Adachi, S.; Yasuoka, N.; Yagi, T.; Yamauchi, O.; Hirota, S.; Higuchi, Y. *J Am Chem Soc* **2002**, *124*, 11628.

(73) Ludwig, M.; Cracknell, J. A.; Vincent, K. A.; Armstrong, F. A.; Lenz, O. *J Biol Chem* **2009**, *284*, 465.

(74) Fritsch, J.; Lenz, O.; Friedrich, B. *Nat Rev Microbiol* **2013**, *11*, 106.

(75) Kubas, G. J. *Chem Rev* **2007**, *107*, 4152.

(76) Stein, M.; Lubitz, W. *Phys Chem Chem Phys* **2001**, *3*, 2668.

(77) Stein, M.; van Lenthe, E.; Baerends, E. J.; Lubitz, W. *J Am Chem Soc* **2001**, *123*, 5839.

(78) Vanderzwaan, J. W.; Coremans, J. M. C. C.; Bouwens, E. C. M.; Albracht, S. P. J. *Biochim Biophys Acta* **1990**, *1041*, 101.

(79) Adams, M. W. W. *FEMS Microbiol Lett* **1990**, *75*, 219.

(80) Adams, M. W. W. *Adv Inorg Chem Rad* **1992**, *38*, 341.

(81) Stein, M.; Lubitz, W. *J Inorg Biochem* **2004**, *98*, 862.

(82) Pardo, A.; De Lacey, A. L.; Fernandez, V. M.; Fan, H. J.; Fan, Y.; Hall, M. B. *J Biol Inorg Chem* **2006**, *11*, 286.

(83) Siegbahn, P. E.; Tye, J. W.; Hall, M. B. *Chem Rev* **2007**, *107*, 4414.

(84) Weber, K.; Weyhermuller, T.; Bill, E.; Lubitz, W. *J Biol Inorg Chem* **2014**, *19*, S425.

(85) Fontecilla-Camps, J. C.; Volbeda, A.; Cavazza, C.; Nicolet, Y. *Chem Rev* **2007**, *107*, 4273.

(86) Mulder, D. W.; Shepard, E. M.; Meuser, J. E.; Joshi, N.; King, P. W.; Posewitz, M. C.; Broderick, J. B.; Peters, J. W. *Structure* **2011**, *19*, 1038.

(87) Lubitz, W.; Ogata, H.; Rudiger, O.; Reijerse, E. *Chem Rev* **2014**, *114*, 4081.

(88) Ma, K.; Schicho, R. N.; Kelly, R. M.; Adams, M. W. W. *P Natl Acad Sci USA* **1993**, *90*, 5341.

(89) Arendsen, A. F.; Veenhuizen, P. T. M.; Hagen, W. R. *FEBS Lett* **1995**, *368*, 117.

(90) Vincent, K. A.; Parkin, A.; Armstrong, F. A. *Chem Rev* **2007**, *107*, 4366.

Chapter 4

Photo-Chemical Methods for Rapid Initiation of Proton Reduction by H_2ase Enzymes

Abstract: Experimental limitations in both traditional enzymology techniques as well as rapid mixing approaches to pre-steady state initiation have inhibited the investigation of the mechanism of the hydrogenase (H_2ase) enzymes due to their rapid reactivity. In this chapter, a survey of photo-chemical initiation methods are investigated with an emphasis on systems with potential to initiate the reductive reactivity of H_2ase enzymes with sufficient time resolution to explore reactivity beyond the rate determining step. To this end, photo-initiated electron transfer (ET) was investigated from a dye molecule (Tris(bipyridine) ruthenium(II) [$Ru(bpy)_3^{2+}$]) as well as mercaptoacid stabilized semiconductor nanoparticles. $Ru(bpy)_3^{2+}$ based photo-sensitization was observed, but efficiencies were low attributed to non-specific ET interactions. CdTe quantum dot photo-sensitization was highly efficient with 4% internal quantum efficiency and revealed drastically different photo-reduction properties as determined by light titration FTIR difference spectroscopy. The differences in dye and nanoparticle sensitization were attributed to electron delivery rate to the enzyme indicating different modalities of catalysis under various electron flux conditions. These results were further compared to photo-ionization of NADH, an irreversible photo-initiator. While the CdTe quantum dots performed ideally for bulk measurements, stability and optical density mismatch issues indicate the NADH photo-ionization to be a more plausible methodology for transient spectroscopic investigations.

4.1 Introduction

Enzymes are peptide based biopolymers that facilitate catalysis of biologically relevant reactions with high specificity and efficiency. Their function and mechanism of action has been the subject of extensive research for over a century, but still fundamental

questions remain.[1-6] The lack of consensus on enzymes function has often been a direct result of experimental challenges in investigating enzymatic processes on their relevant timescales.[7-11] Enzymes often coordinate multiple chemical steps including substrate binding and product release to achieve a target chemical transformation at rate from 10^{-2} to 10^{7} s^{-1}. These rates for overall catalysis (k_{cat}) necessitate the elementary processes involved in the chemical reactions (such as hydride transfer, electron transfer, proton transfer and protein conformational dynamics) to be faster. This presents an implicit experimental challenge for analysis of enzymatic reaction mechanisms, where both the reaction initiation and the analytical detection methodology must have sufficient temporal resolution to observe chemical changes before the reaction has completed. The difficulty of studying enzymatic reaction mechanisms on their relevant timescale is exemplified by the hydrogenases (H_2ases), enzymes that reversibly convert protons and electrons to H_2 with turnover frequencies of 10,000 s^{-1} or greater.[12-20] In these enzymes, complete turnover is often achieved within a hundred microseconds, which necessitates the transport of two electrons and two protons over long distances within the enzyme on shorter timescales. Since proton motion in proteins is inherently difficult to probe and the redox active cofactors do not have strong spectroscopic signatures the mechanism of these enzymes has been difficult to probe.

To rapidly initiate reactions with enzymes numerous methodological advances have emerged.[10,11,21-29] Rapidly initiating enzyme reactions by rapid mixing, thermodynamic perturbations and photo-release of reactants have been established as techniques to push the reaction initiation timescale past bulk turnover rates. Rapid mixing methods have been advanced substantially and can readily achieve time resolutions of

<100 μs, but typically rely on intrinsic or extrinsic chromophores to achieve sub-millisecond timescales.[30-33] These mixing technologies are not amenable to the study of numerous enzymatic systems including H_2ases for which cofactors or substrates are not good chromophore candidates. Specifically in the H_2ases the iron sulfur clusters and active site display poor optical characteristics for spectroscopic investigation with respect to their low absorption cross sections which do not respond significantly to redox changes.[34-36]

Rapid thermodynamic perturbations such as temperature and pressure jump methods can achieve very high time resolution (ps-ns), but require systems to have equilibrium constants that are temperature/pressure dependent and near unity.[8,10,28] Photo-release (or photolysis) of "caged" reactants achieves the advantages of both the aforementioned techniques by generating large equilibrium displacements for reactions with equilibrium constants far away from unity with time resolutions limited by photo-chemical release (ps-ns).[29,37-41] Numerous examples in the literature have used these techniques to study fast reactions by photolysis of electrons, protons, O_2 and even ATP.[8,10,29,37,39-42] Of all the caged reagents for photo-chemical release, photolysis of electrons is the most broadly applicable technique for two reasons; redox chemistry often overlaps with O_2, proton and metal reactivity and photolysis driven reduction is not constrained by buffering or saturation issues as H^+ and O_2 photo-chemical release are. While photo-reduction has been used extensively to study charge transport phenomenon in redox metallo-proteins such as azurins and cytochromes, it has been less exploited for interrogating chemical mechanisms in enzymes.[38,42-47]

In this chapter, photo-chemical methods for driving photo-catalysis of [NiFe] H_2ases are developed based on small molecule (NADH and $Ru(bpy)_3$) as well as semiconductor nano-particle (CdTe and CdSe@CdS dot in rod structures) photo-sensitizers. The different photo-reductant modules are compared with respect to efficiency, mechanism of action and utility in mechanisitic investigations on H_2ase reductive activity.

4.2 Results and Discussion

To investigate potential molecular photo-reductants for rapid initiation of H_2ase activity three critical criteria need be met; (1) the molecular photo-sensitizer needs to facilitate reduction of the enzyme which is functional in driving catalysis, (2) the photo-sensitizer need to reduce the enzyme with a rate that is competitive or faster than the overall TOF of the enzyme and (3) the photo-sensitizer needs to reduce the enzyme with internal quantum yields appreciable enough to generate substantial changes in enzyme populations with a single laser flash for applications in time resolved spectroscopy. As a baseline test, tris(bipyridine)ruthenium(II) chloride (Ru(bpy)) was used as a dye sensitizer for photo-chemical H_2ase reduction, which operates by direct ET or reductive quenching depending on conditions.

4.2.1 Tris(bipyridine)ruthenium(II) photo-sensitization

Ru(bpy) proved to be an excellent model system for investigation of proton reduction by the [NiFe] H_2ase from *Thiocapsa roseopersicina* (*Tr*), a "standard" class I [NiFe] H_2ase. Although no crystallographic structure of the Tr H_2ase has been reported,

numerous steady state kinetic data have been reported and the amino acid sequence is over 50% similar to other crystalized class I [NiFe] H_2ases.[48-50] To investigate intermolecular ET the steady state and transient photoluminescence (PL) was measured in D_2O pD 6.6 in the absence and presence of the *Tr* H_2ase and is shown in Fig. 4.1. The steady state photoluminescence is sensitive to the overall QY as described in equation 1 and the transient photoluminescence is sensitive to the component lifetimes as described in equations 2;

$$QY = \frac{k_{RR}}{k_{RR}+k_{NR}} \qquad (1)$$

$$I(t) = I_0 * e^{-t\cdot(k_{RR}+k_{NR})} \qquad (2)$$

where k_{RR} is the rate of radiative excited state relaxation, k_{NR} is the rate of non-radiative excited state relaxation (which includes electron transfer or reductive/oxidative quenching as well as energy dissipation in heat or inner system crossing) and I_0 is the initial fluorescence intensity. In steady state PL titrations with 10 µM Ru(bpy) was quenched 9% with a twofold excess of *Tr* H_2ase. This quenching was observed without a sacrificial electron donor, but was not changed substantially due to the poor reductive quenching efficiency of the ascorbate donor relative to ascorbic acid. The trend was linear up to fourfold excess which indicates a non-static complex probably governed by diffusion or a very weak association. Diffusion models for contact initiated ET are well established for small molecules, but less developed for complex protein systems, where the protein cannot be treated as a sphere of equal radial contact probability for ET. Instead the majority of the protein surface is redox inactive, and only very small portions of the surface are functional in collision based ET. The photoluminescence lifetime was

measured to be 1.2 µs without the enzyme present, and with a twofold excess decreased to 1.1 µs consistent with the steady state results.

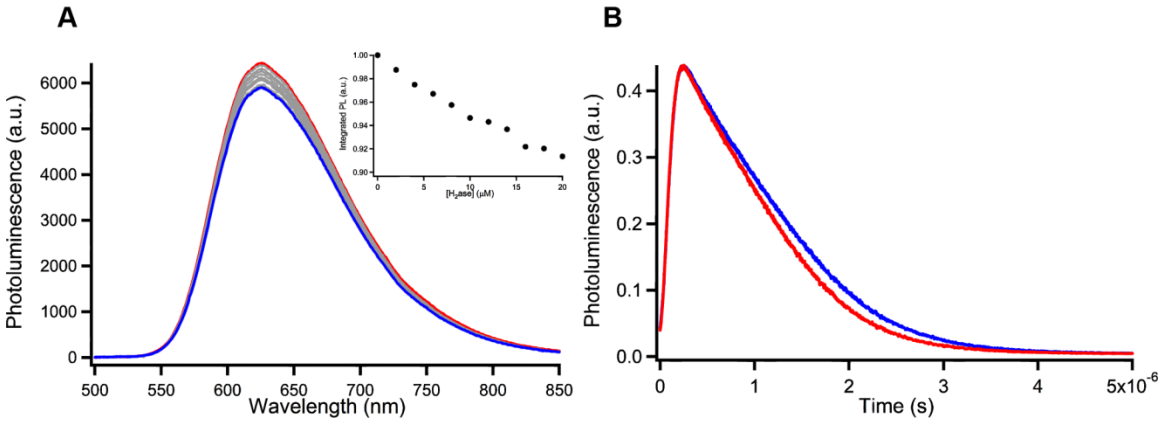

Figure 4.1 – Steady state and time resolved photoluminescence quenching of Ru(bpy) in the presence of *Tr* H_2ase. (A) Steady state photoluminescence quenching of 10 µM Ru(bpy) by various concentrations of H_2ase (red represents no H_2ase, blue represents 20 µM H_2ase in steps of 2 µM H_2ase. Inset shows integrated peak area as a function of H_2ase concentration. (B) Time resolved photoluminescence quenching of Ru(bpy) with (red) and without (blue) 20 µM H_2ase.

The small observed quenching efficiency in the steady state and transient photoluminescence implies a low quantum efficiency of ET and thus proton reduction by the *Tr* H_2ase. To examine this, H_2 production was quantified for a solution of 10 mM Ru(bpy), 1 µM H_2ase and 100 mM Ascorbate as a sacrificial electron donor in 100 mM phosphate buffer pD = 6.6. The system produced H_2 consistently for over two hours with a final turnover number (TON) of 140, but the quantum yield (QY) was 0.02%. This was quite low and consistent with the transient and steady state PL data, where the QY of PL is 4% and less than 10% quenching was observed of the PL signal. The PL data is not

sensitive to back ET which likely accounts for the difference in apparent ET yield vs. internal quantum yield.

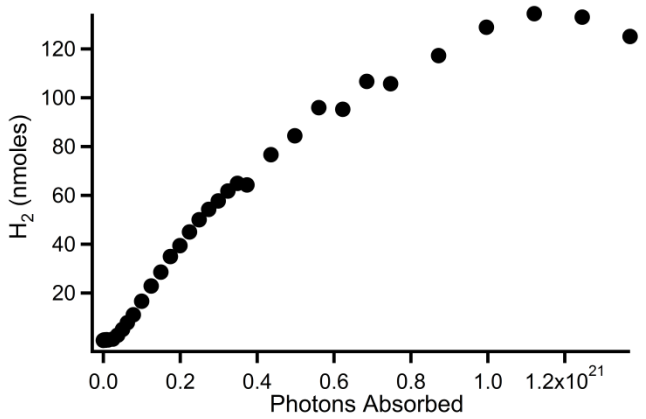

Figure 4.2 – Photo-catalytic H_2 production by Ru(bpy) H_2ase system. H_2 production as measured by gas chromatography from 10 µM *Tr* H_2ase by excitation of 40 µM Ru(bpy) with 100 mW of 527 nm light from a actively Q-switched Nd:YAG laser (Crystalaser) operating at 4 kHz repetition rate with 7ns pulse width.

Additionally, light titration FTIR spectra were collected to determine the potential for mechanistic investigations. Using 527 nm excitation the oxidized Tr H_2ase could be photo-reduced by Ru(bpy) producing a distribution of reduced states in the infrared spectrum. Based on steady state characterization and comparison with other [NiFe] H_2ases, the Ni_r-B (νCO 1944 cm^{-1}) and Ni_a-S (1931 cm^{-1}) states were observed to bleach with concomitant formation of the Ni_r-S (1915 cm^{-1}), Ni_a-C (1951 cm^{-1}), Ni_a-SR (1922 cm^{-1}) and Ni-L (1900 cm^{-1}) states. Despite the obvious observation of reduced states upon illumination, the overall quantum yield and lifetime shortening indicate only a very small

fraction of H_2ase is being reduced on a per pulse basis that would be amenable to time resolved spectroscopy.

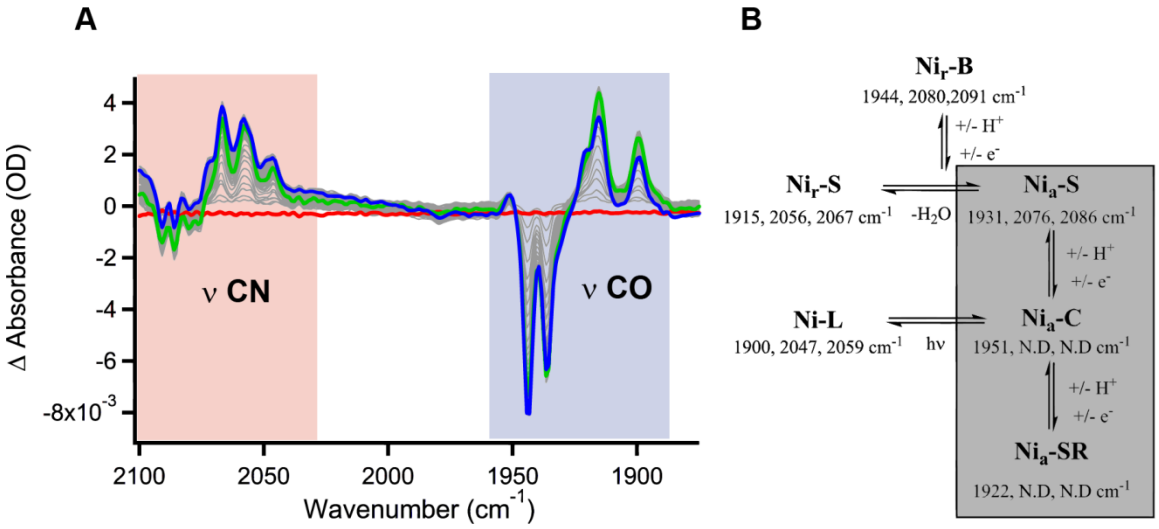

Figure 4.3 – FTIR light titration difference spectra of Ru(bpy)-H_2ase system. A) FTIR light titration difference spectra of Ru(bpy)-H_2ase system under 527 nm illumination and state diagram with associated infrared CO and CN absorbance band positions. The red spectrum represents the dark difference spectrum, green represents the spectrum after 3 seconds of illumination, and blue represents the spectrum after 12 seconds of illumination (grey lines are spectra recorded after successive 100 ms exposures controlled by an optical shutter). B) Various steady states in the catalytic cycle of the H_2ase are labeled. The dark raw absorbance spectrum is shown in black vs. the right ordinate. State diagram describes standard [NiFe] H_2ase steady states and their reactivity. Grey box indicates proposed catalytic states.

4.2.2 CdTe Quantum Dot Photo-Sensitization

Another approach using CdTe semiconductor nanoparticles for photo-reduction of the H_2ase was explored for potential applications in rapid photo-reduction. Here the negatively charged MPA capped CdTe nanoparticle is hypothesized to bind to a positive patch on the enzyme located near the distal FeS cluster which is advantageous for intermolecular ET. Using photo-luminescence quenching, the binding of the H_2ase to MPA capped CdTe quantum dots (diameter = 3.5 nm) was examined. Using analogous experimental characterization techniques the photo-luminescence quenching was examined to determine the quantum efficiency of ET and is shown in Figure 4.4. Based on an initial quantum yield of 10% as determined relative to a rhodamine standard, a quenching of ~45% was achieved with a 4:1 excess of H_2ase to QDs. This implies a quantum yield of ET of approximately 4-5% which is comparable to that observed by others.

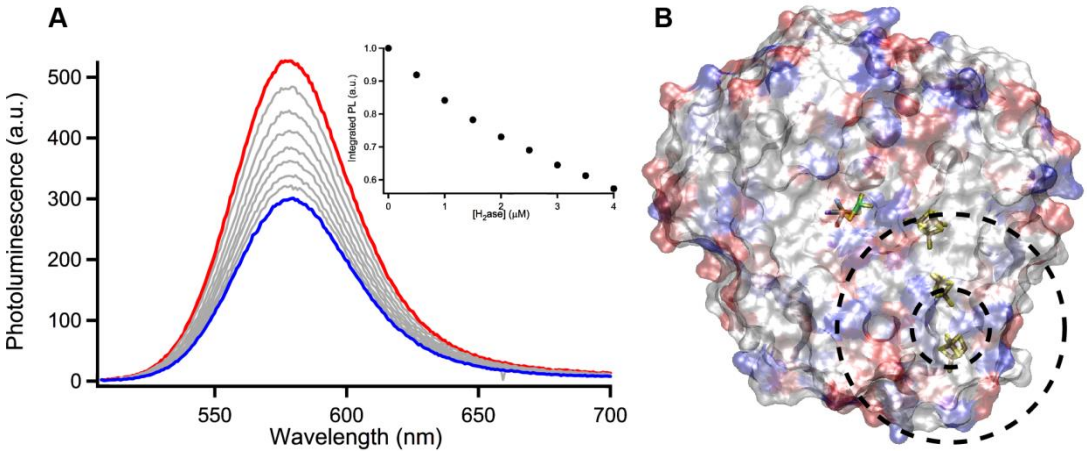

Figure 4.4 – Photoluminescence quenching of CdTe quantum dots upon H_2ase addition. A) Photoluminescence spectra of 1 μM CdTe quantum dots (excitation at 500 nm) alone (red) and with varying concentrations of *Tr* H_2ase (grey) to a final concentration of 4 μM H_2ase (blue). Inset shows integrated concentration dependence of PL quenching. B)

Surface charge density distribution and potential anionic CdTe quantum dot binding region based on the homology modeled structure of the *Tr* H_2ase from the *D. gigas* crystal structure.

The photo-catalytic proton reduction efficiency of the H_2ase-CdTe quantum dot assemblies was examined under similar conditions with ascorbate as a sacrificial electron donor and is shown below in Fig. 4.5. Using gas chromatography the light dependent H_2 production was examined and an internal quantum yield of H_2 production was determined to be 4% (excitons generated relative to electrons stored in H_2), consistent with the PL quenching data. This QY is also comparable to other reports in the literature of H_2ase-nanoparticle assemblies based on electrostatic affinity. The system produced with a TON of 92, slightly lower than the $Ru(bpy)_3$ system, which was attributed to photo-decomposition of the CdTe quantum dots by ligand oxidation. This was clearly observed as a red precipitate after long exposures, temporally consistent with the H_2 production leveling off. At high salt concentration H_2 production was observed (data not shown) albeit at a significantly diminished rate indicating lower binding affinity due to salt screening.

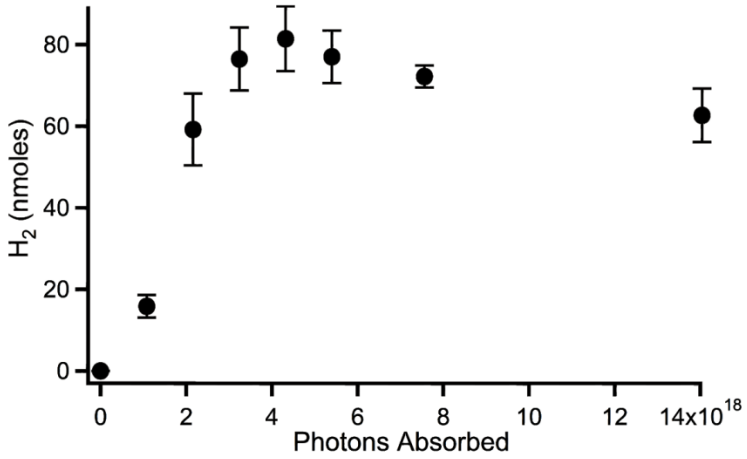

Figure 4.5 – Photo-catalytic H_2 production by CdTe quantum dot-H_2ase system. Photo-catalytic H_2 production from 4:1 complex of H_2ase-CdTe quantum dots by excitation with 100 mW of 527 nm light from a actively Q-switched Nd:YAG laser (Crystalaser) operating at 4 kHz repetition rate with 7ns pulse width. Concentrations of H_2ase and QDs were 4 and 1 μM respectively.

Again, analogously light titrations were performed to examine the potential for applications in fast mechanistic investigation experiments and are shown in Fig. 4.6. These data show photo-reduction of the enzyme, but yielded remarkably different results relative to the $Ru(bpy)_3$ experiments. The clearest result is that only the bleaching of Ni_r-B (1944 cm^{-1}) with concomitant formation of Ni_a-S (1931 cm^{-1}) is observed in the equilibrium light titration when QDs were used rather than $Ru(bpy)_3$. We believe this is due to the greatly enhanced rate of electron flux in these systems due to the large quantum yield of ET and catalysis. Additionally, the sacrificial electron donor could be monitored by this method in the conversion from ascrobate to dehydroascorbate by FTIR. The relative rate of dehydroascorbate/ascorbate conversion relative to Ni_r-B-Ni_a-S conversion is plotted in Figure 4.6B and shows a 2.6 fold larger rate of consumption of

ascorbate relative to formation of reduced hydrogenase. This indicates that the overall process observed in the steady state actually represents a full three electron reduction of the *Tr* [NiFe] H_2ase followed by subsequent turnover to regenerate the Ni_a-S state.

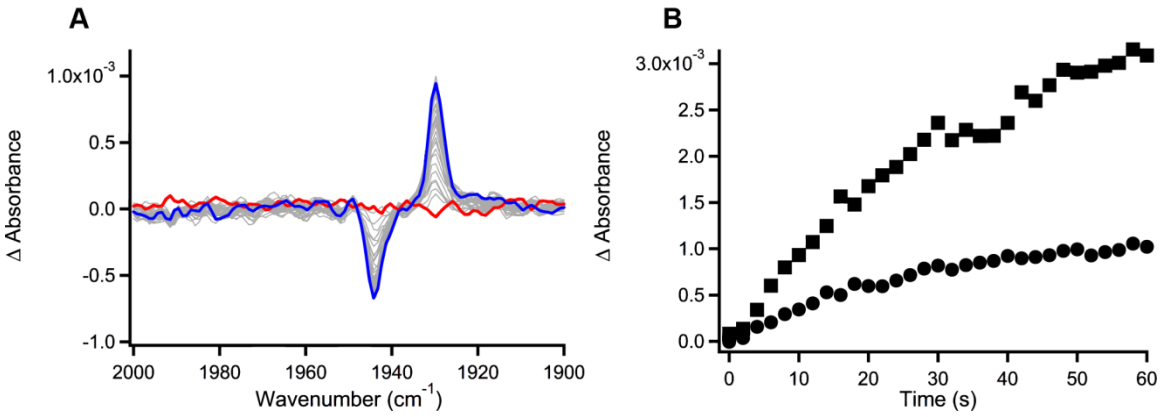

Figure 4.6 - FTIR light titrations of CdTe quantum dot-H_2ase assemblies. A) FTIR spectra as a function of illumination. Red represents the resting dark difference spectrum, and blue represents after 60 seconds of illumination. Data collected every 100 ms of laser exposure controlled by an optical shutter. B) Peak-to-peak difference for Ni_r-B to Ni_a-S (circles) and ascorbate to dehydroascorbate (squares).

The key differences between the QD and $Ru(bpy)_3$ photo-driven enzyme reduction and photo-catalysis can be summarized as follows: First, QD binding is electrostatic, is screened at high salt concentrations, and quenches QD PL, whereas $Ru(bpy)_3$ is nonspecifically bound or bound in ET-inactive sites on the enzyme surface, as determined by homology modeling and PL titrations. Second, H_2 production with QD−H_2ase hybrids is reasonably efficient, whereas $Ru(bpy)_3$ is 100 times less efficient per

photon absorbed. Finally, light-induced difference FTIR measurements showed very different populations of intermediate states. Photo-reduction with QDs resulted in the formation of the Ni_a-S state only, whereas $Ru(bpy)_3$ generated all of the known steady-state intermediates. These are fundamentally different end points in photo-reduction, and the $Ru(bpy)_3$ spectra did not evolve to the QD−H_2ase spectra at long illumination times. The accumulation of a distribution of intermediates is correlated with inefficient enzyme turnover. The origins of the differences in the light titration results are not completely understood but certainly have to do with the fundamental differences between $Ru(bpy)_3$ and QD photosensitizers. One possible explanation is that the observed differences are purely a consequence of the mode of photosensitizer binding.

Homology modeling suggested that positively charged $Ru(bpy)_3$ may bind non-preferentially for ET. This non-optimally bound photo-sensitizer could make the observation of intermediates more likely since the fundamental reduction events are slower. The mode of binding may also influence the flux of electrons entering the enzyme through the FeS chain versus a more direct route, which in turn could influence the turnover, for example by modulating the efficiency of coupled proton transfers. Finally, QDs may be capable of delivering multiple electrons from multiple absorption and exciton dissociation (ET) processes without requiring hole filling. In contrast, $Ru(bpy)_3$ can deliver only a single electron and then must be regenerated by the SED (no faster than bimolecular diffusion). Thus, QDs may produce multiple reducing equivalents on a time scale that is fast relative to the turnover frequency of the enzyme. This observation raises the possibility that efficient turnover requires fast multi-electron reduction and that the partially reduced steady-state intermediates are a consequence of

slow single-electron reduction and are not productive. Further experiments will be required to determine the source of the observed differences.

4.2.3 On Nanoparticle-Enzyme Orientation Effects.

Unlike the $Ru(bpy)_3$ photo-catalytic system, protein orientation with respect to the the nanocrystal surface is critical to facilitate ET. Additionally, in the standard class I H_2ases contain a single ET active site exposed to the protein surface, whereas other H_2ases contain multiple sites of electron exchange with the protein surface.[15] To investigate orientation effects on nanoparticle-H_2ase conjugation the heterotetrameric soluble type 3 [NiFe] H_2ase from *Pyrococcus furiosus* was employed to examine interaction behavior with CdSe@CdS dot in rod nanorod structures (NRs).[51] This enzyme was an advantageous model system for investigating protein binding motifs due to the development of multiple histidine tags appended to the C-terminus of different enzyme subunits that are thought to function differently with electron carrier redox partners described in Fig. 4.7.[52] Since no crystal structure has been solved for this H_2ase, the surface electrostatic environment is largely unknown. To circumvent this limitation, the cadmium affinity of the histidine tag was utilized to specifically immobilize the enzyme on the nanoparticle surface. His tags have been shown to facilitate protein binding to nanoparticle surfaces of varying composition with binding constants from pM to μM.[53-57] By examining the ET efficiency and H_2 production capacity for various his-tagged-NR hybrid constructs, structural and functional aspects of the H_2ase could be determined.

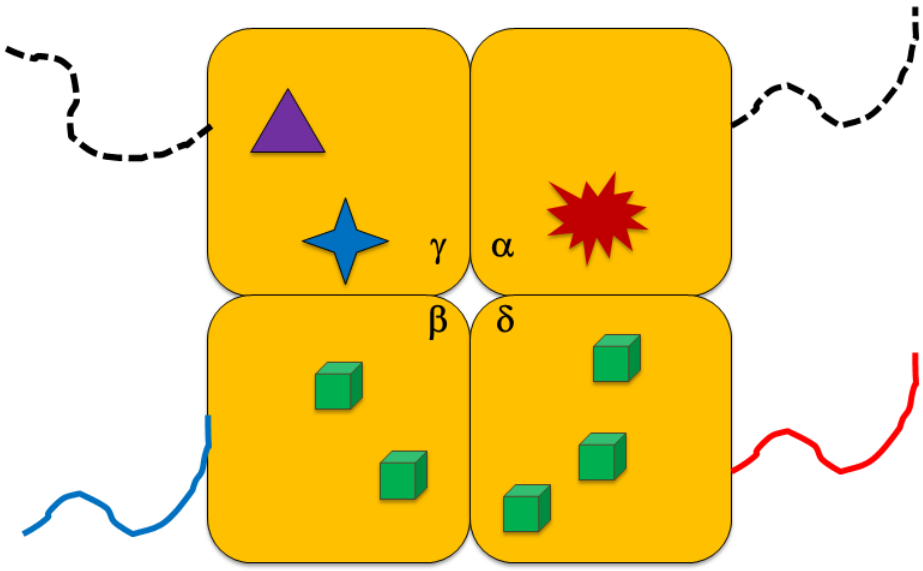

Figure 4.7 – Schematic representation of the *Pf* SHI with the two different his tag locations used in this study (δ and β subunits). Subunits cofactors are represented as follows; Flavin adenine dinucleotide (FAD) as a purple triangle, Fe_2S_2 cluster as a blue star, Fe_4S_4 as green cubes and the [NiFe] active site as a maroon comic explosion.

The two His tags explored here were incorporated into the delta and beta subunits (Fig. 4.7). The delta subunit resembles the standard class 1 H_2ase small subunit, a small domain (~40kDa) that contains three Fe_4S_4 clusters that have been shown in other class III H_2ases to form the ET chain to the active site.[58-61] The solvent exposed C-terminus should thus bind a NR in an orientation that may facilitate electron transfer and subsequent catalysis. The redox potential of Fe_4S_4 clusters in proteins has been typically observed between -0.3 to -0.5 V. In the so called standard H_2ases, the reduction potential has been measured by protein film voltammetry to be -310 mV, thus the clusters are in thermodynamic equilibrium with the H_2 couple and can thus drive catalysis by loading

electrons in from this location.[20,62,63] The second his-tag location was selected on the C terminus of the beta subunit, which also contains two cubane FeS clusters, the function of which is presently unknown.[51,64] Binding of the NRs to either subunit is expected to result in some ET activity, but the internal electronic communication may be different with the various subunits relative to the catalytic subunit α. Thus the nanoparticle functionalization may act as a surface probe to the electronic communication within the clusters.

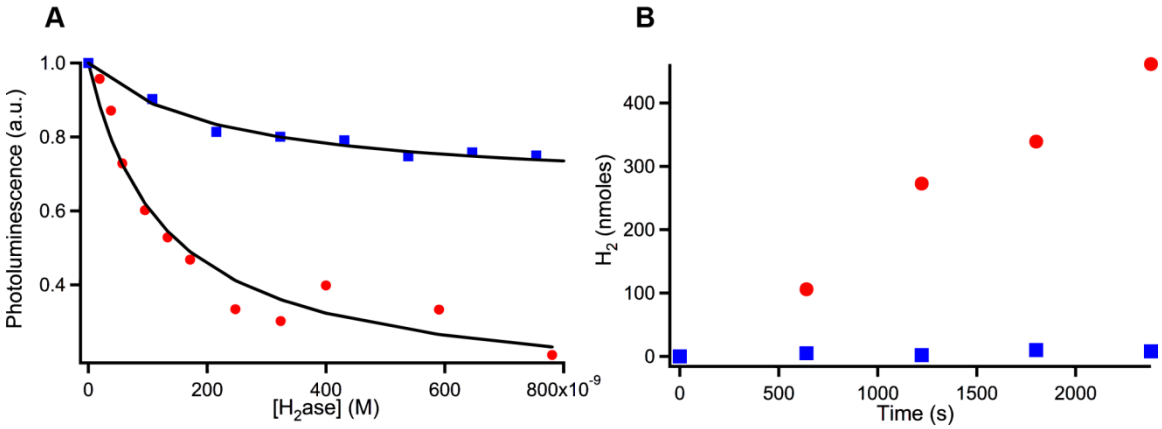

Figure 4.8 – Binding and H_2 production from CdSe@CdS quantum dot bound to β- and δ-His9x tagged *Pf* SHI. A) Photoluminescence quenching of CdSe@CdS quantum dot in rods with β- (blue) or δ-tagged *Pf* SHI (red). B) H_2 production of hybrid nanorod-H_2ase assemblies with β- (blue) or δ-tagged *Pf* SHI (red).

The photoluminescence quenching and Langmuir isotherm for H_2ase-NR assembly are shown in Fig. 4.8A. The addition of stoichiometric amounts of β-tagged SHI to the CdSe@CdS dot in rod structures revealed an approximate 20% quenching efficiency of the PL efficiency, whereas the δ-tagged SHI resulted in significantly

stronger PL quenching at >70%. Assuming that a binding event results in a specific interaction and that only one binding event occurs at these low concentrations the photoluminescence quenching could be fit to a Langmuir relationship described by equation 3 below;

$$\Delta I = 1 - \frac{\Delta I_{max} \cdot K_L \cdot [H_2ase]}{1 - K_L \cdot [H_2ase]} \qquad (3)$$

where ΔI is the normalized photoluminescence quenching, ΔI_{max} is the maximum observed photoluminescence quenching, K_L is the Langmuir constant and [H_2ase] is the H_2ase concentration. Fitting the photoluminescence curve to the above relationship produces a Langmuir constant of 2.2 ± 0.5 * 10^7 M^{-1} for the β-tagged SHI and 1.0 ± 0.1 * 10^7 M^{-1}, a similar effective binding constant of the complexes. This is consistent with various values for His tagged proteins which interact with cadmium based quantum dots and the identical nature of the tags for both subunits. The small difference may be due to the solvent exposure of the C-terminal tag. Non-His tagged H_2ase exhibited <10% quenching efficiency at these concentrations indicating that the histidine tag was indeed responsible for the binding interaction observed in these experiments. Despite an efficient binding constant and PL quenching for the β-tagged construct this hybrid was incapable of performing photo-catalysis. On the other hand, the δ-tagged SHI did exhibit photo-catalytic behavior with a turnover number of 625 over 40 minutes of illumination resulting in a TOF of 0.3 s^{-1}, 0.5% of the native enzyme and an internal quantum yield of approximately 2%.

4.2.4 – NADH Photoionization

As a final comparison, NADH photo-ionization was examined as an example of an irreversible photo-reductant that functions in the absence of a sacrificial electron donor. Here unlike Ru(bpy) and QD photo-sensitizers, the photo-ionization process occurs within picoseconds and is capable of generating two highly reducing species, a solvated electron (-2.6 V vs. NHE) and the $NADH^{+\bullet}$ (-1.9 V vs. NHE) both of which need to diffuse to react with the enzyme.[66,67] The potential benefits of this method are inherent to the irreversibility of the process, thus competition between excited state decay processes are avoided at the expense of high initial photon flux. For these experiments, again the soluble hydrogenase (SHI) from *Pyrococcus furiosus* was used as the H_2ase model system.

Two photon excitation of NADH by 351 nm laser excitation was capable of photo-catalytically driving the SHI as shown in Figure 4.9 A, but seemed to also degrade the enzyme over short periods of time. By using a functional redox mediator such as methyl viologen (MV) the internal QY was enhanced greatly and the enzyme gave a TON of 12,000 and a TOF of 6 s^{-1} despite the high fluence UV laser excitation. The observed TOF is only 10% of the maximal enzymatic turnover (see Chapter 3) which is interesting and unprecedented in most photo-catalytic systems. This is likely a result of the slow turnover of this enzyme at room temperature (62 s^{-1}) and the buildup of substantial MV^+ in the vessel during the initial portion of the experiment. Additionally, UV-Vis spectra were collected to monitor the reaction progress and are also shown in Figure 4.9 B. From the spectra it is clear that methyl viologen was generated and acted as a functional intermediate in the photo-catalytic process. Based on a simple model for two photon efficiency based on the excited state lifetime of the NADH molecule (400 ps) the

pulse width of the Nd:YLF laser used (7 ns) and an assumption that the excited state extinction coefficient doesn't change significantly from the ground state an internal quantum yield can be calculated to be 0.1%, which is quite low, but is likely a lower limit on the photo-reduction quantum yield in a single pulse experiment.

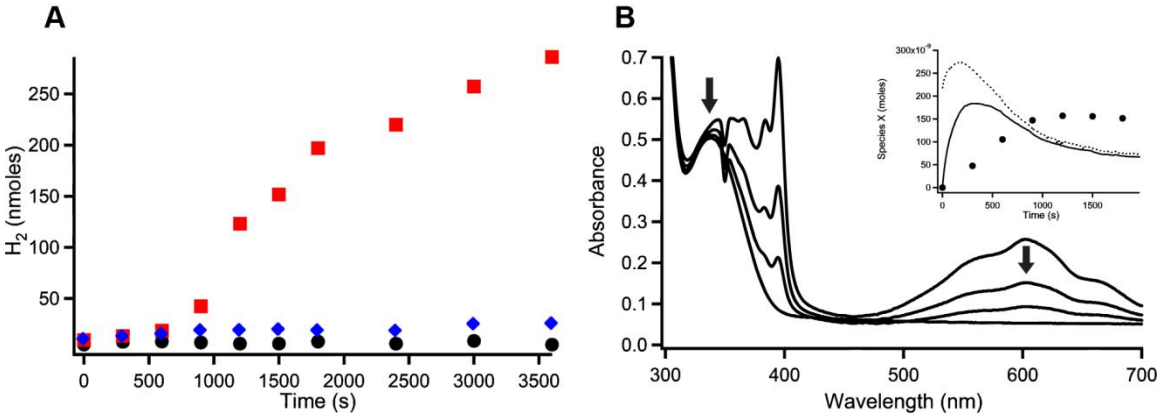

Figure 4.9 – Photo-catalytic H_2 production by SHI through NADH photolysis. A) Photo-catalytic H_2 yield for 20 nM H_2ase alone (black circles) H_2ase and 400 µM NADH (blue diamonds) and H_2ase, 400 µM NADH and 5 mM MV (red squares). B) UV-Vis spectra collected during photo-catalysis experiments. Arrows indicate wavelengths used for determination of NADH and MV concentrations during photo-catalysis. Inset shows content of NADH (dotted line), MV^+ (solid line) as determined by Beer's law from UV-Vis measurements and H_2 (circles) as determined by GC over the course of the reaction.

4.3 Conclusions

In this chapter numerous methodologies for rapid photo-reduction of two [NiFe] H_2ases were explored using gas chromatography, photoluminescence spectroscopy and FTIR spectroscopy. Using a dye sensitizer such as Tris(bipyridine)ruthenium(II) low

quantum yields for photo-catalysis were observed which were consistent with transient and steady state photoluminescence results indicating an inefficient interaction of the dye with the *Tr* [NiFe] enzyme. This was found to be due to unfavorable electrostatics for ET at the distal FeS cluster. Studies with the *Pf* SHI showed no interaction with either the excited state of the dye or with the reductively quenched species indicating either inefficient ET or non-catalytic ET as observed for γ-tagged NR-H_2ase assemblies.

Cadmium-chalcogenide based nanostructures were also examined as potential photo-catalytic platforms for rapidly initiating H_2ase reduction and showed substantial improvement in comparison to the dye sensitized system. This was shown to be due to the specific binding interactions of the hybrid complexes allowing for efficient ET to the enzyme. By comparing the catalytic progression of the active site in comparison to the photo-catalytic yields and known ET quenching efficiency significant differences between the catalytic mechanism of identical enzymes bound to the CdTe QDs relative to the dissociative dye sensitizer were determined to result from the rate of electron delivery to the H_2ase enzyme. This may have dramatic implications on the enzymatic mechanism of these enzymes with respect to the rate of electron delivery for example under physiological conditions vs. in vitro catalysis on an electrode.

H_2ase-nanostructure hybridization orientation effects were also examined using two his-tag constructs of the *Pf* SHI. Hybridization from the two different subunits to CdSe@CdS NRs revealed both configurations functioned for ET, but only the δ-tagged conjugate was functional in photo-catalysis with modest efficiency. These experiments highlight the necessity of an engineered interface between nanoparticle and enzyme as

well as shedding light on the molecular mechanism of physiological bias of the enzyme through the diode like character of ET from the γ-subunit.

Finally, NADH was examined as an irreversible photo-reductant which facilitated photo-catalysis with the redox mediator MV at modest efficiencies with high TOF and TON. This system was selected for subsequent transient experiments detailed in Chapter 5.

4.4 References

(1) Kohen, A. K., J. P.; *Accounts Chem Res* **1998**, *31*, 7.

(2) Olsson, M. H.; Parson, W. W.; Warshel, A. *Chem Rev* **2006**, *106*, 1737.

(3) Warshel, A.; Sharma, P. K.; Kato, M.; Xiang, Y.; Liu, H.; Olsson, M. H. *Chem Rev* **2006**, *106*, 3210.

(4) Hanoian, P.; Liu, C. T.; Hammes-Schiffer, S.; Benkovic, S. *Accounts Chem Res* **2015**, *48*, 482.

(5) Willstatter, R. *Chem Rev* **1933**, *13*, 11.

(6) Knapp, M. J.; Klinman, J. P. *Eur J Biochem* **2002**, *269*, 3113.

(7) Callender, R.; Dyer, R. B. *Acc Chem Res* **2015**, *48*, 407.

(8) Callender, R.; Dyer, R. B. *Chem Rev* **2006**, *106*, 3031.

(9) Krebs, C.; Price, J. C.; Baldwin, J.; Saleh, L.; Green, M. T.; Bollinger, J. M., Jr. *Inorg Chem* **2005**, *44*, 742.

(10) Gutfreund, H. *Annu Rev Biochem* **1971**, *40*, 315.

(11) Johnson, K. A. In *The Enzymes*; Sigman, D. A., Ed.; Academic Press: San Diego, CA, USA, 1992; Vol. 20, p 61.

(12) Armstrong, F. A.; Albracht, P. J. *Philos T Roy Soc A* **2005**, *363*, 937.

(13) Fontecilla-Camps, J. C.; Volbeda, A.; Cavazza, C.; Nicolet, Y. *Chem Rev* **2007**, *107*, 4273.

(14) Lubitz, W.; Reijerse, E.; van Gastel, M. *Chem Rev* **2007**, *107*, 4331.

(15) Vignais, P. M.; Billoud, B. *Chem Rev* **2007**, *107*, 4206.

(16) Vincent, K. A.; Parkin, A.; Armstrong, F. A. *Chem Rev* **2007**, *107*, 4366.

(17) Pandelia, M. E.; Ogata, H.; Lubitz, W. *Chemphyschem* **2010**, *11*, 1127.

(18) Lubitz, W.; Ogata, H.; Rudiger, O.; Reijerse, E. *Chem Rev* **2014**, *114*, 4081.

(19) Madden, C.; Vaughn, M. D.; Diez-Perez, I.; Brown, K. A.; King, P. W.; Gust, D.; Moore, A. L.; Moore, T. A. *J Am Chem Soc* **2012**, *134*, 1577.

(20) Pershad, H. R.; Duff, J. L. C.; Heering, H. A.; Duin, E. C.; Albracht, S. P. J.; Armstrong, F. A. *Biochemistry-Us* **1999**, *38*, 8992.

(21) Hartridge, H.; Roughton, F. J. W. *P R Soc Lond A-Conta* **1923**, *104*, 376.

(22) Hartridge, H.; Roughton, F. J. W. *Nature* **1923**, *111*, 325.

(23) Chance, B. *J Frankl Inst* **1940**, *229*, 737.

(24) Gibson, Q. H.; Milnes, L. *Biochem J* **1964**, *91*, 161.

(25) Tonomura, B.; Nakatani, H.; Ohnishi, M.; Yamaguchiito, J.; Hiromi, K. *Anal Biochem* **1978**, *84*, 370.

(26) Paul, C.; Kirschner, K.; Haenisch, G. *Anal Biochem* **1980**, *101*, 442.

(27) Jensen, K. *Nature* **1998**, *393*, 735.

(28) Kalidas, C.; New Age International Pvt Ltd Publishers: Darya Ganj, New Delhi, India, 2008.

(29) *Dynamic Studies In Biology: Phototriggers, Photoswitches and Caged Biomolecules*; John Wiley & Sons, Inc.,: New York, NY, USA, 2006.

(30) *Rapid Mixing and Sampling Techniques in Biochemistry*; Elsevier: New York, NY, USA, 2013.

3863.

(32) Gambin, Y.; Simonnet, C.; VanDelinder, V.; Deniz, A.; Groisman, A. *Lab Chip* **2010**, *10*, 598.

(33) Burke, K. S.; Parul, D.; Reddish, M. J.; Dyer, R. B. *Lab Chip* **2013**, *13*, 2912.

(34) Fu, W.; Drozdzewski, P. M.; Morgan, T. V.; Mortenson, L. E.; Juszczak, A.; Adams, M. W.; He, S. H.; Peck, H. D., Jr.; DerVartanian, D. V.; LeGall, J.; et al. *Biochemistry-Us* **1993**, *32*, 4813.

(35) Siebert, E.; Horch, M.; Rippers, Y.; Fritsch, J.; Frielingsdorf, S.; Lenz, O.; Velazquez Escobar, F.; Siebert, F.; Paasche, L.; Kuhlmann, U.; Lendzian, F.; Mroginski, M. A.; Zebger, I.; Hildebrandt, P. *Angew Chem Int Ed* **2013**, *52*, 5162.

(36) Fichtner, C.; van Gastel, M.; Lubitz, W. *Phys Chem Chem Phys* **2003**, *5*, 5507.

(37) Orii, Y. *Biochemistry-Us* **1993**, *32*, 11910.

(38) Winkler, J. R.; Gray, H. B. *Chem Rev* **2014**, *114*, 3369.

(39) McCray, J. A.; Herbette, L.; Kihara, T.; Trentham, D. R. *Proc Natl Acad Sci USA* **1980**, *77*, 7237.

(40) Ludovici, C.; Frohlich, R.; Vogtt, K.; Mamat, B.; Lubben, M. *Eur J Biochem* **2002**, *269*, 2630.

(41) Kohse, S.; Neubauer, A.; Pazidis, A.; Lochbrunner, S.; Kragl, U. *J Am Chem Soc* **2013**, *135*, 9407.

(42) Olshansky, L.; Pizano, A. A.; Wei, Y.; Stubbe, J.; Nocera, D. G. *J Am Chem Soc* **2014**, *136*, 16210.

(43) Brown, K. A.; Dayal, S.; Ai, X.; Rumbles, G.; King, P. W. *J Am Chem Soc* **2010**, *132*, 9672.

(44) Brown, K. A.; Wilker, M. B.; Boehm, M.; Dukovic, G.; King, P. W. *J Am Chem Soc* **2012**, *134*, 5627.

(45) Greene, B. L.; Joseph, C. A.; Maroney, M. J.; Dyer, R. B. *J Am Chem Soc* **2012**, *134*, 11108.

(46) Wilker, M. B.; Shinopoulos, K. E.; Brown, K. A.; Mulder, D. W.; King, P. W.; Dukovic, G. *J Am Chem Soc* **2014**, *136*, 4316.

(47) Reece, S. Y.; Nocera, D. G. *Annu Rev Biochem* **2009**, *78*, 673.

(48) Gogotov, I. N.; Zorin, N. A.; Serebriakova, L. T.; Kondratieva, E. N. *Biochim Biophys Acta* **1978**, *523*, 335.

(49) Zorin, N. A.; Dimon, B.; Gagnon, J.; Gaillard, J.; Carrier, P.; Vignais, P. M. *Eur J Biochem* **1996**, *241*, 675.

(50) Colbeau, A.; Kovacs, K. L.; Chabert, J.; Vignais, P. M. *Gene* **1994**, *140*, 25.

(51) Bryant, F. O.; Adams, M. W. W. *J Biol Chem* **1989**, *264*, 5070.

(52) Chandrayan, S. K.; Wu, C. H.; McTernan, P. M.; Adams, M. W. *Protein Expres Purif* **2015**, *107*, 90.

(53) Medintz, I. L.; Uyeda, H. T.; Goldman, E. R.; Mattoussi, H. *Nat Mater* **2005**, *4*, 435.

(54) Aubin-Tam, M. E.; Hamad-Schifferli, K. *Biomed Mater* **2008**, *3*, 034001.

(55) Clapp, A. R.; Medintz, I. L.; Mauro, J. M.; Fisher, B. R.; Bawendi, M. G.; Mattoussi, H. *J Am Chem Soc* **2004**, *126*, 301.

(56) Dennis, A. M.; Sotto, D. C.; Mei, B. C.; Medintz, I. L.; Mattoussi, H.; Bao, G. *Bioconj Chem* **2010**, *21*, 1160.

(57) Clapp, A. R.; Goldman, E. R.; Mattoussi, H. *Nat Protoc* **2006**, *1*, 1258.

(58) Vitt, S.; Ma, K.; Warkentin, E.; Moll, J.; Pierik, A. J.; Shima, S.; Ermler, U. *J Mol Biol* **2014**, *426*, 2813.

(59) Volbeda, A.; Charon, M. H.; Piras, C.; Hatchikian, E. C.; Frey, M.; Fontecillacamps, J. C. *Nature* **1995**, *373*, 580.

(60) Volbeda, A.; Garcin, E.; Piras, C.; deLacey, A. L.; Fernandez, V. M.; Hatchikian, E. C.; Frey, M.; FontecillaCamps, J. C. *J Am Chem Soc* **1996**, *118*, 12989.

(61) Higuchi, Y.; Yagi, T.; Yasuoka, N. *Structure* **1997**, *5*, 1671.

(62) Teixeira, M.; Moura, I.; Fauque, G.; Czechowski, M.; Berlier, Y.; Lespinat, P. A.; Legall, J.; Xavier, A. V.; Moura, J. J. G. *Biochimie* **1986**, *68*, 75.

(63) Patil, D. S.; Moura, J. J.; He, S. H.; Teixeira, M.; Prickril, B. C.; DerVartanian, D. V.; Peck, H. D., Jr.; LeGall, J.; Huynh, B. H. *J Biol Chem* **1988**, *263*, 18732.

(64) Silva, P. J.; de Castro, B.; Hagen, W. R. *J Biol Inorg Chem* **1999**, *4*, 284.

(65) Ma, K.; Schicho, R. N.; Kelly, R. M.; Adams, M. W. W. *P Natl Acad Sci USA* **1993**, *90*, 5341.

(66) Czochralska, B.; Lindqvist, L. *Chem Phys Lett* **1983**, *101*, 297.

(67) Lindqvist, L.; Czochralska, B.; Grigorov, I. *Chem Phys Lett* **1985**, *119*, 494.

Chapter 5

Rapid Initiation and Mechanistic Studies of Hydrogenase Catalysis

Aspects of this chapter have been reprinted with permission from Greene, B. L.; Wu, C. H.; McTernan, P. M.; Adams, M. W. W.; Dyer, R. B. *J. Am. Chem. Soc.* **2015** *DOI:* 10.1021/jacs.5b01791.

Abstract: The chemical mechanism of biological hydrogen oxidation and proton reduction facilitated by the hydrogenase (H_2ase) enzymes is of significant interest in bioinorganic and biomimetic chemistry. Numerous mechanisms have been proposed based on steady state behavior, but no studies to date have vindicated these mechanisms kinetically. This challenge in the field is a direct product of the difficulty in studying the reactivity of the H_2ases on their relevant timescales (<ms) by methods sensitive to enzymatic changes occurring during catalysis. In this chapter, a method for rapid initiation of proton reduction in H_2ase enzymes coupled with infrared spectroscopy, uniquely suited to probing active site function of H_2ases through the active site CO and CN ligands is exploited. The results are compared to transient visible spectroscopy sensitive to intermolecular ET as well as steady state kinetics. Based on the data presented, a new mechanism is proposed for the soluble [NiFe] H_2ase from *Pyrococcus furiosus* and mechanistic implications are presented for a novel electron bifurcating [FeFe] H_2ase from *Thermotoga maritima*.

5.1 – Introduction

Hydrogenases (H_2ases) catalyze the reversible reduction of protons to molecular hydrogen at rates that rival platinum.[1] While this is a highly advantageous property for biotechnological applications of H_2ases in bio-fuel cells, it has presented a formidable experimental challenge in elucidating the mechanism due to the high turnover rate. A sizable amount of steady state kinetic studies have been reported in addition to steady

state spectroscopic characterization of equilibrium states, but numerous questions remain.[2-6]

Steady state kinetic experiments, utilizing either chemical reductants or protein film voltammetry, have determined the mechanism of H_2 cleavage, defined pH optima for the H_2 oxidation and proton reduction reactions, Michaelis constants of H_2, directionality, maximal turnover rates, inhibition properties as well as activation energies for rate determining steps.[7-23] By coupling steady state kinetics with site directed mutagenesis, residues involved in the proton transport network have been identified and intramolecular electron transfer (ET) kinetics have been estimated.[20,22,24-26] Numerous reports have detailed kinetic properties of the hydrogenases, but due to the variability in chemical conditions employed and the vast array of host organisms used as sources of H_2ase with dissimilar amino acid and cofactor composition the results have been difficult to interpret in terms of a predictive chemical mechanism.[7,17,27,28] Although a complete chemical mechanism hasn't been developed from these studies, certain aspects of the H_2ases reactivity have become apparent.[5]

The H_2 oxidation reaction has been shown to occur through a heterolytic cleavage reaction in which the incoming H_2 molecule is heterolytically cleaved resulting in a protein bound hydride (H^-) and a proton which can exchange with the solvent.[11,12,29,30] The [NiFe] H_2ases operate optimally in proton reduction at pH <5, but lose protein stability, thus they typically show diminishing reactivity at low pH.[30-38] Conversely the pH optimum for H_2 oxidation is >10, but similarly the enzymes loose stability at this high pH and thus loose activity.[30-38] The [NiFe] H_2ases also exhibit higher overall turnover frequencies in the H_2 oxidation reaction relative to the H^+ reduction reaction under ideal

conditions.[7,28,39,40] This phenomenon has been termed the "bias" of the enzyme, but has taken numerous interpretations in the literature.[27,28,41,42] Under ideal conditions, which typically involve physisorption to pyrolytic graphite rotating disk electrodes and under large over-potentials, the turnover frequency of the [NiFe] H_2ases range from 100-10,000 s^{-1} in H_2 oxidation and 10-1000 s^{-1} for proton reduction.[7] The Michaelis constant for H_2 typically falls within a narrow range of 1-10 μM corresponding to the solubility of H_2 at <1% atmospheric composition at 298K.[39,43] This is consistent with the environmental conditions of most organisms that utilize H_2 as an obligate energy source, indicating an evolutionarily derived affinity for the substrate.[44,45] [NiFe] H_2ases have been found in mesophiles, thermophiles and hyperthermophiles, and the temperature dependence of their reactivity has been investigated, revealing activation barriers that can vary widely from 2-40 kcal/mol for H_2 oxidation and 5-30 kcal/mol for H^+ reduction.[9,14,15,31,34,36,44-48]

In a few studies, site directed mutagenesis and kinetic modeling have revealed aspects of the proton and electron transfer processes independent of active site chemistry.[25,46,49-52] Mutation of amino acids which coordinate the FeS cluster cofactors has been shown to affect the rates of inter- and intra-molecular electron transfer (ET).[22,26,51,53] Although explicit rates could not be defined, lower or upper limits for ET could be assigned for standard hydrogenases indicating that ET rates were largely heterogeneous between different cofactors.[21] The results implicated ET as potentially rate determining in H_2 oxidation consistent with previous observation. Mutations among amino acids proposed to be involved in proton transfer (PT) have been shown to affect turnover rates in both H_2 oxidation and H^+ reduction.[25] In these studies, rates of heterolytic cleavage, as measured by nuclear spin isomer scrambling experiments (ortho-

para H_2 exchange), largely do not change because this process is only dependent on active site chemistry.[25] Despite little change in heterolytic cleavage rates, large changes were observed in the overall catalytic rate as well as isotope exchange of D_2 gas with H_2O solvent.[25] The site directed mutagenesis studies of proton transport have developed an initial qualitative understanding of the proton conduction mechanism, but lack any quantitative implications. Additionally, as mentioned above, due to the large variability in amino acid composition and observed kinetics rates among the [NiFe] H_2ases, broadly applicable implications of the observed behavior of the highlighted amino acids have not been demonstrated.

Spectroscopy and x-ray crystallography have also aided our understanding of the H_2ases and their reactivity. Spectroscopic investigations, particularly electron paramagnetic resonance (EPR) spectroscopy sensitive to paramagnetic states of the enzyme, and Fourier transform infrared spectroscopy (FTIR) sensitive to the active site ligated diatomic CO and CN ligands have revealed numerous stable states of the [NiFe] and [FeFe] H_2ases, which are proposed to be involved in the reaction mechanism.[5,6,54,55] These states are described in Figure 5.1.

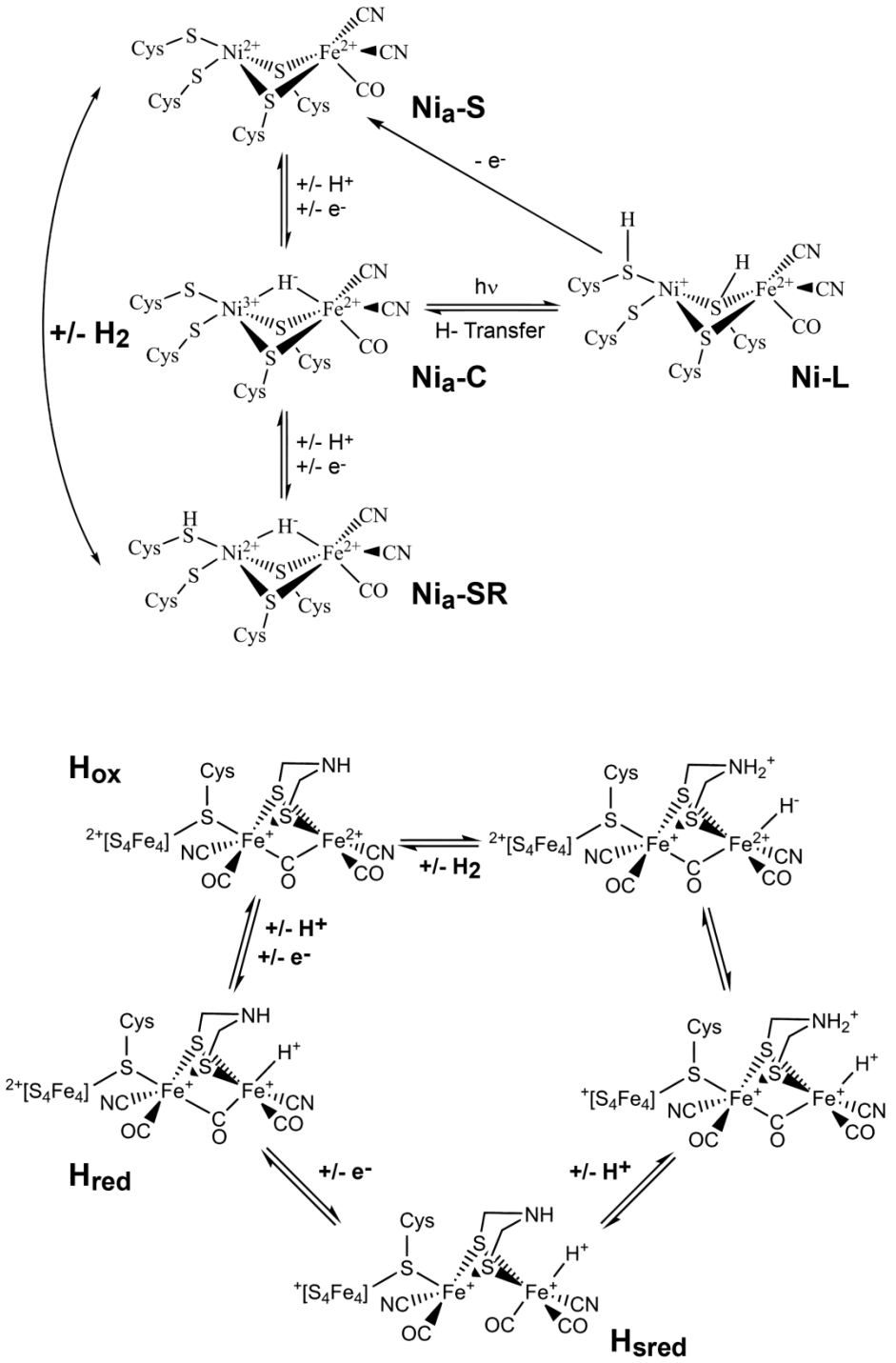

Figure 5.1 – Proposed reaction intermediates for [NiFe] (top) and [FeFe] (bottom) H_2ases.

Three steady states observed in chemically and electrochemically controlled oxidation/reduction of active [NiFe] H_2ases have been identified and have been termed Ni_a-S, Ni_a-C and Ni_a-SR.[6,56,57] Other states have been identified in thermodynamic equilibrium with the H_2/H^+ couple for various [NiFe] H_2ases, including Ni_a-SR', Ni_a-SR'' and Ni_a-SR2, but their involvement in the overall mechanism of proton reduction is at this point unclear.[5,56] Spectroscopic and crystallographic studies have also identified the binding and inhibition mechanism of carbon monoxide, which was shown to coordinate to the nickel atom of the [NiFe] active site.[58-60] Additionally, the photochemical reactivity of numerous [NiFe] H_2ases has been investigated which results in the photolysis of the bridging hydride from the Ni_a-C state.[61-65] Photolysis of the bridging hydride in Ni_a-C results in formation of at least one state best described by a monovalent nickel and a proton residing in the near vicinity at an indeterminate location.[5,6] The critical test of these proposed intermediates is their kinetic competency. This is important because thermodynamically stable equilibrium states can occur which are not along the reaction coordinate that coincidentally lie in the potential window of catalysis.

The spectroscopic characterization of the [FeFe] H_2ases has been significantly hindered relative to the [NiFe] H_2ases based on their irreversible reactivity with O_2 and the limited number of organisms which produce these enzymes at significant expression levels.[66-70] Spectroelectrochemical and chemical reactivity have been utilized in a few organisms to elucidate the basic components of the reaction intermediates which include, analogous to the [NiFe] H_2ases, three steady states termed H_{ox}, H_{red} and H_{sred}. These states are each one electron separated from one another, and the H_{ox} to H_{red} transition involves a proton as well, while the H_{red} to H_{sred} transition is still ambiguous.[71-87]

Contrary to the [NiFe] H_2ases, very little steady state kinetic studies have been performed on the [FeFe] H_2ases including electrochemical protein film voltammetry.[7,43,88-92] Because of this, the mechanism of proton and electron transfer as well as the origin of the enzymatic bias and molecular rational for the faster rate observed in these enzymes relative to their [NiFe] counterparts is unclear.

Despite the obvious pitfalls of the steady state treatment, only two studies have attempted to address the kinetic competency of the observed steady states, and only the [NiFe] H_2ases have been investigated.[93,94] In both studies, rapid mixing techniques were applied to mix the enzyme with the oxidative substrate molecule H_2 on the 10-100 ms timescale.[93,94] Both studies concluded similar results, in that the observed steady states were either consumed or formed on timescales faster than the experimental time resolution.[93,94] Thus while the known steady states were shown to form rapidly, they were not demonstrated to form faster than the turnover frequency of the enzyme, again leaving kinetic competency an open question.

In this chapter, the rapid initiation method of NADH photoionization developed in Chapter 4 was applied to the soluble H_2ase 1 (SHI) from *Pyrococcus furiosus* (*Pf*) and the electron bifurcating [FeFe] H_2ase from *Thermotoga maritima* (*Tm*). The former was studied extensively by steady state methods in Chapter 3 and by others and some aspects of the proton reduction chemistry have been determined, but again numerous questions remain. The latter has been investigated from a bioenergetics perspective due to its ability to facilitate electron bifurcation in combining the high potential electrons from NADH (-330 mV) and the low potential electrons from the *Tm* ferredoxin (-460 mV) to catalyze the reduction of protons (-414 mV, pH 7.0).[95,96] By coupling the rapid initiation

methodology to time resolved infrared and visible spectroscopy inter- and intra-molecular proton and electron transfer could be probed directly from nanoseconds to seconds resulting in the first sub-TOF characterization of a [NiFe] or [FeFe] H_2ase to date. The results are discussed in terms of a kinetically sound elementary mechanism for proton reduction in the H_2ases.

5.2 – Results and Discussion

5.2.1 – Steady State Spectroscopic Characterization of *Pf* [NiFe] SHI

Infrared spectroscopy is well established for the study of H_2ase, utilizing the intrinsic CO and CN ligands of the active site iron, which report on the electronic structure of the active site irrespective of oxidation state.[55] The CO and CN vibrational spectra of the *Pf* H_2ase (Fig. 5.2) are highly sensitive to the applied chemical or electrochemical potential, and analogously to pH as has been observed in other [NiFe] H_2ases.[55,56,97,98] The vibrational spectrum of the *Pf* SHI under a nitrogen atmosphere with12 mM NADH in phosophate buffer pH 7.0 shows a distribution of equilibrium states under mildly reducing conditions. Multi-peak fitting of the CO region based on second derivative analysis revealed peaks at 1931, 1940, 1950, 1954 and 1967 cm^{-1}. The nature of these equilibrium states were further addressed by oxidative treatment and pH dependence as well as comparison to other spectroscopically characterized [NiFe] H_2ases.

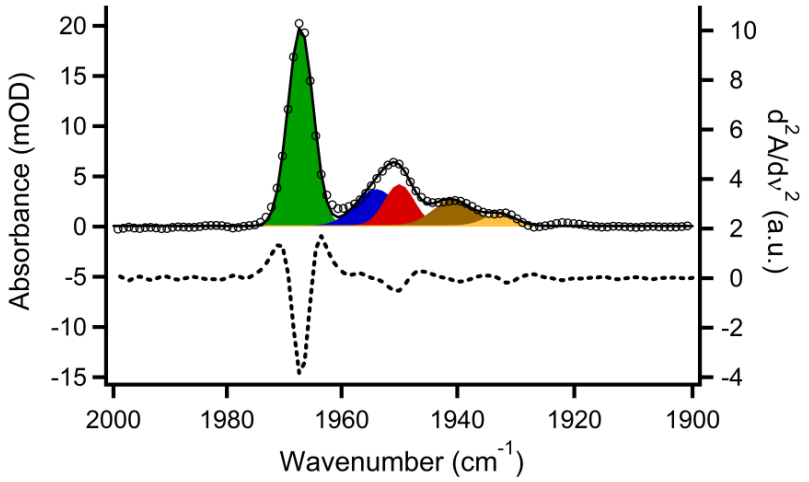

Figure 5.2 – Steady state active site FTIR analysis of the *Pf* SHI. Multi-peak Gaussian fitting to experimental data for the CO absorbance region of *Pf* SHI at pH 7.0 based on second derivative analysis, oxidative treatment and previous reports. Open circles, experimental data; solid black line, multi-Gaussian fit; colored peaks, multi-Gaussian fit components (left ordinate); dotted line, second derivative of experimental data (right ordinate).

H_2ases have been shown to be reduced electrochemically in a proton coupled manner, i.e. their reduction potential transitions between Ni_a-S, Ni_a-C and Ni_a-SR vary with pH by -59 mV/pH, nearly identical to the theoretical Nernstian prediction.[56,97] This implies that enzyme preparations with identical conditions except a change in pH will yield different equilibrium populations of the active Ni_a-S, Ni_a-C and Ni_a-SR states. This could thus be a method of aiding in assignment of the FTIR spectrum of the SHI. The pH dependent FTIR spectra of the *Pf* SHI at pH 6.3, 7.0 and 7.7 are reported in Figure 5.3. The data show a shift and broadening of the 1950 peak to the blue as well as the growth of a new CN band at 2060 cm^{-1}. The 1950 cm^{-1} band at pH 7.7 fit reasonably well to a

single Gaussian peak centered at 1950.4 cm^{-1}, but was shifted slightly by the inclusion of an additional peak at 1954 consistent with 2nd derivative and oxidative treatments. This feature grew in with decreasing pH indicating a more reduced species relative to the 1950 cm^{-1} peak. This is clearly shown by the low minus high pH difference spectrum which shows bleaches at 1948 and 1966 cm^{-1} and induced absorbances at 1954 and 1968 cm^{-1}. The 1966 to 1968 cm^{-1} spectral shift is small and has been assigned to a similar active site steady state with two different proximal FeS cluster oxidation states, which result in slightly different electron densities at the active site.

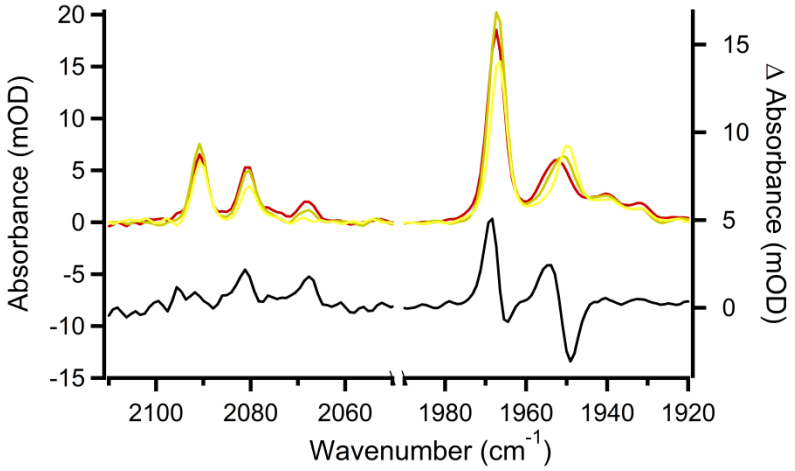

Figure 5.3 – pH dependence of the CO and CN FTIR signals and difference spectrum for low pH minus high pH data from *Pf* SHI. Colors, yellow pH 7.7; tan, pH 7.0, red pH 6.3 (left ordinate) and black pH 6.3-7.7 difference spectrum (right ordinate).

A final effort to assign the vibrational spectral properties of the *Pf* SHI involved the slow oxidation of the enzyme in the anaerobic FTIR cell when left in aerobic environments. These changes were slow and reflect the time required for H_2 to diffuse

out of the cell and O_2 to diffuse into the cell. The time dependent spectra of the oxidation process are shown in Figure 5.4. The enzyme initially was observed to have a fairly rapid decay of the 1954 cm^{-1} band. Based on this observation and the higher population at acidic pH as well as the position relative to other known H_2ases, this band was thus assigned to the most reduced steady state Ni_a-SR. The loss of this state was concomitant with the increase in the 1967 cm^{-1} band which was thus assigned to the Ni_a-C state, again based on oxidative treatment and the observed frequency relative to other known [NiFe] H_2ases. On longer timescales, the Ni_a-C state was observed to bleach, forming the species at 1950 cm^{-1}. This was followed by a final very long timescale formation of a band at 1960 cm^{-1} consistent with the Ni_r-B/Ni_u-A states known for this and other H_2ases.

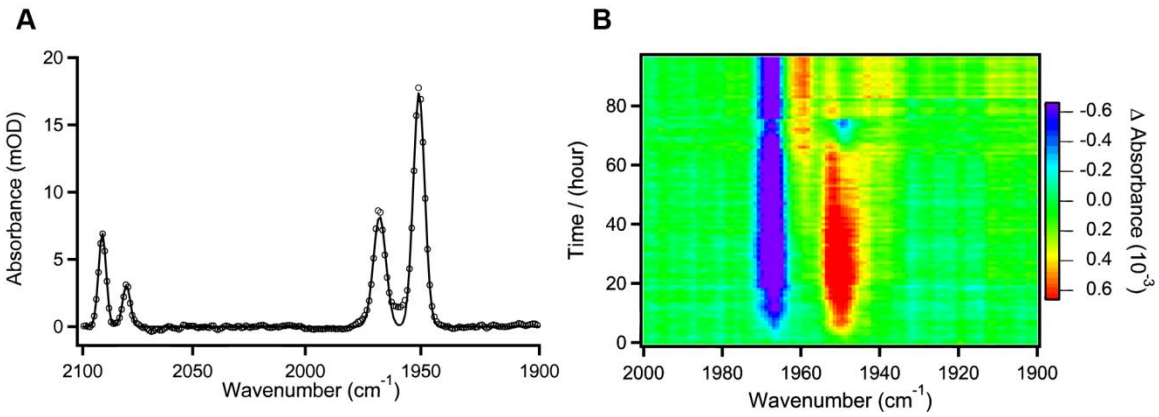

Figure 5.4 – FTIR analysis of the oxidized active site of *Pf* SHI. (A) Infrared spectrum of the CO/CN region of a transient sample a week after data collection (open circles) and associated multi-peak Gaussian fitting (solid line) which resolved only two CO and CN species at 1968 cm^{-1}, 1951 cm^{-1} (CO) and 2091 cm^{-1} and 2080 cm^{-1} (CN). (B) Infrared analysis of the CO region under slow oxidation conditions.

Based on the chemical reactivity of the various observed steady states observable by FTIR spectroscopy and comparison to literature reports of FTIR characterization of other [NiFe] H_2ases (Table 5.1) a conclusive assignment of the spectroscopic properties of the catalytically active and inactive species in the *Pf* SHI could be determined. This is a critical step to enable interpretation of transient signals from the active site.

	Absolute CO frequency (cm^{-1})			Relative frequency shift (cm^{-1})		
Organsim (Class)	Ni_a-S	Ni_a-C	Ni_a-SR	Δν S-C	Δν C-SR	Reference
A. aeolicus (I)	1927	1949	N.D.	-22	N.A.	[20]
A. vinosum (III)*	1947	1969	1955	-22	14	[21]
A. vinosum (I)	1932	1951	1936	-19	15	[22]
D. fructosovorans (I)	1933	1951	1938	-18	13	[23]
D. gigas (I)	1934	1952	1940	-18	12	[24]
D. vulgaris Myazaki F (I)	1943	1961	1948	-18	13	[25]
R. eutropha (I)	1936	1957	1948	-21	9	[26]
R. eutropha (II)	1943	1962	N.D.	-19	N.A.	[27]
R. eutropha (III)	n.d.	1961	1946	N.A.	15	[28]
Synechocystis (III)	1947	1968	1955	-21	13	[19]
P. furiosus (III)	1950	1967	1954	-17	13	This work
			Average	-19.7	13	
			Standard Deviation	1.6	1.8	

Table 5.1 - Infrared CO absorption frequencies and spectral shifts for various catalytic intermediates in numerous [NiFe] H_2ases. N.D. indicates not detected, N.A. indicates not applicable. * The spectral assignment of the *A. vinosum* soluble H_2ase was reinterpreted based on the present work and others due to inconclusive analysis in the original work, but requires further analysis to confirm.

5.2.2 – Photogeneration of e^-_{aq} and MV^+ Observed by Time Resolved Visible Spectroscopy

The method for rapidly initiating proton reduction by the *Pf* SHI involves the photo-ionization of NADH, which results in the formation of solvated electrons and $NADH^{+\bullet}$ cation radicals.[99-101] Both species are highly reactive with reduction potentials of <-1V vs. NHE. The potential for utilization of these species directly without a mediator

was investigated by transient visible absorbance sensitive to the solvated electron absorbance due to its broad absorption band centered at 715 nm in H_2O.[102-104] This transition is related to the essential particle in a box description of the water solvation shell potential well on the electron.[103] The power dependence on solvated electron production after photolysis probed at 670 nm is shown in Figure 5.5. The transients show two phases, a fast phase at ~ 100-200 ns and a slower phase at 1-10 μs. Both phases were shown to accelerate at higher power and their amplitudes also increased with increasing power. This is consistent with a recombination process in which the photo-generated solvated electrons recombine with solvent protons or $NAD^{\bullet}$ radicals. This is not an advantageous process for efficient initiation of the *Pf* SHI for two reasons. First, the rate of decay is extremely fast, which may compete with intermolecular ET from the solvated electron to the *Pf* SHI, and based on the extinction coefficient of the solvated electron at this wavelength (ca. 7,000 M^{-1} cm^{-1}) less than 200 μM solvated electrons remain at 100 ns in the lowest fluence, a relatively small amount. Thus methyl viologen was again used as a rapid electron acceptor to mitigate the high reactivity of the solvated electron and $NAD^{\bullet}$ radicals.

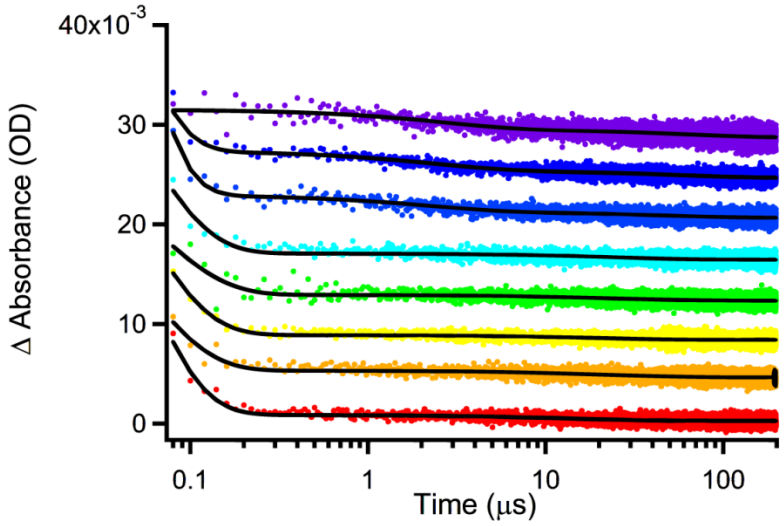

Figure 5.5 – Power dependence of solvated electron production from NADH photo-ionization measured by transient visible absorbance. Pump energy was varied from 0.01 to 2.2 mJ/pulse.

In an analogous set of transient visible experiments again probing at 670 nm, the MV concentration dependence was examined under constant laser pulse power to determine total reductant generated as a result of the NADH photolysis pulse (Fig. 5.6). Using the extinction coefficient of MV^+ at 670 nm (ca. 3,000 M^{-1} cm^{-1}) and the transient absorbance at 100 μs the total MV^+ produced was calculated for each transient. At low MV concentration, very little MV^+ was produced indicating that the bimolecular rate constant was smaller than the lifetime of the solvated electron and/or NAD radical. At increased concentration, a linear relationship was observed with MV concentration consistent with a first order process in MV^{2+}, which plateaued at ~1.6 mM, indicating that 1.6 mM reducing equivalents were generated by the photolysis pulse from photoionization of 800 μM NADH assuming stoichiometric conversion of NADH photoproducts to MV^+. Based on the sample absorbance and fluence it is calculated that

the photo-ionization process was 0.01% efficient based on a single photon absorption analysis, and 3% based on two photon absorption events. This is reasonably close to the literature value of 10%, and the underestimate is likely due to decay of photo-products faster than their reactivity with MV^{2+}.[101]

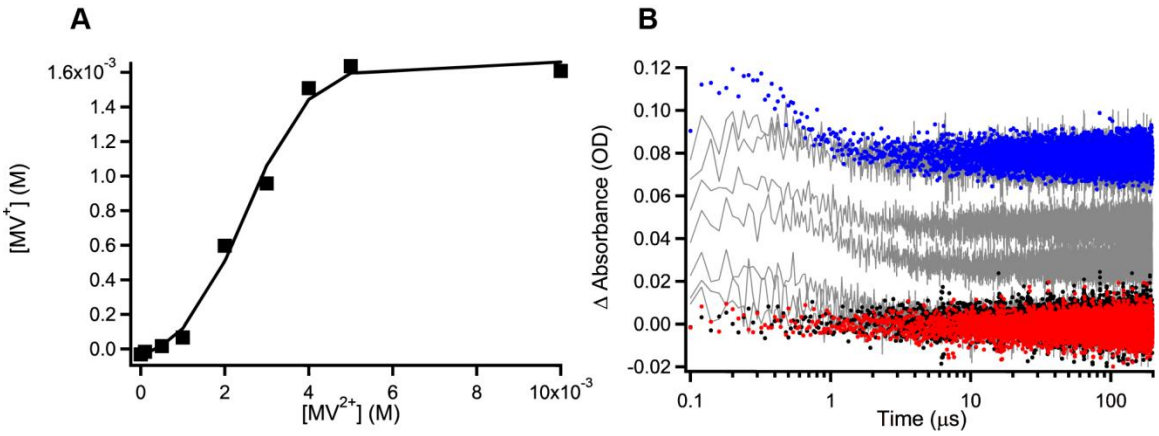

Figure 5.6 – MV^{2+} concentration dependence on MV^{+} yield. A) Photo-generated MV^{+} at 100 μs calculated by transient absorbance values from (A). B) Transient visible absorbance traces probed at 670 nm of NADH photoionization at various MV^{2+} concentrations. Transients at 10 mM MV^{2+} shown in blue, 0 mM MV^{2+} shown in red and 0 mM NADH with 10 mM MV^{2+} in black, intermediate concentrations shown in gray.

In addition to the concentration dependence of NADH photo-ionization, the fluence dependence of the NADH photo-ionization in the presence of MV^{2+} was investigated under MV^{2+} excess (10:1, Fig. 5.7). Similarly to the MV^{2+} concentration dependence measurements, the data were described well by a linear relationship over a wide fluence range from 0-2 mJ/pulse and constant illumination area. At high fluence, a feature at early time emerged (100-500 ns) which, based on concomitant transient

infrared data collected was due to cavitation, which scattered the probe beam resulting in an apparent induced absorbance until the microbubbles formed during cavitation dissolved again. A satisfactory set of experimental conditions which did not appear to excessively cavitate, but resulted in substantial MV production could be achieved by MV^{2+} concentrations > 5 mM and pump pulse energies of < 1 mJ/pulse in a 300 μm diameter spot.

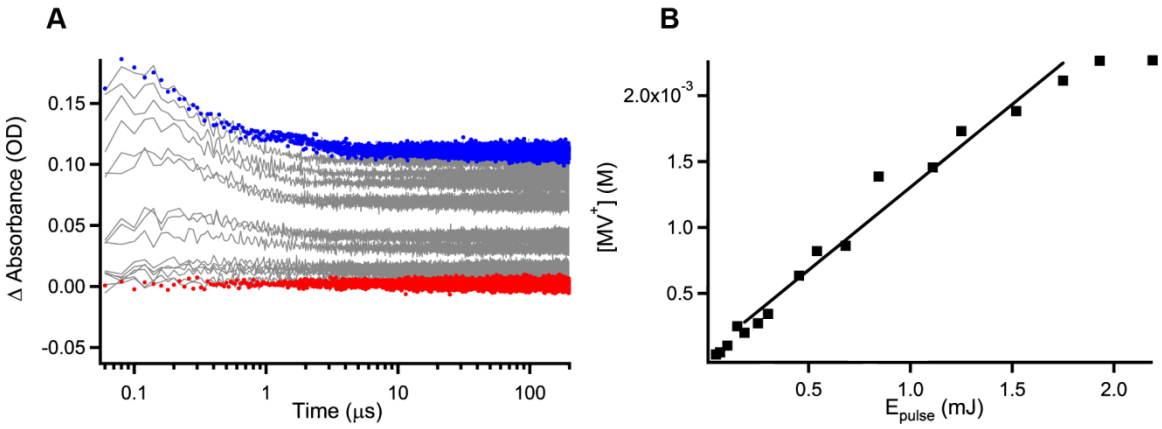

Figure 5.7 – Power dependence on MV^{+} yield. A) Transient visible absorbance traces probed at 670 nm of NADH photoionization at various pump energies from 0.01 (red) to 2.2 (blue) mJ/pulse. B) Photo-generated MV^{+} at 100 μs calculated by transient absorbance values from (A).

5.2.3 – Photo-reduction of MetMb: A Case Study

As a proof of principle for the tandem transient infrared and visible analysis of interfacial ET and active site dynamics of the Pf SHI, the photo-reduction of ferric myoglobin (MetMb) by MV^{+} produced during photolysis and subsequent CO binding to ferrous myoglobin (deoxyMb) forming the CO adduct to ferrous myoglobin (MbCO) was

examined utilizing its characteristic CO stretching frequency at 1944 cm^{-1}, which is spectrally very similar to the active site metal bound carbonyls of the Pf SHI (*vida supra*). In these experiments, the photolysis pulse generated a burst of solvated electrons and cation radicals which could reduce the MetMb directly, or be quenched by MV^{2+}, which can also reduce MetMb. After reduction, dissolved CO from the CO saturated solution could diffusionally bind to deoxyMb, a well characterized process. Transient data are shown below in Figure 5.8. Upon photolysis, an initial difference in the transient infrared bleach is observed at very early time. This is likely due to a small population of MbCO generated slowly in the cell due to the direct ground state reactivity of MetMb and NADH in solution, which produces deoxyMb which in turn binds exogenous CO. By normalization and subtraction of a reference spectrum of photo-reduction of MetMb in the absence of CO, the CO binding could be analyzed. The results showed two phases, one of which was fast with a rate of 1.7×10^{4} s^{-1} and another with a rate of $9.1 \times 10^{\$}$ s^{-1}. The two phases are attributed to static trapped CO photolysis products and completely liberated CO photolysis products which rebind with different kinetics.[105-107]

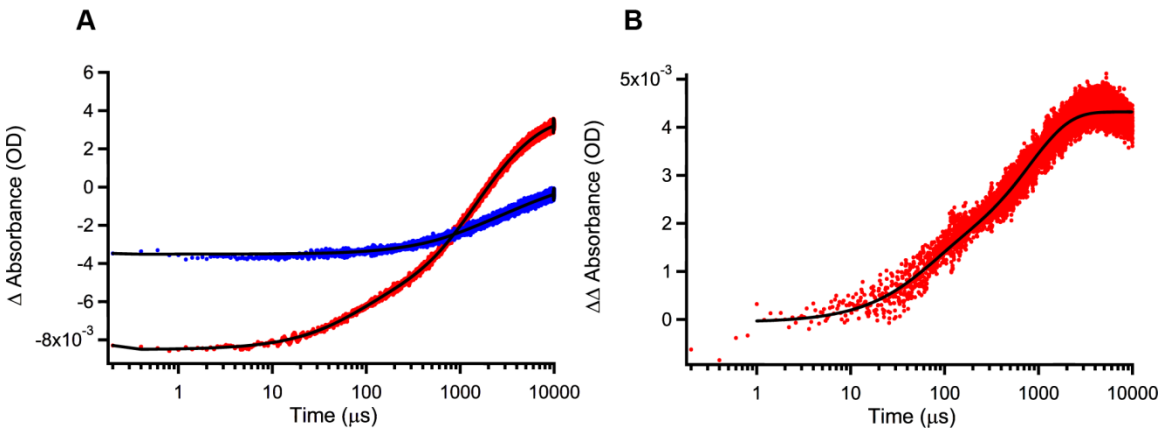

Figure 5.8 – Infrared transient absorbance of CO binding to deoxymyoglobin generated by the photo-reduction of MetMb by NADH photolysis. A) Raw infrared transient difference absorbance of 2 mM Mb (red) and a reference of 10 mM NADH and 10 mM MV^{2+} (blue) in 50 mM phosphate buffer pD 7.0 probed at 1944 cm^{-1}. B) Transient double difference of the normalized data from (A).

The transient results reported above were also consistent with steady state UV-Vis and FTIR analysis of the Mb sample (Fig. 5.9). FTIR analysis confirmed the small initial population of MbCO, which was dramatically increased upon illumination in the cell. The total increase in MbCO was 8 mOD, which was only slightly larger than the transient value of 5 mOD, which is consistent with the additional ground state reduction by NADH observed initially, which continued in the cell during the transient experiments. UV-Vis analysis revealed that nearly 100% of the MetMb (Soret at 409 nm) was reduced and it all formed the reduced CO bound MbCO (Soret at 424 nm) with no production of deoxyMb.

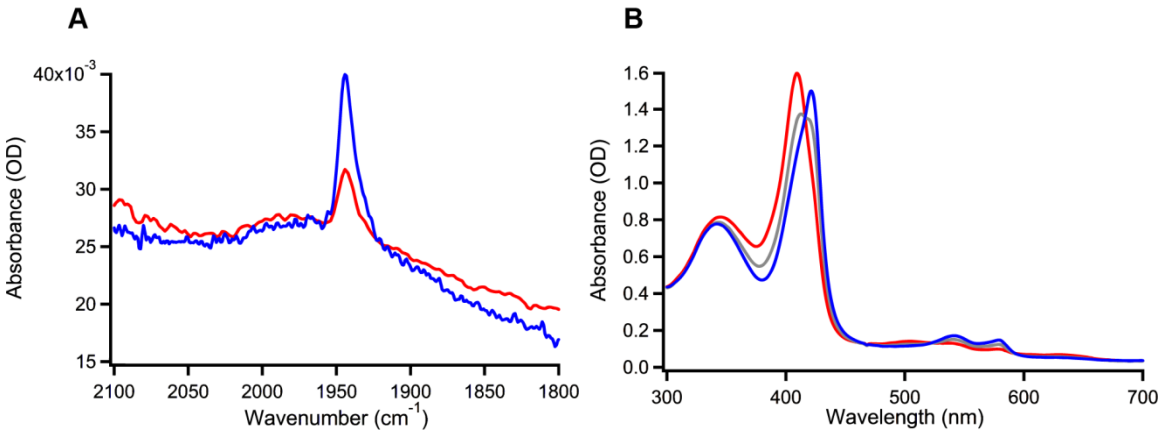

Figure 5.9 – Steady state characterization of photo-reduction of MetMb in the presence of saturated CO. A) FTIR of 2 mM Mb before (red) and after (blue) photolysis with 10 mM NADH and 10 mM MV^{2+} in 50 mM phosphate buffer pD 7.0. B) UV-vis of 2 mM Mb before (red) and during (grey) and after (blue) photolysis.

With the establishment of the ability to simultaneously monitor transient signals from both infrared and visible dynamics in a single photolysis pulse with high signal to noise in the infrared region of interest, a photo-triggering scheme and analytically method for investigating pre-steady state kinetics of the [NiFe] H_2ase from *Pf* could be tested experimentally. The results of such a study are reported below.

5.2.4 – Photo-reduction of *Pf* SHI

To confirm sub-TOF intermolecular ET of photolysis generated MV+ with the SHI, transient visible absorbance of the MV^+ radical probed at 635 nm (ε_{635} = 5,500 M^{-1} cm^{-1}), was conducted and is shown in Figure 5.10 below. In control experiments, photo-ionization of NADH resulted in the production of 530 µM MV^+ in the absence of the catalytic acceptor SHI. This MV^+ concentration jump was capable of decreasing the

equilibrium reduction potential in the cell by 50 mV as determined by a simple Nernstian calculation based on an initial solution reduction potential determined by the enzyme at NADH at approximately -330 mV and the concentration jump of 530 µM MV^{+}.

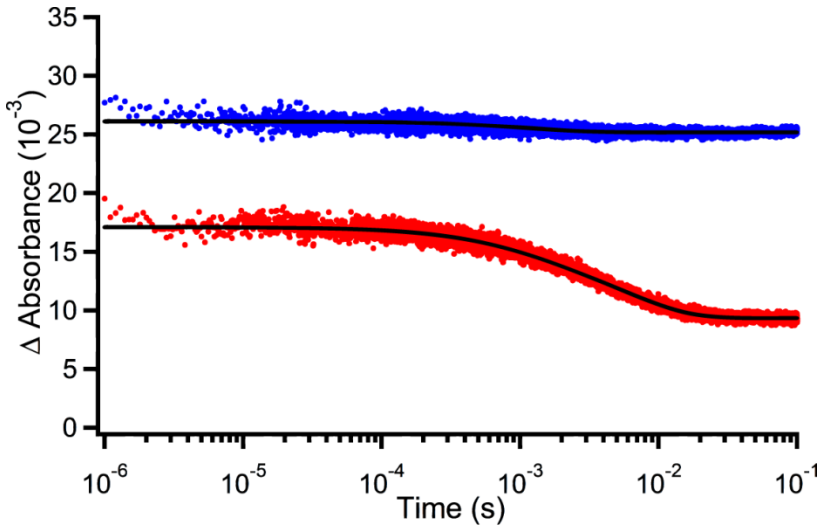

Figure 5.10 – Intermolecular ET dynamics of MV^{+} with *Pf* SHI. Transient visible data probed at 635 nm after photolysis for deoxyMb (blue) and SHI (red) with associated exponential fits (black).

DeoxyMb was used in these control experiments as a protein-based UV absorber that did not interact with MV^{+} to match the optical density at the pump wavelength relative to the H_2ase samples, thus matching the inner filter effect. The MV^{+} signal decayed less than 5% over 100 ms post photolysis, confirming the anaerobic environment of the IR cell. When SHI was present, dramatic differences in the initial absorbance and subsequent decay kinetics of MV^{+} were observed. We attribute the initial absorbance difference to direct reduction of SHI by the solvated electron occurring faster than the experimental time resolution, which competes with MV^{2+} reduction. Based on the difference in MV^{+} formation in the H_2ase samples relative to the deoxyMb samples, 200 µM of solvated

electrons are consumed by SHI by intermolecular ET, presumably to an exposed FeS cluster or the flavin unit, on a very rapid timescale (<100 ns). The subsequent decay of MV^+ was observed to be bi-phasic, with relaxation rates of 1.0 x 10^3 s^{-1} (40%) and 2.0 x 10^2 s^{-1} (60%) with a net consumption of 200 µM MV^+. We attribute the two phases to multiple ET sites on the enzyme surface with competitive, but different rates, such as the flavin or Fe_4S_4 cofactors.[36,108,109] These results demonstrate a cumulative reduction of 400 µM H_2ase (~27%) within *ca* 5 ms, well below the enzymes TOF, approximately half of which occurs faster than the time resolution of the experiment. The equilibrium distribution of Ni_a-S, Ni_a-C and Ni_a-SR are expected to react with equal probability based on initial populations with the solvated electron, $NADH^{+\bullet}$ radical and MV^+, thus active site dynamics unhindered by any other kinetic process should be observed on these timescales. After partial MV^+ oxidation, a new H_2ase/MV equilibrium was established, as demonstrated by the stable residual MV^+ absorbance, which persisted with minimal diffusional decay for minutes. Based on the initial enzyme equilibrium state populations of Ni_a-S, Ni_a-C and Ni_a-SR, it is expected that little H_2 is produced with these modest potential jumps below the H_2/H^+ couple, but that substantial enzyme reduction occurs. Thus the inter-conversion of the equilibrium states could be examined by this method despite little overall turnover. FTIR spectra were collected before and after photolysis experiments indicated negligible photo-degradation during transient data collection (data not shown) indicating that the photo-catalysis induced activity loss previously observed in bulk photolysis experiments (Chapter 4) is the result of enzyme degradation and not due to direct photo-degradation.

Nanosecond transient infrared absorbance signals (Fig. 5.11) from the steady states Ni_a-S, Ni_a-C, Ni_a-SR and the photo-product Ni-L were collected simultaneously with the visible transients at probe frequencies illustrated in Fig. 1a. This was highly advantageous since interfacial ET and active site chemistry could be resolved under identical conditions at the same time, which substantially aided in the analysis. Dynamics for Ni_a-S, Ni_a-C and Ni_a-SR were observed within the overall TOF of the enzyme, the first direct evidence validating the kinetic competency of these proposed intermediates. Kinetic competency is crucial in determining the relevance of the observed equilibrium states in the catalytic cycle, eliminating their potential as off-pathway thermodynamic trap states.

Ni_a-S yielded transients displaying three phases (red trace in Fig. 5.11). The earliest feature observed was an induced absorbance with a relaxation rate of $2.9 \pm 0.3 \times 10^5\ s^{-1}$. We attributed this phase to the formation of Ni_a-S by ET (and possibly PT) from the photo-product Ni-L state, a recently discovered phenomenon.[110] This process is the most direct measure of the ET rate between the proximal iron-sulfur cluster and the [NiFe] active site to date. This may aid in the experimental determination of the reorganization energy and wave function overlap in ET to the active site from the proximal Fe_4S_4 cluster, a common feature of all [NiFe] H_2ases. Subsequently, a biphasic decay with rates of $1.8 \pm 0.2 \times 10^4\ s^{-1}$ (56%) and $5.0 \pm 2.4 \times 10^2\ s^{-1}$ (44%) was observed yielding a net bleach of the Ni_a-S absorbance, verifying a shift of the system to lower potential. The two bleach phases are attributed to reduction by solvated electrons and MV^+ respectively based on the associated timescales and amplitudes. We observed a substantial lag phase between the interfacial reduction of the enzyme by the solvated

electron (<100ns) and the eventual reduction of the active site (>50μs). This lag phase describes the time required for ET through the protein to the buried active site following intermolecular ET; the lifetime is reasonable since ET between the proximal iron-sulfur cluster and the active site is on the order of a few microseconds (*vide supra*) and there are likely multiple intramolecular ET steps.

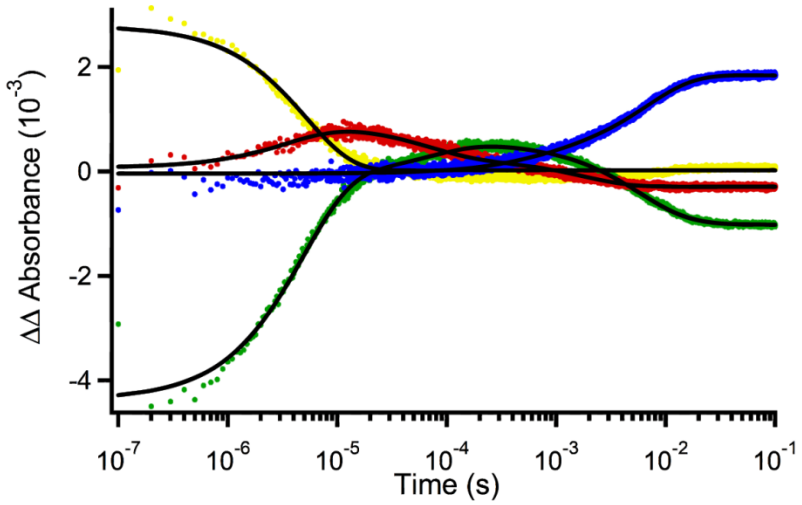

Figure 5.11 – Transient infrared data probed at frequencies illustrated in Figure 1(a). Color scheme: Ni_a-S (1948 cm^{-1}), red; Ni_a-C (1967 cm^{-1}), green; Ni-L (1920 cm^{-1}), yellow; and Ni_a-SR (1954 cm^{-1}), blue; global fits, black. Inset shows kinetic model used to fit the experimental data.

The transient signals of the Ni_a-C state yielded more complex dynamics (green trace of Fig. 5.11), as expected for an intermediate state. Immediately after the photo-ionization pulse, a bleach of the Ni_a-C state was observed due to fast (unresolved) photolysis of the bridging hydride, which is presumably binds as a proton to a nearby base, a well-known phenomenon in [NiFe] H_2ases. The photolysis product Ni-L relaxed

back to the Ni_a-C state with a rate of $1.94 \pm 0.14 \times 10^5$ s^{-1}. Further assignment of the photolytic production of the Ni-L state was performed in the absence of NADH (Fig. 5.12), in which two spectrally similar Ni-L states (1916 and 1923 cm^{-1}) were observed with very similar relaxation rates (2.0×10^5 and 1.4×10^5 s^{-1} respectively at pH 7.0). Multiple photo-product states have been observed before and have been ascribed to different acceptor sites on the active site sulfur ligands.[5,57,111-114] The recovery of Ni_a-C from both Ni-L states were an order of magnitude faster than that predicted from cryogenic experiments for the H_2ase of *Desulfovibrio vulgaris* Miyazaki F.[111] This apparent discrepancy could be explained by a lowering of the activation barrier of the proton transfer step at room temperature due to the thermal mobility of an associated proton donor. This is corroborated by a smaller observed KIE (vida infra) of 2.8 relative to that observed at cyrogenic temperatures of ca. 6.[111] An induced absorbance of the Ni_a-C transients was observed at intermediate time, concomitant and opposite in sign to the decay signal from Ni_a-S. We assign this process to the formation of Ni_a-C from Ni_a-S via a concerted mechanism. At later time, a bleaching of the Ni_a-C signal was observed with a rate of $2.2 \pm 0.4 \times 10^2$ s^{-1} attributed to reduction of Ni_a-C to form Ni_a-SR. This 100-fold slower rate implies dissimilar mechanisms for the Ni_a-C state reduction relative to Ni_a-S reduction.

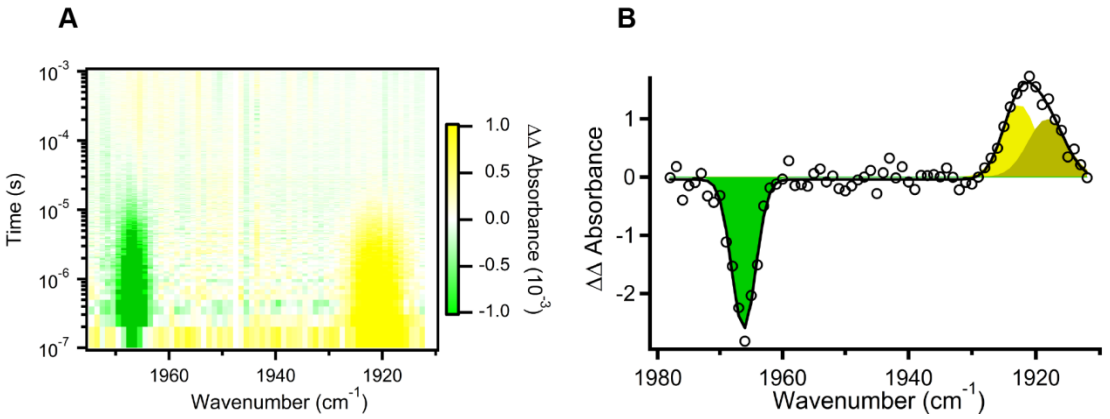

Figure 5.12 – Transient infrared analysis of SHI photochemistry. A) Transient infrared spectrum of SHI after photo-excitation with 355 nm light at 1 cm^{-1} resolution. B) Transient infrared spectrum at 500 ns. Circles represent experimental data, solid line represents multi-Gaussian fit, colored peaks represent multi-Gaussian fit components.

The most reduced active state, Ni_a-SR, also showed dynamics in our experiments with an induced absorbance at 1.9 ± 0.3 x 10^2 s^{-1} (blue trace Fig. 5.12). This was slightly delayed in time relative to the Ni_a-C state bleach indicating the presence of an intermediate, providing further evidence that the mechanisms of proton associated reduction of Ni_a-S and Ni_a-C are distinct. Based on independent kinetic analysis, a coupled kinetic model was applied. The coupled model resulted in fits to the experimental data with similar but opposite amplitudes for transitions between connected states. Assuming similar oscillator strengths and a reasonable extinction coefficient of 1,000 M^{-1} cm^{-1}, the total enzyme reduction was *ca* 350 µM, which is again in agreement with the calculated electron transfer yield determined from the visible transient absorbance data.

5.2.5 – Mechanistic Aspects of Proton Reduction by *Pf* SHI.

The methodology established above set the stage for in depth investigation of the elementary mechanisms involved in PT, ET and active site chemistry. Little is known about key elements, including the overall rate determining step(s), the effects of the protein matrix on ET and PT as well as the rates of active site chemistry relative to ET and PT. These details are critical in developing a complete understanding of the catalytic mechanism and may give rationale for the reversibility, bias and efficiency observed in these enzymes. Thus, to investigate the nature of proton and electron transfer in the conversion of Ni_a-S to Ni_a-C and Ni_a-C to Ni_a-SR, the transient experiments were reexamined at pH 7.0 and pH 7.7 as well as in D_2O (Fig. 5.13). The steady state behavior under differing pH and solvent isotopes was also investigated for comparison to pre-steady state kinetics data (Fig. 5.13 and Chapter 3).

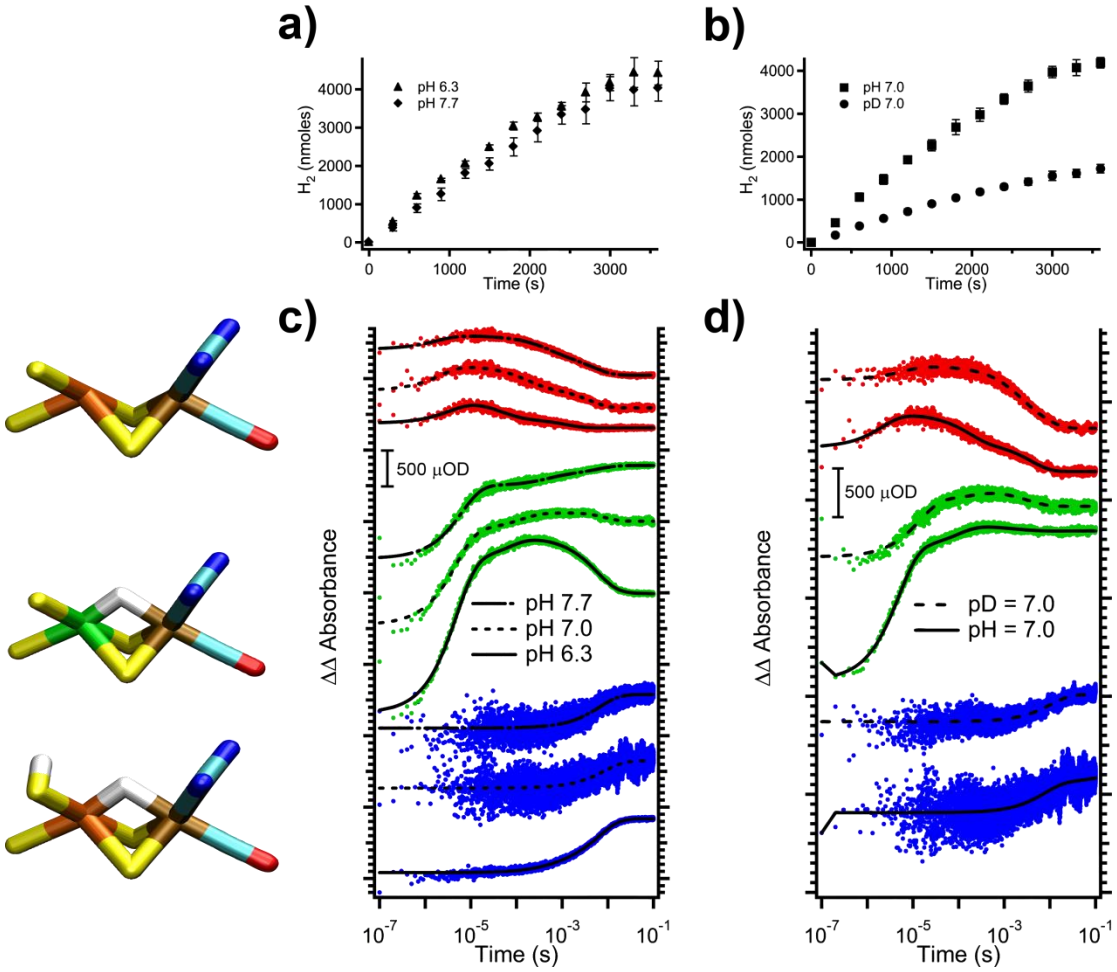

Figure 5.13 – pH and solvent isotope effects on steady state and pre-steady state proton reduction kinetics. (a) H_2 production steady state kinetics at pH 7.7 (diamonds) and 6.3 (triangles). (b) H_2/D_2 production steady state kinetics at pH 7.0 (squares) and pD 7.0 (circles). (c) Transient infrared signatures for Ni_a-S (red), Ni_a-C (green) and Ni_a-SR (blue) with associated fits (black lines) at pH 7.7 (dotted dashed lines), 7.0 (dotted lines) and 6.3 (solid lines). (d) Transient infrared signatures for Ni_a-S (red), Ni_a-C (green) and Ni_a-SR (blue) with associated fits (black lines) at pH 7.0 (solid lines) and pD 7.0 (dotted lines). Structures of the [NiFe] active site in the various equilibrium redox states are visualized pictorially to the left of the associated transient data based on the recent structure of the [NiFe] H_2ase from *Desulfovibrio vulgaris* Miyazaki F (PDB 4U9H).

The concerted bleach of the Ni_a-S state and induced absorbance of the Ni_a-C state were highly pH dependent, with rates ranging from 2,300-18,000 s^{-1} from pH 7.7 to 6.3 (Table 5.3). We conclude from these data that the conversion of Ni_a-S to Ni_a-C occurs through a concerted mechanism modulated by protonation of a donor residue near the active site with a pK_a near 7. The amplitudes of these features were also affected by pH with basic pH yielding the largest Ni_a-S bleach signals, consistent with initial Ni_a-S state content (Table 5.2). This was corroborated by the observed Ni_a-C and Ni_a-SR state dynamics, which show a trend towards Ni_a-C state production over Ni_a-SR at higher pH, again consistent with the equilibrium concentrations of these species.

State\pH	6.3 (μM)	7.0 (μM)	7.7 (μM)
Ni_a-S	200	330	570
Ni_a-C	1000	1000	920
Ni_a-SR	300	170	10

Table 5.2 – Equilibrium initial concentrations for transient experiments as determined by FTIR analysis of transient samples and Gaussian curve fitting of spectral components.

The nature of the concerted Ni_a-S to Ni_a-C transition was further examined by the H/D kinetic isotope effect (KIE). The KIE of concerted EPT processes are known to be unusually high ($k_H/k_D > 7$) in situations which involve an elementary electron-proton transfer reaction (proton and electron tunneling) due to the decrease in tunneling probability with the shortening of the de Broglie wavelength of the deuteron relative to the proton.[115-117] The kinetics of Ni_a-S reduction in H_2O and D_2O (Fig. 5.13 D) were

drastically different. The KIE for Ni_a-S to Ni_a-C conversion was pH dependent and varied from 6 +/- 1 to 43 +/- 6 in the pH(D) range of 7.7 to 6.3 respectively (Table 5.3).

Phase	pH 6.3 (s^{-1})	pH 7.0 (s^{-1})	pH 7.7 (s^{-1})	pD 6.3 (s^{-1})	pD 7.0 (s^{-1})	pD 7.7 (s^{-1})
S formation from L	289,000 +/- 30,000	428,000 +/- 12,000	460,000 +/- 50,000	242,000 +/- 1150	160,000 +/- 7,000	43,000 +/- 11,000
S bleach 1	18,000 +/- 1,800	6,650 +/- 920	2,260 +/- 189	422 +/- 66	414 +/- 20	339 +/- 56
S bleach 2	500 +/- 240	206 +/- 90	222 +/- 20	86 +/- 9	203 +/- 38	86 +/- 21
L recovery from C	194,000 +/- 14,000	185,000 +/- 13,000	160,000 +/- 2,000	101,000 +/- 7,000	66,000 +/- 3,000	78,000 +/- 5,600
C bleach	220 +/- 40	305 +/- 43	235 +/- 13	N.O.	260 +/- 28	N.O.
SR formation	193 +/-25	137 +/- 19	122 +/- 16	72	171 +/- 33	N.O.

Table 5.3 – Relaxation rate constants for pH(D) dependent pre-steady state kinetics. Errors represent the standard deviation of three independent measurements. Red values represent the results from a single transient experiment.

The large KIE at acidic pH can only be reconciled by an EPT rate determining step involving proton tunneling, whereas the basic KIE is more consistent with classical primary KIE process being rate determining. Additionally, in separate experiments the activation barrier for the EPT process at pH 6.3, where the EPT mechanism is dominant, was determined to be 1.5 kcal/mol (Fig. 5.14). This very low value is consistent with a fast, concerted EPT that is kinetically competitive with alternative ET and PT pathways. This low value is compared to barriers determined similarly for ET and PT processes in Ni-L relaxation to Ni_a-S (10 kcal/mol), Ni-L relaxation to Ni_a-C (5 kcal/mol) and ETPT from Ni_a-C to Ni_a-SR (10 kcal/mol).

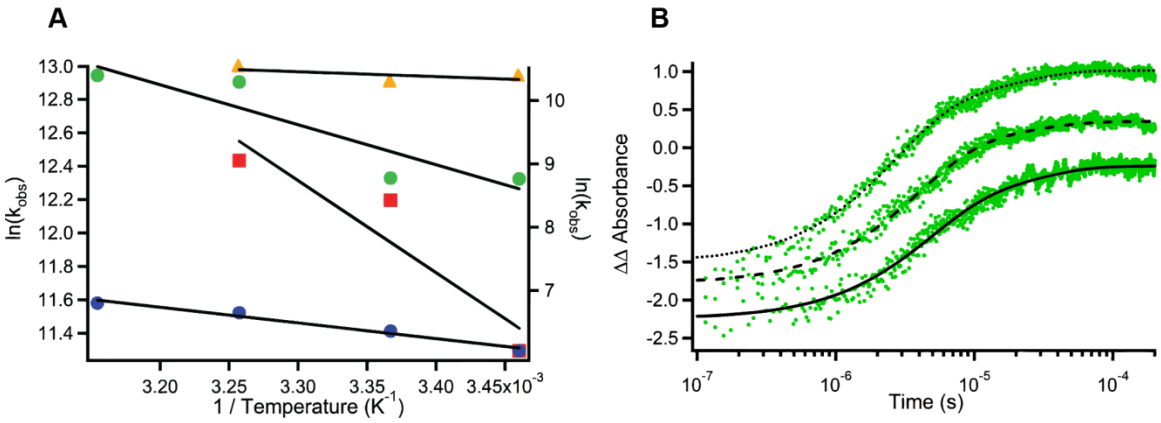

Figure 5.14 – Temperature dependence of Ni-L recovery to Ni_a-S, Ni-L recovery to Ni_a-C, Ni_a-S reduction to Ni_a-C and Ni_a-C reduction to Ni_a-SR. A) Arrhenius plots of rates of Ni_a-S formation from Ni-L (red squares), Ni_a-C formation from Ni-L (green circles), Ni_a-S reduction to Ni_a-C (orange triangles) and Ni_a-C reduction to Ni_a-SR^- (blue circles). Activation barriers were determined at 10 kcal/mol, 5 kcal/mol, 1.5 kcal/mol and 5 kcal/mol respectively. B) Temperature dependent transient infrared traces at 16.4 (solid line fit), 24.3 (dashed line fit) and 34.6˚C (dotted line fit) of the Ni_a-C state probed at 1967 cm^{-1}. Data offset for clarity.

EPT is, in theory, pH independent. To rationalize the observed pH dependence we propose a simple kinetic model in which the EPT mechanism is gated by protonation of one or more ionizable amino acids in the protein. Since this reaction is fast relative to enzyme turnover, it is not expected to be reflected in the steady state data, which is clear from the minimal steady state KIE of 2.6 and the small pH dependence. This result highlights the substantial mechanistic insights obtained from sub-TOF kinetics experiments that are obscured by steady state measurements. This is the first direct evidence for a MS-EPT mechanism in an enzyme as far as we are aware. In the MS-EPT

mechanism, proton tunneling from an amino acid residue adjacent to the active site is coupled to long range electron transfer from the proximal Fe_4S_4 cluster to the [NiFe] active site.

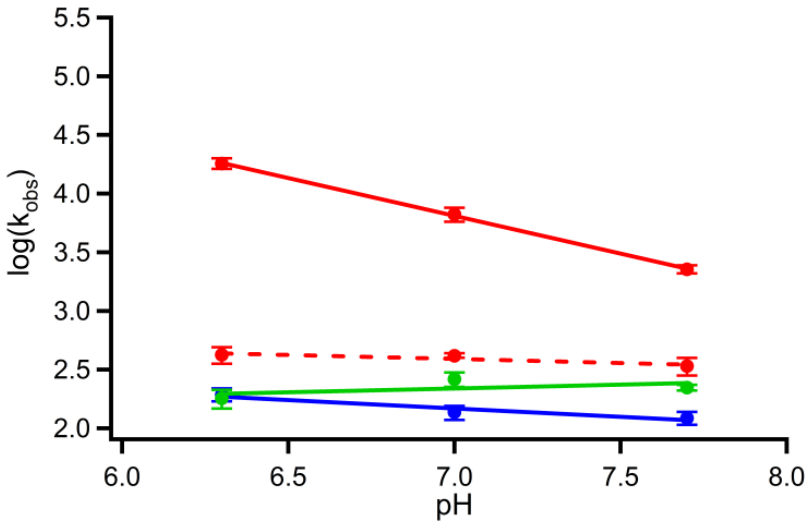

Figure 5.15 – $log(k_{obs})$ versus pH(D) for Ni_a-S conversion to Ni_a-C, Ni_a-C bleaching and Ni_a-SR formation. Ni_a-S reduction (concerted formation of Ni_a-C) in H_2O shown in red solid lines, in D_2O shown in red dashed lines, Ni_a-C reduction in H_2O shown in green solid line, Ni_a-SR formation in H_2O shown in blue solid line. Error bars represent the standard deviation of the observed rate constants based on three independent measurements.

This mechanism is distinct from the H-atom transfer in soybean lipoxygenase where a proton and electron are transferred from a single bonding orbital. The Ni_a-S to Ni_a-C state transition necessarily involves proton and electron transfer as well as hydride formation. We observed no intermediate in this process, nor in the Ni-L recovery to Ni_a-C, which also involves proton transfer and subsequent hydride formation. Thus the

hydride formation chemical step must occur much faster (<50 μs) than the concerted EPT step. This reduced protonated state is involved in catalysis, but based on our measurements, could not be observed due to the slower EPT relative to hydride formation. We therefore term this state the Ni_a-I state based on its presence in the mechanism as a fleeting intermediate state *en route* to Ni_a-C state formation. This claim is supported by theoretical predictions where a reduced protonated state is predicted as an intermediate.[50-52] Importantly, our data also indicate that the Ni_a-I to Ni_a-C and Ni-L to Ni_a-C transitions are remarkably similar and thus the photo-chemical dynamics may be a rich model system for experimentally disentangling the hydride formation from the EPT process. Based on our observations of multiple Ni-L states at room temperature, it is likely that these states result in different proton binding sites upon hydride photolysis. Thus the Ni_a-I state may in fact be identical to one of the observed Ni_a-L states allowing this kinetically obscured reaction intermediate to be studied more extensively.

The kinetics of Ni_a-S conversion to Ni_a-C in D_2O was also fit well to a concerted step, but showed little pH dependence. The $\log(k_{obs})$ versus pH(D) plot for the Ni_a-S to Ni_a-C conversion in H_2O and D_2O (Fig. 5.15) dramatically shows this difference. Based on the small pH dependence of the Ni_a-S to Ni_a-C conversion in D_2O we propose that this process occurs through a PT-ET step-wise mechanism in which the active site is protonated, followed by fast reduction to form the Ni_a-I state which subsequently forms the bridging hydride rapidly to finally form Ni_a-C. This PT-ET mechanism is intuitive because the reduction of the divalent nickel is a high energy species, thus protonation of the active site would lower the electron density on the nickel facilitating reduction.

The difference in pH(D) dependence between the Ni_a-S to Ni_a-C transition in H_2O and D_2O suggests one of two possibilities; either proton transfer to the active site is slow relative to proton exchange of the donor residue (i.e. same donor in H_2O vs. D_2O) or that there is a different proton donor residue entirely which facilitates the EPT process that is shut down upon deprotonation at pH > 7.7. Based on the large pH dependence of the KIE, we propose that it is pH that modulates PT from two different donors with different mechanisms, favoring the latter explanation. There are two potential proton donor residues, His^{75} and Glu^{17} (*Pf* H_2ase numbering), both of which are largely conserved in [NiFe] H_2ases and within H^+ tunneling distances to the active site cysteine ligands. Using site directed mutagenesis and steady state kinetics, the glutamate residue has been shown to be critical in the enzymatic proton transport, but the histidine residue has been less explored. We favor the histidine residue as the proton source for the EPT mechanism due to the observed pH dependence, consistent with a characteristic histidine pK_a. In the PT-ET mechanism we favor the glutamic acid as the proton donor based on the dissimilarity in pH dependence relative to the EPT mechanism, site directed mutagenesis studies and theoretical predictions.

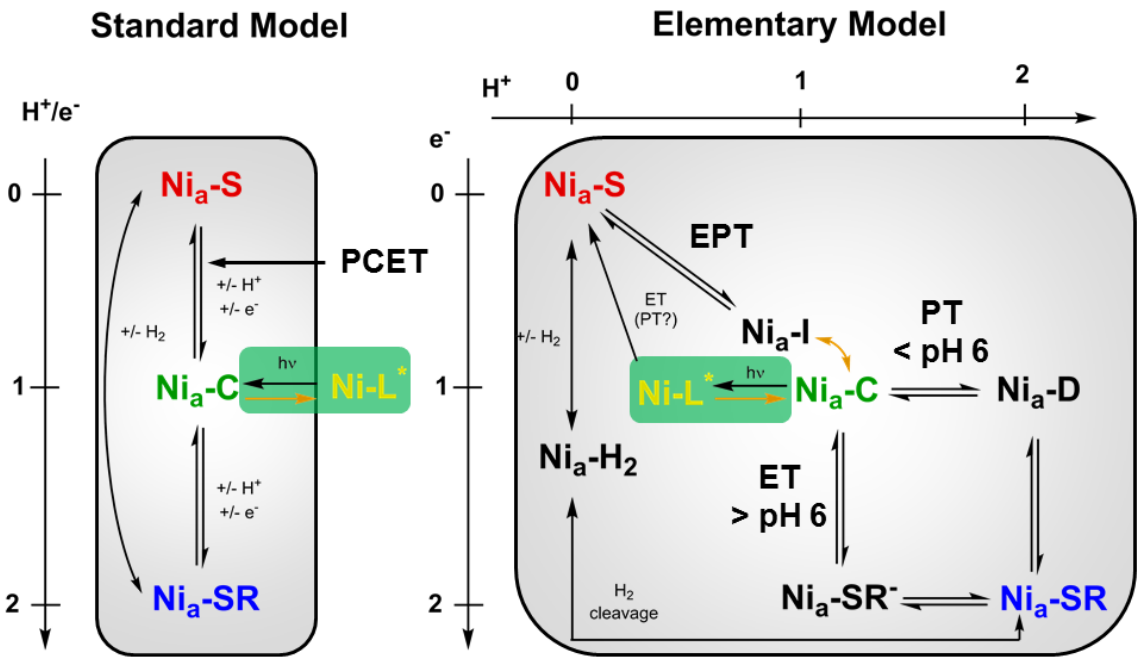

Figure 5.16 – Previously established "Standard" model and newly established elementary model for proton reduction by [NiFe] H_2ases. Previously observed intermediates are shown in color corresponding to colors used in the main text. New proposed intermediates, as well as the debated Ni_a-H_2 state are shown in black. Ni_a-I and Ni-L, as described in the text may be very similar or identical and are formally isoelectronic and isoprotic with the Ni_a-C state i.e. one electron reduced and mono-protonated. Purple arrows indicate hydride transfer in which no electrons or protons are exchanged to/from the active site. Ni-L is shown in green indicating a photo-chemically activated state.

[NiFe] hydrogenases typically function with high K_m for H_2 and an electrochemically defined bias towards H_2 oxidation, despite almost no over-potential for the reversible reduction of protons.[7,19,22,23] The observed EPT mechanism reported for *Pf* [NiFe] H_2ase could potentially explain this bias, where a fast second proton coupled

oxidation process pushes the equilibrium towards Ni_a-S in low H_2 conditions. Furthermore, it is interesting to note that the EPT mechanism only affects the Ni_a-S to Ni_a-C transition in the [NiFe] H_2ase, and has little kinetic effect in the proton reduction reaction since the formation of Ni_a-SR and subsequent product release are 100 fold slower. Others have shown multiple methods for kinetically tuning the bias of these enzymes through ET and H_2 diffusion, which together with the present results highlight an enzyme highly engineered in its function.

The EPT mechanism observed in this [NiFe] H_2ase may be different or absent in the less studied [FeFe] type of H_2ases, where again there is little thermodynamic over-potential, but a significant bias towards proton reduction and substantially faster TOF.[75,78,84,85,87] In a broader sense, the combined power of separately resolving the intermolecular ET and catalytic steps developed herein could open new doors for the study of other catalysts or redox active enzymes, not only H_2ases, which have been proposed to involve complex proton-coupled redox chemistry. The combinatory methodology presented herein of structure (infrared) and chemical potential (visible) specific kinetics after a photo-triggered perturbation could thus be a powerful technique for the study of complex redox processes in catalytic or enzymatic systems.

The second proton associated reduction event in the catalytic cycle, the Ni_a-C reduction to Ni_a-SR was also investigated at various pH's and solvent isotope compositions. Here the kinetics of active site chemistry are similar to the overall TOF, thus the steady state kinetics may reflect aspects of the elementary details of this process. The reduction of Ni_a-C was observed to be pH independent in pre-steady state kinetics (Fig. 5.15). Conversely the Ni_a-SR formation was pH dependent with nearly the same

slope as the pD dependence of the Ni_a-C formation. In contrast to the Ni_a-S reduction this process is instead consistent with a stepwise ET-PT mechanism, and an intermediate is inferred based on the delay of Ni_a-SR formation. The data were not described well by a coupled model further validating the step-wise mechanism. Reduction of Ni_a-C results in the formation of a transient state we term Ni_a-SR^-, a presumably EPR silent species. A small observed KIE in H_2O vs. D_2O of Ni_a-C decay (1.2) at pH(D) 7.0 is consistent with this interpretation as an ET modulated process. No KIE was observed for the Ni_a-SR formation. This is again somewhat intuitive since the trivalent nickel site would appear to favor direct reduction followed by protonation rather than protonating the electron deficient Ni_a-C state. The lack of a KIE on Ni_a-SR formation could be due to a reduction induced conformational step which brings the proton into the proper orientation for PT with PT faster than the conformational step. The recently reported sub-atomic resolution x-ray crystal structure of the nearly homogeneously prepared Ni_a-SR form of the [NiFe] H_2ase from *Desulfovibrio vulgaris* Miyazaki F shows that the Ni-S bond trans to the hydride becomes elongated, which may also be involved in stabilization of this species.[118] Further experiments on this process, including temperature dependence will help shed light on the explicit details and potentially detect the intermediate directly.

Based on the observed pH dependence of Ni_a-SR formation, at sufficiently low pH (< 6) a PT-ET mechanism would likely be favored over the presently observed ET-PT mechanism, resulting in a trivalent protonated state we term Ni_a-D. It is unclear whether this intermediate could be trapped because PT may be fast after reduction, which likely modulates the active site pK_a substantially. This would result in an inversion of the step-wise mechanism, but no intermediate formation due to a fast second step. These states,

the Ni_a-D and Ni_a-SR^- and the intermediate state Ni_a-I, complete the two dimensional (proton and electron) elementary mechanism of proton-coupled reduction of the *Pf* [NiFe] H_2ase illustrated in Figure 5.16. Here the most oxidized catalytically active state, Ni_a-S, is reduced and protonated simultaneously in a concerted EPT process likely involving substantial proton tunneling to form the Ni_a-I state. This intermediate state rapidly transforms by hydride formation to the known Ni_a-C state, a similar, if not identical process to that observed in the reformation of Ni_a-C from the photo-product Ni-L. The Ni_a-C is converted to the most reduced catalytically active state Ni_a-SR by a step-wise ET-PT mechanism which can be tuned by pH resulting in intermediates Ni_a-D and Ni_a-SR^- *en route* to formation of Ni_a-SR. An additional state involved in the complete mechanism of H^+ reduction has been proposed involving a metal bound H_2 molecule before product release (here termed Ni_a-H_2, Figure 5.16), completing a mechanism completely composed of elementary chemical steps. The nature of this state and its relevance as a true intermediate or a transition state in product formation has not been established representing another challenge in the determination of the complete mechanism of these enzymes.

5.2.6 – Proton Reduction by the [FeFe] H_2ase from *Thermotoga maritima*.

In an effort to compare and contrast the proton reduction dynamics of the well-known [NiFe] and [FeFe] H_2ases, the spectroscopic properties and pre-steady state kinetics of the novel [FeFe] H_2ase from *Thermotoga maritima* (Tm) were also investigated analogously to those for the *Pf* SHI.[95,96,119-121] The [FeFe] H_2ases have not been extensively characterized spectroscopically due to their irreversible inhibition by O_2

and their rather complicated steady state behavior. This is particularly true for the *Tm* [FeFe] H_2ase, which is highly sensitive to irreversible O_2 inhibition and has only been characterized by EPR spectroscopy.[95]

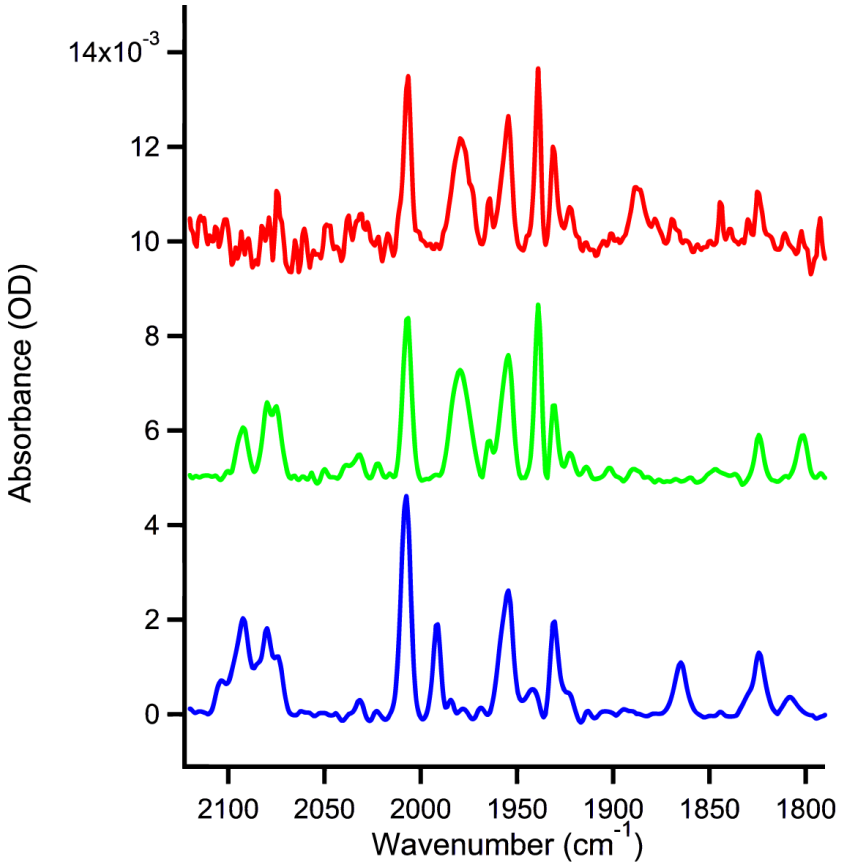

Figure 5.17 – FTIR spectrum of the CO and CN region of the [FeFe] *Tm* H_2ase. Red trace collected immediately after anaerobic sample preparation; green, after 4 day; and blue, after 15 days. [FeFe] concentration is estimated at 1 mM in a 75μm pathlength CaF_2 infrared cell with 10 mM MV, 12 mM NADH and 50 mM phosphate buffer pH 7.0.

The FTIR spectrum of the *Tm* [FeFe] H_2ase was thus analyzed to determine further understand the steady state properties of this enzyme (Fig. 5.17). The FTIR

spectrum of the *Tm* [FeFe] H_2ase in an N_2 atmosphere with 12 mM NADH and 10 mM MV^{2+} exhibited 2 peaks in the CN region (2060-2110 cm^{-1}), 8-9 peaks in the terminal CO region (1880-2030 cm^{-1}) and one peak in the bridging CO region of the spectrum (1790-1870 cm^{-1}). It is known that the terminal CO bands are the most intense vibrational transitions associated with the active site, consistent with those observed in the *Tm* H_2ase. The enzyme exhibited strong terminal CO resonances at 1930, 1939, 1955, 1978, 1983 and 2006 cm^{-1} and minor components at 1923, 1964 and 1888 cm^{-1}. Based on the model of two terminal CO species per stable redox state, the spectrum represents at least three significantly populated states and one or more less populated states. Sequence similarity to other known [FeFe] H_2ases, and the slow oxidation behavior of these states their assignment has been summarized in Table 5.4 below.[74,75,78,81,84,85,87]

State	ν CN_T(1)	ν CN_T(2)	ν CO_T(1)	ν CO_T(2)	ν CO_B
$H_{inact}1$	2091	2080	2006	1983	1824
$H_{inact}2$	2105	2091	2007	1991	1864
H_{trans}	N/O	N/O	1983	1979	1804
H_{ox}	2090	2081	1964	1940	1824
H_{red}	N/O	N/O	N/O	N/O	N/O
H_{sred}	N/O	N/O	1954	1930	1888

Table 5.4 – FTIR vibrational signature (in cm^{-1}) summary of the [FeFe] H_2ase from *Thermotoga maritima*. N/O indicates not observed and N/A indicates not assigned. Red species indicate a highly distorted bridging CO that is more properly described as a terminal CO trans to the H^+/H_2 binding site.

The observed FTIR results indicate a significantly different active site geometry from the previously investigated *Chlamydomonas reinhardtii* or *Desulfovibrio desurfuricans* [FeFe] H_2ases.[74-76,81,85,87] This is not surprising since there are only two [FeFe] H_2ases which have been extensively examined by infrared spectroscopy. A complete understanding of the steady states derived from the FTIR spectrum is currently being investigated, and will likely implicate different reactivity of these H_2ases relative to other investigated [FeFe] H_2ases.

Using analogous techniques to those employed for the SHI of *Pf*, the transient inter-conversion of active site steady states was investigated using tandem transient visible and infrared absorbance spectroscopy. Based on the transient analysis of the MV^+ (Fig 5.18) absorbance the MV^+ decay was again modeled well with two exponential phases with rates of 2.18 +/- 0.07 * 10^3 and 166 +/- 2 s^{-1} indicating relatively fast interfacial ET that is faster than the overall turnover frequency of 10 s^{-1} previously reported.[120] Based on the initial induced absorbance, a net MV^+ concentration jump is calculated at 200 μM, of which 100 μM was consumed within the experimental time resolution. Unfortunately, due to improper sample and reference optical density matching a determination of the solvated electron consumption/generation could not be determined, but it is expected based on previous results with the [NiFe] SHI of *Pf* that there indeed would be some direct reduction, thus the estimates of 100 μM enzyme reduction are likely underestimates.

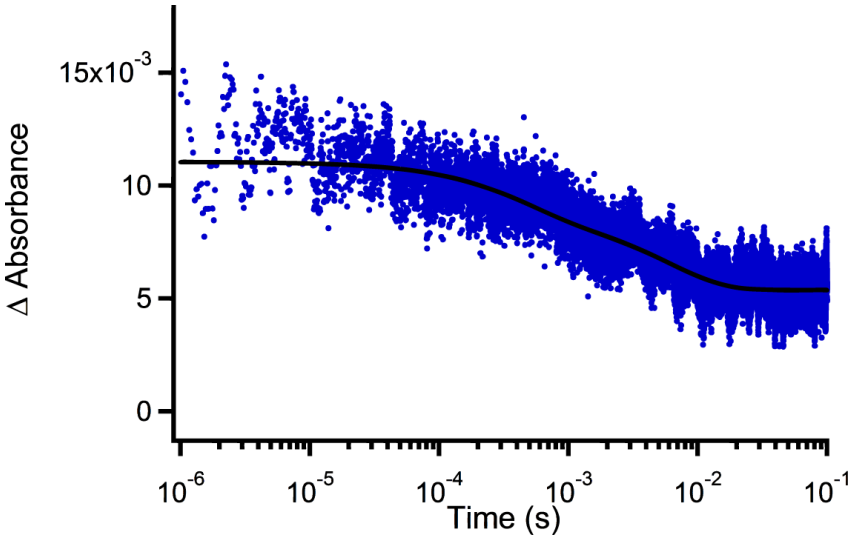

Figure 5.18 – Transient visible dynamics of MV^+. The transient was fit to a double exponential decay with timeconstants of 2.18 +/- 0.07 * 10^3 and 166 +/- 2 s^{-1}.

Transient infrared analysis did not yield substantial signals due to the low initial absorbance of all steady states due to low concentration as well as the lower MV yield. Despite this, dynamics were observed for multiple wavelengths probed including 1954, 1939 and 1888 cm^{-1} associated with the H_{sred} and H_{ox} states respectively and are reported in Figure 5.19. The H_{ox} state was observed to bleach with a rate constant of 54 +/- 1 and 190 +/- 4 s^{-1}. Both rates were slower than the interfacial ET rate indicating intermolecular ET is not rate determining. The origin of the biphasic behavior here is not clear. The fast rate is very similar to the slower phase of intermolecular ET observed by transient visible absorbance of the MV^+ radical (Fig. 5.18), indicating intramolecular ET to the most proximal redox cofactor is probably not rate determining. This is not surprising in light of the results with the *Pf* SHI and in the relatively short ET chain to the active site. A more plausible mechanism is a rate determined by either ET or PT to the active site from the proximal FeS cluster. This reduction event should result in the formation of the H_{red} state

based on the standard model proposed in the literature. No induced absorbance dynamics were observed at wavelengths consistent with the H_{red} state, although this state has little consistent description spectroscopically in the two organisms [FeFe] H_2ases currently characterized. Further characterization of this process will require pH control, power dependence and KIEs.

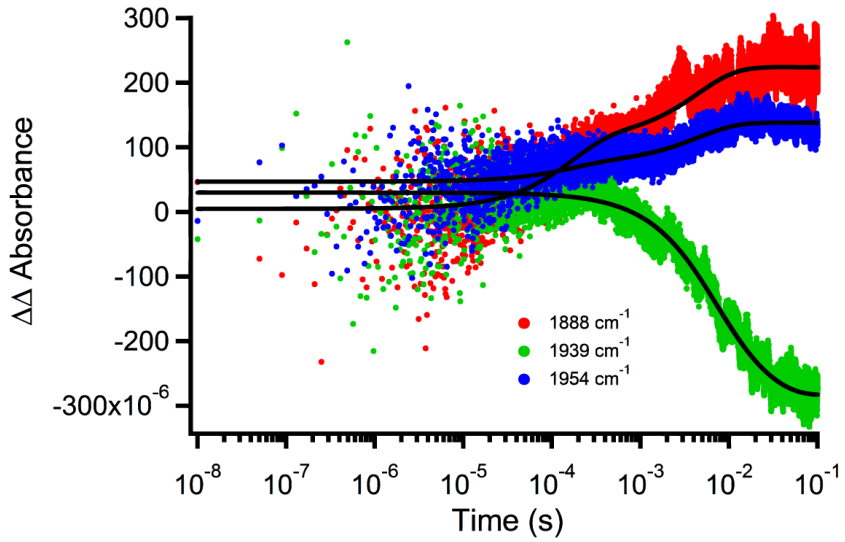

Figure 5.19 – *Tm* [FeFe] H_2ase terminal CO transient infrared traces after photoionization of NADH. Red, terminal trans CO of H_{sred} probed at 1888 cm^{-1}, blue terminal cis CO of H_{sred} probed at 1954 cm-1, green, terminal cis CO of H_{ox} probed at 1939 cm^{-1}. Fits shown in black.

Interestingly, as noted above, a terminal CO in the frequency range of the H_{sred} was observed which decayed very rapidly with respect to the overall timescale of the measurements (1888 cm^{-1} band in red trace of Fig. 5.17). In [FeFe] H_2ases which display the H_{sred} signals at very low potentials do not contain ancillary FeS clusters, which

rapidly quench the highly reduced active site by back ET. Here this H_{sred} state appears to be stable even in the presence of ancillary redox active cofactors. This could be due to numerous aspects of the enzyme that at this point cannot be addressed due to a lack of structural and functional studies of this enzyme. This state was investigated in transient photo-reduction experiments which revealed clear induced absorbance signals consistent with the formation of this highly reduced state. Infrared transients were collected at wavelengths associated with the terminal and formerly bridging CO *trans* to the H^+/H^- binding site. Both transients' revealed identical dynamics, biphasic induced absorbance signals with timescales that were largely separated in time at 6.3 +/- 0.1 * 10^3 and 224 +/- 2 s^{-1}. The fast phase is approximately three times faster than the fastest intermolecular ET rate. An explanation for this could be either a photo-chemically induced transition, or a fast reduction from unresolved ET by solvated electrons. The former is highly unlikely due to the extremely short lifetimes of FeS clusters and minimal photo-chemistry observed in these enzymes relative to the [NiFe] H_2ase counterparts. The latter mechanism indicates an intramolecular ET timescale that is delayed over four decades in time later indicating a slow intramolecular ET relative to the [NiFe] counterparts. This could be to a more oxidizing potential of the [NiFe] active site, or differences in redox levels and distances or overlap of FeS cluster cofactors. The method described herein may also allow experimentalists to examine the involvement of the H_{sred} state in [FeFe] H_2ases which do not support the H_{sred} state as a steady state, thus its ubiquity in the mechanism of [FeFe] H_2ases could be investigated.[84,87]

5.3 – Conclusions

The analysis of pre-steady state kinetics of the [NiFe] and [FeFe] H_2ases have been examined under numerous conditions, spectral and temporal domains by probing intermolecular ET through transient visible spectroscopy and active site chemistry by transient infrared spectroscopy. Transient visible spectroscopy sensitive to the MV^+ radical cation indicate at least two interfacial ET mechanisms, an early reduction mechanism by solvated electrons generated by the NADH photolysis process on a very rapid timescale (100 ns) and a second process at later time (10^2-10^3 s^{-1}) facilitated by oxidation of MV^+. MV^+ interaction with the H_2ases is of great interest due to the universality of it as a redox mediator to these enzymes, but the remarkably different behavior of catalytic activity in solution assays with MV and on electrodes by protein film voltammetry. These experiments represent the first direct experimental method to address this difference. The fast interfacial ET allowed for the observation of active site chemistry at unprecedented time resolutions by transient infrared.

Transient infrared analysis of photo-reduction dynamics revealed rapid active site chemistry relative to the overall turnover frequency of the enzyme, and for the first time, kinetically validated three proposed catalytic intermediates in the [NiFe] (Ni_a-S, Ni_a-C and Ni_a-SR) and two intermediates in the [FeFe] catalytic mechanism (H_{ox} and H_{sred}), as well as implicating three new intermediates in the [NiFe] H_2ase mechanism (Ni_a-I, Ni_a-D and Ni_a-SR^-). By tuning system conditions including pH and solvent isotope conditions, elementary details of the proton reduction mechanism for the [NiFe] H_2ase could be determined. These studies definitively demonstrated a multi-site EPT mechanism in the Ni_a-S reduction to Ni_a-C which involved substantial proton tunneling. This is the first

direct observation of such a phenomenon in a biological system, and the methodology used to investigate this phenomenon may be broadly applicable to investigations in other systems proposed to involve EPT such as photosystem II, cytochrome c oxidase and ribonucleotide reductase. Interestingly, the [NiFe] H_2ases also have a step-wise proton coupled reduction mechanism that facilitates the reduction of the Ni_a-C state. The reason for this heterogeneity is still not understood, but the results presented herein may implicate a kinetic biasing mechanism that among other protein factors explains the observed bias of these enzymes toward H_2 oxidation.

In comparison of the pre-steady state and steady state kinetic results from others and those presented in Chapter 3 of this thesis, a conclusive mechanism of proton reduction in the SHI of Pf could be deduced in which rapid EPT from the Ni_a-S state generates a highly reactive intermediate denoted Ni_a-I, which is nearly identical to the Ni-L state, which subsequently forms the Ni_a-C state orders of magnitude faster than the overall reaction rate. Subsequent ET-PT proceeding through the newly discovered Ni_a-SR^- state occurs on a timescale very similar to the overall turnover frequency consistent with the small pH dependence on overall H_2 production and H/D exchange rates. After formation of the Ni_a-SR state, the eventual product release is rate determining as indicated by steady state KIE and minimal pH dependence.

Preliminary results on the [FeFe] H_2ase indicate that this enzyme also performs inter- and intramolecular ET faster than the overall TOF indicating new intermediates that may be discovered using this technique. By coupling these studies to steady state kinetic analysis, the elementary mechanism of these enzymes may also be determined. Comparison of these two mechanisms in conjunction with structural studies will shed

light on the convergent evolutionary aspects of biological proton reduction and H_2 oxidation which will certainly aid in synthetic catalyst development and an improved understanding of PCET in biological systems.

5.4 - References

(1) Jones, A. K.; Sillery, E.; Albracht, S. P. J.; Armstrong, F. A. *Chem Comm* **2002**, 866.

(2) Armstrong, F. A.; Albracht, P. J. *Philos T Roy Soc A* **2005**, *363*, 937.

(3) Fontecilla-Camps, J. C.; Volbeda, A.; Cavazza, C.; Nicolet, Y. *Chem Rev* **2007**, *107*, 4273.

(4) Lubitz, W. *J Biol Inorg Chem* **2014**, *19*, S99.

(5) Lubitz, W.; Ogata, H.; Rudiger, O.; Reijerse, E. *Chem Rev* **2014**, *114*, 4081.

(6) Lubitz, W.; Reijerse, E.; van Gastel, M. *Chem Rev* **2007**, *107*, 4331.

(7) Vincent, K. A.; Parkin, A.; Armstrong, F. A. *Chem Rev* **2007**, *107*, 4366.

(8) Fisher, H. F.; Krasna, A. I.; Rittenberg, D. *J Biol Chem* **1954**, *209*, 569.

(9) Krasna, A. I.; Rittenberg, D. *Proc Natl Acad Sci U S A* **1956**, *42*, 180.

(10) Purec, L.; Krasna, A. I.; Rittenberg, D. *Biochemistry-Us* **1962**, *1*, 270.

(11) Tamiya, N.; Miller, S. L. *J Biol Chem* **1963**, *238*, 2194.

(12) Yagi, T.; Tsuda, M.; Inokuchi, H. *J Biochem-Tokyo* **1973**, *73*, 1069.

(13) Arp, D. J.; Burris, R. H. *Biochim Biophys Acta* **1982**, *700*, 7.

(14) McTavish, H.; SayavedraSoto, L. A.; Arp, D. J. *BBA-Protein Struct M* **1996**, *1294*, 183.

(15) Zorin, N. A.; Dimon, B.; Gagnon, J.; Gaillard, J.; Carrier, P.; Vignais, P. M. *Eur J Biochem* **1996**, *241*, 675.

(16) Massanz, C.; Fliedrich, B. *Biochemistry-Us* **1999**, *38*, 14330.

(17) Bertrand, P.; Dole, F.; Asso, M.; Guigliarelli, B. *J Biol Inorg Chem* **2000**, *5*, 682.

(18) Vignais, P. M.; Cournac, L.; Hatchikian, E. C.; Elsen, S.; Serebryakova, L.; Zorin, N.; Dimon, B. *Int J Hydrogen Energ* **2002**, *27*, 1441.

(19) van Haaster, D. J.; Hagedoorn, P. L.; Jongejan, J. A.; Hagen, W. R. *Biochem Soc T* **2005**, *33*, 12.

(20) Vignais, P. M. *Coordin Chem Rev* **2005**, *249*, 1677.

(21) Dementin, S.; Burlat, B.; Fourmond, V.; Leroux, F.; Liebgott, P. P.; Abou Hamdan, A.; Leger, C.; Rousset, M.; Guigliarelli, B.; Bertrand, P. *J Am Chem Soc* **2011**, *133*, 10211.

(22) Abou Hamdan, A.; Dementin, S.; Liebgott, P. P.; Gutierrez-Sanz, O.; Richaud, P.; De Lacey, A. L.; Roussett, M.; Bertrand, P.; Cournac, L.; Leger, C. *J Am Chem Soc* **2012**, *134*, 8368.

(23) Fourmond, V.; Baffert, C.; Sybirna, K.; Dementin, S.; Abou-Hamdan, A.; Meynial-Salles, I.; Soucaille, P.; Bottin, H.; Leger, C. *Chem Comm* **2013**, *49*, 6840.

(24) DeLacey, A. L.; Fernandez, V. M.; Rousset, M.; Cavazza, C.; Hatchikian, E. C. *J Biol Inorg Chem* **2003**, *8*, 129.

(25) Dementin, S.; Burlat, B.; De Lacey, A. L.; Pardo, A.; Adryanczyk-Perrier, G.; Guigliarelli, B.; Fernandez, V. M.; Rousset, M. *J Biol Chem* **2004**, *279*, 10508.

(26) Dementin, S.; Belle, V.; Champ, S.; Bertrand, P.; Guigliarelli, B.; De Lacey, A. L.; Fernandez, V. M.; Leger, C.; Rousset, M. *Int J Hydrogen Energ* **2008**, *33*, 1503.

(27) Armstrong, F. A.; Belsey, N. A.; Cracknell, J. A.; Goldet, G.; Parkin, A.; Reisner, E.; Vincent, K. A.; Wait, A. F. *Chem Soc Rev* **2009**, *38*, 36.

(28) Hexter, S. V.; Grey, F.; Happe, T.; Climent, V.; Armstrong, F. A. *P Natl Acad Sci USA* **2012**, *109*, 18232.

(29) Krasna, A. I.; Rittenberg, D. *J Am Chem Soc* **1954**, *76*, 3015.

(30) Peck, H. D.; Pietro, A. S.; Gest, H. *P Natl Acad Sci USA* **1956**, *42*, 13.

(31) Peck, H. D.; Gest, H. *J Bacteriol* **1956**, *71*, 70.

(32) Krasna, A. I.; Riklis, E.; Rittenberg, D. *J Biol Chem* **1960**, *235*, 2717.

(33) Riklis, E.; Rittenberg, D. *J Biol Chem* **1961**, *236*, 2526.

(34) Sadana, J. C.; Rittenberg, D. *P Natl Acad Sci USA* **1963**, *50*, 900.

(35) Gogotov, I. N.; Zorin, N. A.; Serebriakova, L. T.; Kondratieva, E. N. *Biochim Biophys Acta* **1978**, *523*, 335.

(36) Bryant, F. O.; Adams, M. W. W. *J Biol Chem* **1989**, *264*, 5070.

(37) Rakhely, G.; Zhou, Z. H.; Adams, M. W. W.; Kovacs, K. L. *Eur J Biochem* **1999**, *266*, 1158.

(38) Sapra, R.; Verhagen, M. F. J. M.; Adams, M. W. W. *J Bacteriol* **2000**, *182*, 3423.

(39) Pershad, H. R.; Duff, J. L. C.; Heering, H. A.; Duin, E. C.; Albracht, S. P. J.; Armstrong, F. A. *Biochemistry-Us* **1999**, *38*, 8992.

(40) Pershad, H. R.; Duff, J. L. C.; Heering, H. A.; Duin, E. C.; Albracht, S. P. J.; Armstrong, F. A. *J Inorg Biochem* **1999**, *74*, 264.

(41) Parkin, A.; Goldet, G.; Cavazza, C.; Fontecilla-Camps, J. C.; Armstrong, F. A. *J Am Chem Soc* **2008**, *130*, 13410.

(42) McIntosh, C. L.; Germer, F.; Schulz, R.; Appel, J.; Jones, A. K. *J Am Chem Soc* **2011**, *133*, 11308.

(43) Madden, C.; Vaughn, M. D.; Diez-Perez, I.; Brown, K. A.; King, P. W.; Gust, D.; Moore, A. L.; Moore, T. A. *J Am Chem Soc* **2012**, *134*, 1577.

(44) Vignais, P. M.; Colbeau, A. *Curr Issues Mol Biol* **2004**, *6*, 159.

(45) Vignais, P. M.; Billoud, B. *Chem Rev* **2007**, *107*, 4206.

(46) Mctavish, H.; Sayavedrasoto, L. A.; Arp, D. J. *J Bacteriol* **1995**, *177*, 3960.

(47) Coremans, J. M.; van Garderen, C. J.; Albracht, S. P. *Biochim Biophys Acta* **1992**, *1119*, 148.

(48) Fernandez, V. M.; Hatchikian, E. C.; Cammack, R. *Biochim Biophys Acta* **1985**, *832*, 69.

(49) Burgdorf, T.; De Lacey, A. L.; Friedrich, B. *J Bacteriol* **2002**, *184*, 6280.

(50) de Lacey, A. L.; Fernandez, V. M.; Rousset, M. *Coord Chem Rev* **2005**, *249*, 1596.

(51) Dementin, S.; Belle, V.; Bertrand, P.; Guigliarelli, B.; Adryanczyk-Perrier, G.; De Lacey, A. L.; Fernandez, V. M.; Rousset, M.; Leger, C. *J Am Chem Soc* **2006**, *128*, 5209.

(52) Rousset, M.; Montet, Y.; Guigliarelli, B.; Forget, N.; Asso, M.; Bertrand, P.; Fontecilla-Camps, J. C.; Hatchikian, E. C. *P Natl Acad Sci USA* **1998**, *95*, 11625.

(53) Dementin, S.; Leroux, F.; Cournac, L.; de Lacey, A. L.; Volbeda, A.; Leger, C.; Burlat, B.; Martinez, N.; Champ, S.; Martin, L.; Sanganas, O.; Haumann, M.; Fernandez, V. M.; Guigliarelli, B.; Fontecilla-Camps, J. C.; Rousset, M. *J Am Chem Soc* **2009**, *131*, 10156.

(54) Pandelia, M. E.; Ogata, H.; Lubitz, W. *Chemphyschem* **2010**, *11*, 1127.

(55) De Lacey, A. L.; Fernandez, V. M.; Rousset, M.; Cammack, R. *Chem Rev* **2007**, *107*, 4304.

(56) Fichtner, C.; Laurich, C.; Bothe, E.; Lubitz, W. *Biochemistry-Us* **2006**, *45*, 9706.

(57) Pandelia, M. E.; Ogata, H.; Currell, L. J.; Flores, M.; Lubitz, W. *J Biol Inorg Chem* **2009**, *14*, 1227.

(58) Montet, Y.; Amara, P.; Volbeda, A.; Vernede, X.; Hatchikian, E. C.; Field, M. J.; Frey, M.; FontecillaCamps, J. C. *Nat Struct Biol* **1997**, *4*, 523.

(59) Ogata, H.; Mizoguchi, Y.; Mizuno, N.; Miki, K.; Adachi, S.; Yasuoka, N.; Yagi, T.; Yamauchi, O.; Hirota, S.; Higuchi, Y. *J Am Chem Soc* **2002**, *124*, 11628.

(60) DeLacey, A. L.; Stadler, C.; Fernandez, V. M.; Hatchikian, E. C.; Fan, H. J.; Li, S. H.; Hall, M. B. *J Biol Inorg Chem* **2002**, *7*, 318.

(61) Vanderzwaan, J. W.; Albracht, S. P. J.; Fontijn, R. D.; Slater, E. C. *FEBS Lett* **1985**, *179*, 271.

(62) Fan, C. L.; Teixeira, M.; Moura, J.; Moura, I.; Huynh, B. H.; Legall, J.; Peck, H. D.; Hoffman, B. M. *J Am Chem Soc* **1991**, *113*, 20.

(63) Brecht, M.; van Gastel, M.; Buhrke, T.; Friedrich, B.; Lubitz, W. *J Am Chem Soc* **2003**, *125*, 13075.

(64) Lubitz, W.; Brecht, M.; Foerster, S.; van Gastel, M.; Stein, M. *ACS Sym Ser* **2003**, *858*, 128.

(65) Foerster, S.; van Gastel, M.; Brecht, M.; Lubitz, W. *J Biol Inorg Chem* **2005**, *10*, 51.

(66) Adams, M. W. W. *Biochim Biophys Acta* **1990**, *1020*, 115.

(67) Peters, J. W. *Curr Opin Struc Biol* **1999**, *9*, 670.

(68) Fontecilla-Camps, J. C.; Volbeda, A.; Cavazza, C.; Nicolet, Y. *Chem Rev* **2007**, *107*, 4273.

(69) Mulder, D. W.; Shepard, E. M.; Meuser, J. E.; Joshi, N.; King, P. W.; Posewitz, M. C.; Broderick, J. B.; Peters, J. W. *Structure* **2011**, *19*, 1038.

(70) Lubitz, W.; Ogata, H.; Rudiger, O.; Reijerse, E. *Chem Rev* **2014**, *114*, 4081.

(71) Huynh, B. H.; Czechowski, M. H.; Kruger, H. J.; Dervartanian, D. V.; Peck, H. D.; Legall, J. *P Natl Acad Sci-Biol* **1984**, *81*, 3728.

(72) Wang, G.; Benecky, M. J.; Huynh, B. H.; Cline, J. F.; Adams, M. W. W.; Mortenson, L. E.; Hoffman, B. M.; Munck, E. *J Biol Chem* **1984**, *259*, 4328.

(73) Fu, W.; Drozdzewski, P. M.; Morgan, T. V.; Mortenson, L. E.; Juszczak, A.; Adams, M. W.; He, S. H.; Peck, H. D., Jr.; DerVartanian, D. V.; LeGall, J.; et al. *Biochemistry-Us* **1993**, *32*, 4813.

(74) Pierik, A. J.; Hulstein, M.; Hagen, W. R.; Albracht, S. P. J. *Eur J Biochem* **1998**, *258*, 572.

(75) De Lacey, A. L.; Stadler, C.; Cavazza, C.; Hatchikian, E. C.; Fernandez, V. M. *J Am Chem Soc* **2000**, *122*, 11232.

(76) Nicolet, Y.; de Lacey, A. L.; Vernede, X.; Fernandez, V. M.; Hatchikian, E. C.; Fontecilla-Camps, J. C. *J Am Chem Soc* **2001**, *123*, 1596.

(77) Chen, Z. J.; Lemon, B. J.; Huang, S.; Swartz, D. J.; Peters, J. W.; Bagley, K. A. *Biochemistry-Us* **2002**, *41*, 2036.

(78) Albracht, S. P. J.; Roseboom, W.; Hatchikian, E. C. *J Biol Inorg Chem* **2006**, *11*, 88.

(79) Roseboom, W.; De Lacey, A. L.; Fernandez, V. M.; Hatchikian, E. C.; Albracht, S. P. J. *J Biol Inorg Chem* **2006**, *11*, 102.

(80) Silakov, A.; Reijerse, E. J.; Albracht, S. P. J.; Hatchikian, E. C.; Lubitz, W. *J Am Chem Soc* **2007**, *129*, 11447.

(81) Silakov, A.; Kamp, C.; Reijerse, E.; Happe, T.; Lubitz, W. *Biochemistry-Us* **2009**, *48*, 7780.

(82) Silakov, A.; Wenk, B.; Reijerse, E.; Lubitz, W. *Phys Chem Chem Phys* **2009**, *11*, 6592.

(83) Stripp, S.; Sanganas, O.; Happe, T.; Haumann, M. *Biochemistry-Us* **2009**, *48*, 5042.

(84) Adamska, A.; Silakov, A.; Lambertz, C.; Rudiger, O.; Happe, T.; Reijerse, E.; Lubitz, W. *Angew Chem Int Ed* **2012**, *51*, 11458.

(85) Mulder, D. W.; Ratzloff, M. W.; Shepard, E. M.; Byer, A. S.; Noone, S. M.; Peters, J. W.; Broderick, J. B.; King, P. W. *J Am Chem Soc* **2013**, *135*, 6921.

(86) Adamska-Venkatesh, A.; Krawietz, D.; Siebel, J.; Weber, K.; Happe, T.; Reijerse, E.; Lubitz, W. *J Am Chem Soc* **2014**, *136*, 11339.

(87) Mulder, D. W.; Ratzloff, M. W.; Bruschi, M.; Greco, C.; Koonce, E.; Peters, J. W.; King, P. W. *J Am Chem Soc* **2014**, *136*, 15394.

(88) Parkin, A.; Cavazza, C.; Fontecilla-Camps, J. C.; Armstrong, F. A. *J Am Chem Soc* **2006**, *128*, 16808.

(89) Hexter, S. V.; Grey, F.; Happe, T.; Climent, V.; Armstrong, F. A. *P Natl Acad Sci USA* **2012**, *109*, 11516.

(90) Fernandez, V. M.; Gutierrez, C.; Ballesteros, A. *Anal Biochem* **1982**, *120*, 85.

(91) Cornish, A. J.; Gartner, K.; Yang, H.; Peters, J. W.; Hegg, E. L. *J Biol Chem* **2011**, *286*, 38341.

(92) Lemon, B. J.; Peters, J. W. *Biochemistry-Us* **1999**, *38*, 12969.

(93) Happe, R. P.; Roseboom, W.; Albracht, S. P. J. *Eur J Biochem* **1999**, *259*, 602.

(94) George, S. J.; Kurkin, S.; Thorneley, R. N. F.; Albracht, S. P. J. *Biochemistry-Us* **2004**, *43*, 6808.

(95) Schut, G. J.; Adams, M. W. W. *J Bacteriol* **2009**, *191*, 4451.

(96) Wang, S. N.; Huang, H. Y.; Kahnt, J.; Mueller, A. P.; Kopke, M.; Thauer, R. K. *J Bacteriol* **2013**, *195*, 4373.

(97) deLacey, A. L.; Hatchikian, E. C.; Volbeda, A.; Frey, M.; FontecillaCamps, J. C.; Fernandez, V. M. *J Am Chem Soc* **1997**, *119*, 7181.

(98) Wang, H. X.; Ralston, C. Y.; Patil, D. S.; Jones, R. M.; Gu, W.; Verhagen, M.; Adams, M.; Ge, P.; Riordan, C.; Marganian, C. A.; Mascharak, P.; Kovacs, J.; Miller, C. G.; Collins, T. J.; Brooker, S.; Croucher, P. D.; Wang, K.; Stiefel, E. I.; Cramer, S. P. *J Am Chem Soc* **2000**, *122*, 10544.

(99) Orii, Y. *Biochemistry-Us* **1993**, *32*, 11910.

(100) Czochralska, B.; Lindqvist, L. *Chem Phys Lett* **1983**, *101*, 297.

(101) Lindqvist, L.; Czochralska, B.; Grigorov, I. *Chem Phys Lett* **1985**, *119*, 494.

(102) Jortner, J.; Ottolenghi, M.; Rabani, J.; Stein, G. *J Chem Phys* **1962**, *37*, 2488.

(103) Boag, J. W.; Hart, E. J. *Nature* **1963**, *197*, 45.

(104) Gordon, S.; Thomas, J. K.; Matheson, M. S.; Rabani, J.; Hart, E. J. *J Am Chem Soc* **1963**, *85*, 1375.

(105) Austin, R. H.; Beeson, K.; Eisenstein, L.; Frauenfelder, H.; Gunsalus, I. C.; Marshall, V. P. *Science* **1973**, *181*, 541.

(106) Austin, R. H.; Beeson, K. W.; Eisenstein, L.; Frauenfelder, H.; Gunsalus, I. C. *Biochemistry-Us* **1975**, *14*, 5355.

(107) Alberding, N.; Austin, R. H.; Beeson, K. W.; Chan, S. S.; Eisenstein, L.; Frauenfelder, H.; Nordlund, T. M. *Science* **1976**, *192*, 1002.

(108) Arendsen, A. F.; Veenhuizen, P. T. M.; Hagen, W. R. *FEBS Lett* **1995**, *368*, 117.

(109) Silva, P. J.; de Castro, B.; Hagen, W. R. *J Biol Inorg Chem* **1999**, *4*, 284.

(110) Tai, H.; Nishikawa, K.; Suzuki, M.; Higuchi, Y.; Hirota, S. *Angew Chem Int Ed* **2014**, *53*, 13817.

(111) Kellers, P.; Pandelia, M. E.; Currell, L. J.; Gorner, H.; Lubitz, W. *Phys Chem Chem Phys* **2009**, *11*, 8680.

(112) Wisitruangsakul, N.; Lenz, O.; Ludwig, M.; Friedrich, B.; Lendzian, F.; Hildebrandt, P.; Zebger, I. *Angew Chem Int Edit* **2009**, *48*, 611.

(113) Pandelia, M. E.; Fourmond, V.; Tron-Infossi, P.; Lojou, E.; Bertrand, P.; Leger, C.; Giudici-Orticoni, M. T.; Lubitz, W. *J Am Chem Soc* **2010**, *132*, 6991.

(114) Pandelia, M. E.; Infossi, P.; Stein, M.; Giudici-Orticoni, M. T.; Lubitz, W. *Chem Comm* **2012**, *48*, 823.

(115) Knapp, M. J.; Klinman, J. P. *Eur J Biochem* **2002**, *269*, 3113.

(116) Hammes-Schiffer, S.; Stuchebrukhov, A. A. *Chem Rev* **2010**, *110*, 6939.

(117) Weinberg, D. R.; Gagliardi, C. J.; Hull, J. F.; Murphy, C. F.; Kent, C. A.; Westlake, B. C.; Paul, A.; Ess, D. H.; McCafferty, D. G.; Meyer, T. J. *Chem Rev* **2012**, *112*, 4016.

(118) Ogata, H.; Nishikawa, K.; Lubitz, W. *Nature* **2015**, *advance online publication*.

(119) Juszczak, A.; Aono, S.; Adams, M. W. W. *J Biol Chem* **1991**, *266*, 13834.

(120) Verhagen, M. F. J. M.; O'Rourke, T.; Adams, M. W. W. *BBA-Bioenergetics* **1999**, *1412*, 212.

(121) Schuchmann, K.; Muller, V. *J Biol Chem* **2012**, *287*, 31165.